TUM School of Engineering and Design

Implementation of the SP_3 approximation for the neutron transport equation in FENNECS

Silvia lo Muzio

Vollständiger Abdruck der von der TUM School of Engineering and Design der Technischen Universität München zur Erlangung einer **Doktorin der Ingenieurwissenschaften (Dr.-Ing.)** genehmigten Dissertation.

Vorsitz:		Prof. Carlo Luigi Bottasso
Prüfende der Dissertation:	1.	Prof. Dr. Rafael Macián-Juan
	2.	Prof. Gumersindo Jesús Verdú Martín
	3.	Prof. Piero Ravetto

Die Dissertation wurde am 14.02.2024 bei der Technische Universität München eingereicht und durch die TUM School of Engineering and Design am 20.06.2024 angenommen.

Acknowledgments

Although a doctorate is a very personal endeavour, you are never alone on this journey. In my case, many persons supported me in various ways and aided completing this project. I will always be grateful for the support I received. Being aware that I can not name all the persons who helped my during this time, I want to thank those who I am particularly grateful to here in the following.

Firstly, I would like to thank my doctor father Prof. Macián-Juan for having supported and supervised me during the last years. He was always open for questions during my whole doctorate. Furthermore, I would like to thank him for his guidance during my whole study period in the field of nuclear engineering.

For the solid and ensured financial support of my work during the last three years, I would like to thank Gesellschaft für Anlagen- und Reaktorsicherheit (GRS) gGmbH, which allowed me to conduct this doctorate project.

I would like to express my gratitude to all my colleagues, present as well as former ones, of the Nuclear Fuel Department, A303, at GRS. I strongly appreciated their daily and continuous support in every situation, also in the most difficult times. Furthermore, they were always available for questions and open to help me at any time. I am very lucky to have such nice colleagues during my work at GRS.

In particular, I thank Dr. Robert Kilger, head of the Nuclear Fuel Department, who believed in me and gave me the possibility to conduct my doctorate in his department.

A special thank goes to the project leader of this work as well as mentor of this dissertation, Dr. Armin Seubert, who guided me through this work.

Especially, I would like to express my deepest gratitude to Dr. Jeremy Bousquet for his technical as well moral support. His teachings were fundamental for this work. He was always available to help me with any kind of issue.

A big role was also played by Dr. Romain Henry, whose help was crucial, particularly in my first months at GRS.

I would also like to thank my Italian colleagues at GRS, Simone Palazzo, Dr. Vincenzo Anthony Di Nora, and Dr. Thomas Eisenstecken, who were always available for an espresso or a tea break.

Furthermore, for the support during this journey, I would like to acknowledge my closest friends. Their support and encouragements were very important for me.

A very special thank goes to my partner, Joachim Leibold, who was the first one who encouraged me to start my studies in nuclear engineering. He believed in me and he constantly and continuously supported me. This strongly contributed to this work. His love was essential in the last years. No words can be found to express how grateful I am to him.

I am extremely grateful to my mother, whose very strong support was fundamental. She is my greatest supporter and the best mother I could ever ask for. Additionally, she has been a solid pillar on which I could count in every moment of my life. Her encouragements helped me a lot and her presence in the most difficult moments was essential.

Last but not least, special thanks go to Dr. Flavio Carsughi, whose advices and help were fundamental. He was the first one, who allowed me to work in this field. Without this opportunity, very probably, I would never have started this doctorate.

Publications

Full paper peer reviewed publications

[38] Silvia lo Muzio and Armin Seubert. Implementation and validation of the steady state SP_3 approximation in the GRS FENNECS code. In Proceedings of NENE 2022. 2022.

[41] S. lo Muzio and A. Seubert. Implementation of the steady state simplified P3 (SP3) transport solver in the finite element neutronic code FENNECS, Part 1: Theory. Annals of Nuclear Energy, 200:110303, 2024.

[42] S. lo Muzio and A. Seubert. Implementation of the steady state Simplified P3 (SP3) transport solver in the finite element neutronic code FENNECS, Part 2: Verification. Annals of Nuclear Energy, 200:110304, 2024.

Extended abstract peer reviewed publications

[40] Silvia lo Muzio and Armin Seubert. Validation of the FENNECS SP_3 Solver with Control Rod Insertion Simulations of the ESFR Using Serpent Cross Sections. Proceedings M&C 2023 -The International Conference on Mathematics and Computational Methods Applied to Nuclear Science and Engineering, 2023.

Publications without peer review

[43] Silvia lo Muzio, Armin Seubert, and Liancheng Guo. Simulation of CEFR neutronic start-up tests with FENNECS and coupled pin-by-pin model of a CEFR subassembly. In Proceedings of Young Scientist Workshop at Kerntechnik 2022. 2022.

[39] Silvia lo Muzio and Armin Seubert. Verification of the SP3 solver in FENNECS with C5G7 test cases using HELIOS cross sections. ETSON Conference in Munich, 2022.

Awards

During the doctorate, the following awards were received.

- Young author award at the "31^{st} International Conference Nuclear Energy for New Europe 2022" for the paper [38]
- 2^{nd} Price of the ETSON award at the ETSON conference 2022 for the work [40]
- Performance price for the work performed in 2022 at Gesellschaft für Anlagen- und Reaktorsicherheit (GRS) gGmbH

Abbreviations

Letters

Lower case letters

b	Right hand side of the system of equations, also called load vector
d	Differential
e	Exponential function
f	Expansion coefficient of F
g	Energy group
h	Exponent of the Legendre polynomial
i	Complex number
k_{eff}	Effective multiplication factor
k_{∞}	Infinite multiplication factor
l	Length of the cylinder (dl is the length of the differential cylindrical volume)
lim	Limit
m	Legendre order
n	Legendre order
t	Time
r	Variable indicating the three dimensional spatial dependency
w	Function, continous in the interval $[-1, 1]$
x	First axis on the global coordinate system
x_e	First axis on the local coordinate system
x_0	Fixed point in space on the x-axis
y	Second axis on the global coordinate system
y_e	Second axis on the local coordinate system
v	Neutron velocity
z	Third axis on the global coordinate system
z_e	Third axis on the local coordinate system

Capital letters

A	Surface area
B	Matrix defined as $\int_{\Gamma^e} \nabla\vec{\varphi}^T(\vec{r})\nabla\vec{\varphi}(\vec{r})dV^e, \forall\vec{r} \in e$
C	Matrix defined as $\int_{\Gamma^e} \vec{\varphi}^T(\vec{r})\vec{\varphi}(\vec{r})dV^e, \forall\vec{r} \in e$
D	Diffusion coefficient
E	Energy
F	Spatial distribution of the even order fluxes
G	Slowest energy group
H	Matrix defined as $\int_{\partial\Gamma^e} \vec{\varphi}^T(\vec{r})\vec{\varphi}(\vec{r})d\vec{A}^e, \forall\vec{r} \in e$
J	Number of nodes in a finite element
K	Total number of elements composing the geometry
L	System matrix
N	Highest order of the Legendre polynoamial in 1D and of the spherical harmonics in 3D
$\mathbb{N}$	Set of natural numbers
M	Highest order of the Legendre polynomial in 1D
P	Legendre polynomial
Q	Particle or neutron distribution function
S	Neutron source term
$\tilde{S}$	Extended neutron source, including the scattering between energy groups, fission, and the external neutron source

Greek letters

Lower case Greek letters

α	Coefficient of the boundary condition
β	Coefficient of the boundary condition
γ	Coefficient of the boundary condition
δ	Kronecker delta
ϵ	Basis vector of the coordinate system
θ	Angle between the neutron travelling direction and the x axis of the (global) coordinate system

θ_0	Angle between the neutron travelling direction before and after the scattering event
μ	$cos(\theta)$
μ_0	$cos(\theta_0)$
ν	Number of neutrons emitted per fission reaction
π	Mathematical constant, which is equal to the ratio of the circle circumference to its diameter
$\rho_{leakage}$	Reactivity due to leakage
τ	Coefficient describing the type of external boundary condition
ϕ_0	Zeroth order, or scalar, neutron flux
ϕ_1	First order neutron flux
ϕ_2	Second order neutron flux
ϕ_3	Third order neutron flux
φ	Test, or basis, function of the prismatic finite element
χ	Fission spectrum
ψ	Directional or angular neutron flux distribution
ω	Angle between the neutron travelling direction and the y axis of the (global) coordinate system

Capital greek letters

Γ	Spatial problem domain
Δ	Laplacian operator
Δx	Difference between x and x_0, hence $x - x_0$
Σ	Macroscopic cross section
Ω	Travelling direction

Symbols

∇	Nabla operator or gradient
∂	Partial derivative
$\partial\Gamma$	Boundary of Γ
$\forall$	For all
$\in$	Belonging to

∞	Infinite
$\rightarrow$	Transition from the initial state (left hand side) to the final one (right hand side)
$\Rightarrow$	From which it follows
$=$	Equal to
$\equiv$	Equivalent to/defined as
$\approx$	Approximately equal to
$\cdot$	Product for scalars and scalar product for vectors
$\sum$	Summation
$\int$	Integral
$\cap$	Intersection

Acronyms

1D	One dimensional
3D	Three dimensional
ATHLET	Analysis of Thermal-Hydraulics of LEaks and Transients
CEFR	China Experimental Fast Reactor
CR	Control Rod
ESFR	European Sodium Fast Reactor
FEM	Finite Element Method
GRS	Gesellschaft für Anlagen- und Reaktorsicherheit
HCO	Heat-conduction object
HPMR	Heat Pipe Micro Reactor
HZDR	Helmotz-Zentrum Dresden-Rossendorf
IAEA	International Atomic Energy Agency
LWR	Light water reactor
NSSS	Nuclear Steam Supply System
MMR	Micro Modular Reactor
MOOSE	Multiphysics Object-Oriented Simulation Environment
MWe	Mega Watt electric
P_3	Third order spherical harmonics

PARCS	Pardue Advanced Reactor Core Simulator
PEMTY	Python External Meshing Tool with Yaml input
P_N	N-th order spherical harmonics
PSI	Paul Scherrer Institut
PWR	Pressurized water reactor
RE	Regulating rods
RMS	Root Mean Squared
SA	Subassemblies
SA-1, SA-2, SA-3	Safety rods
SFR	Sodium fast reactor
SH	Shim rods
SMR	Small Modular Reactor
S_N	N-th order discrete ordinate
SP_3	Third order simplified spherical harmonics
SP_3 TR	SP_3 approach using the transport cross section to define the zeroth order diffusion coefficient
SP_N	N-th order simplified spherical harmonics
SPH	Superhomogeneisation
SS	Stainless steel
TFO	thermo-fluid dynamic object
vSMR	very Small Modular Reactor
(v)SMR	(very) Small Modular Reactor

Upper scripts

Lower case letters

e	Finite element within the geometry
h	Exponent of the Legendre polynomial
in	Incoming

Capital letters

I	Interface

R	Reflective
T	Transposed
V	Vacuum
ZF	Zero-flux

Lower case greek letters

η	Coefficient indicating the face of the prismatic finite element

Symbols

$'$	Before the scattering or fission event

Lower scripts

Lower case letters

a	Absorption
b	Boundary
ex	External
f	Fission
g	Energy group
i	Coefficient for the six nodes of the finite element
j	Coefficient for the six nodes of the finite element
k	Coefficient indicating the spatial distribution of the even order fluxes and the zeroth or first order diffusion coefficient
m	Legendre order
n	Legendre order
s	Scattering
t	Total
tr	Transport
x	First axis of the coordinate system
y	Second axis of the coordinate system
z	Third axis of the coordinate system

Capital letters

G	Slowest energy group
N	Order of the spherical harmonics or of the Legendre polynomial

Numbers

0	Zeroth order
1	First order
2	Second order
3	Third order

Hats

$\bar{\square}$	Average
$\tilde{\square}$	Extended neutron source
$\vec{\square}$	Vector

Abstract

The interest in (very) Small Modular reactors ((v)SMRs) and Micro Modular reactors (MMRs) is increasing. These reactor systems show complex geometries and high neutron flux gradients. Therefore, adequate neutronic codes to model such geometries must be developed. To perform the safety assessment of (v)SMRs and MMRs, it is essential to simulate their core behaviour. For the neutronic simulation, one option would be to use transport codes. These provide a high accuracy, but also high computational costs, even if they are deterministic. The required computational resources increase even more in case of Monte Carlo codes. The necessary resources increase drastically for the simulation of transient scenarios. To reduce the computations costs, approximations can be applied to the neutron transport equation. The most widely used is diffusion theory. However, this theory shows limitations for small and heterogeneous configurations, which are characteristic of (v)SMRs and MMRs. Therefore, it arises the necessity to find an alternative approximation to the neutron transport equation, capable to compute calculations in a shorter time, compared to transport simulations, and providing a higher accuracy compared to diffusion theory.

One possibility is to use the SP_3 approximation. This is derived from the one dimensional P_3 approximation, which is obtained by expanding the angular terms of the neutron transport equation with the first four Legendre polynomials. To obtain the SP_3 equations, the one dimensional P_3 approximation is transformed to three dimensions, keeping the Legendre polynomials, without replacing them with spherical harmonics.

In order to perform the safety assessment of (v)SMRs and MMRs, the GRS neutronics code FENNECS, based on the finite elements approach, was equipped with a steady state SP_3 solver. Therefore, beside the derivation of SP_3 methodology, including its boundary conditions, it was necessary to obtain the Galerkin form of the steady state SP_3 equations. To implement them in FENNECS, algorithms were designed and implemented in the code.

The solver implementation was followed by its verification. Within this process, test cases with various geometry complexities and sizes as well as with a different amount of energy groups in the macroscopic cross section libraries were used. Firstly, exercises with given homogenised neutron macroscopic cross sections libraries, defined

by the authors of the benchmark, were modelled. This allowed to prove the correct implementation of the solver, excluding effects caused by the cross section generation. Secondly, examples where the libraries were generated using codes capable to calculate homogenised multi-energy-group neutron macroscopic cross sections were used to verify the new solver. The results were assessed based on several parameters: effective multiplication factor, normalized power and neutron distributions, loss in reactivity due to the leakage, as well as control rod worth. The results of the FENNECS SP_3 solver were evaluated with respect to a reference, obtained from more accurate codes, like for example transport based ones, in order to calculate the deviation of the obtained results. For most of the test cases, the evaluation involved also other SP_3 solvers to show that the new FENNECS solver calculates similar results. Additionally, the outcomes were also compared to diffusion solvers to evaluate the improvement in accuracy, which arises from the application of a more expensive methodology.

From the verification process, based on the comparison of the results of the FENNNECS SP_3 solver with other SP_3 solvers, as well as with transport or Monte Carlo codes, the proper functionality of the new FENNECS steady state SP_3 solver was proven. In addition, based on the test cases analysed, the limitations and strengths of this methodology were identified. With this regards, very good results were obtained by the new FENNECS SP_3 solver for example for the Hébert benchmark, as well as the fuel assemblies of the C5G7 benchmark. On the contrary, the new solver showed difficulties in modelling configurations with fully inserted control rods. Furthermore, for the FENNECS code, the improvement in accuracy due to the application of the SP_3 methodology, with respect to diffusion theory, was evaluated. Concerning this point, it was proven that increasing the heterogeneity of the geometries, a larger improvement of the results can be obtained using the FENNECS SP_3 solver, instead of the diffusion approximation. For the scenarios with fully inserted control rods, using the FENNECS diffusion solver with SPH corrected cross sections delivered better results, than the SP_3 methodology, where no corrections were applied to the nuclear data.

Zusammenfassung

Ein steigendes Interesse in (v)SMRs und MMRs kann zur Zeit beobachtet werden. Diese weisen komplexe Geometrien und hohe Neutronenfluss-Gradienten auf. Aus diesen Grund besteht die Notwendigkeit passende Neutronikcodes für deren Sicherheitsbewertung zu entwickeln. Das Reaktorkernverhalten von (v)SMRs und MMRs zu simulieren ist essentiell um deren Sicherheitsbewertung durchzuführen. Eine Möglichkeit für die Neutroniksimulation besteht darin Transportcodes zu verwenden, welche eine hohe Genauigkeit bieten. Codes die auf diesem Prinzip basieren haben jedoch hohe Rechenkosten, auch wenn diese deterministisch sind. Die notwendigen Rechenressourcen steigen weiter im Fall von Monte Carlo Codes. Dies führt dazu, dass Simulationen von Transienten, basierend auf deterministischen Transportcodes oder Monte Carlo Codes, für alltägliche Berechnungen nicht verwendet werden können. Näherungen können auf die Transportgleichung angewandt werde um die Rechenkosten zu reduzieren. Die am meisten genutzte Näherung ist die Diffusionstheorie. Diese Theorie weißt jedoch Beschränkungen auf für kleine und heterogene Geometrien, die für (v)SMRs und MMRs charakteristisch sind. Aus diesem Grund besteht die Notwendigkeit eine alternative Näherung zur Transporttheorie zu finden, die Rechnungen in kürzerer Zeit als die Transportsimulation und mit höherer Genauigkeit als die Diffusionstheorie ermöglicht.

Eine Möglichkeit ist die Verwendung der SP_3 Näherung. Diese wird aus der eindimensionalen P_3 Näherung hergeleitet. Die P_3 erhält man durch das Entwickeln nach den ersten drei Legendre Polynomen der winkelabhängigen Terme in der Transportgleichung. Um die SP_3 Gleichungen zu erhalten wird die eindimensionale P_3 Näherung in 3D gebracht, wobei die Legendre Polynome beibehalten werden und diese werden nicht durch sphärische harmonische Funktionen ersetzt.

Um die Sicherheitsbewertung von (v)SMRs und MMRs zu ermöglichen wurde, der GRS Neutronikcode FENNECS, welche auf der Finite Elemente Methode basiert, mit einen stationären SP_3 Löser ausgerüstet. Aus diesem Grund war es nötig die Galerkin Form der stationären SP_3 Gleichungen, inklusive Randbedingungen, zu herleiten. Darauf basierend wurden Ad-hoc Algorithmen entwickelt und in den Code implementiert.

Auf die Implementierung des Lösers folgte dessen Verifizierung. Diese beinhaltete Testfälle mit verschiedenen Geometriekomplexitäten und -Größen

und mit unterschiedlicher Anzahl an Energiegruppen bei den makroskopischen Wirkungsquerschnitte. Erstens wurden Beispiele gerechnet mit vorgegebenen homogenisierten maskroskopischen Wirkungsquerschnittsbibliotheken. Das erlaubte die Funktionalität des neuen Löser zu zeigen. Danach wurden Modelle gerechnet in denen die Bibliotheken mittels Programmen erzeugt wurden, die homogenisierte Mehrenergiegruppen-Wirkungsquerschnitte berechnen können. Für die Ergebnisauswertung wurden die effektiven Multiplikationsfaktoren genutzt. In einigen Fällen wurde die Auswertung ergänzt durch Vergleiche mit der normalisierten Leistungs- oder Neutronenflussverteilungen oder des Reaktivitätsverlustes aufgrund der Leckage oder der Steuerstabswirksamkeit. Die Ergebnisse des FENNECS SP_3 Lösers wurden im Verhältnis zu einer Referenz ausgewertet, die von einem genaueren Code berechnet wurde, wie z.B. einem Transportcode, um die Abweichung der Ergebnisse zu auswerten. Die Auswertung der meisten Testfälle involvierte auch andere SP_3 Löser, um zu beweisen dass der neue FENNECS SP_3 Löser ähnliche Ergebnisse liefert. Zusätzlich wurden die Ergebnisse auch mit Diffusionslösern verglichen, um die Verbesserung der Genauigkeit zu quantifizieren, welche durch die Anwendung des rechenintensiveren SP_3 Lösers erhalten wird.

Die Funktionalität des stationären FENNECS SP_3 Lösers wurde im Rahmen des Verifizierungsprozesses bewiesen. Dafür wurden die Ergebnissen aus dem FENNECS SP_3 Löser mit denen aus verschiedenen SP_3 Lösern, Transportlösern und auch Monte Carlo Codes genutzt. Zusätzlich, basierend auf den betrachteten Testfällen, wurden die Beschränkungen und Stärken dieser Methode identifiziert. Diesbezüglich lieferte der FENNECS SP_3 Löser sehr gute Ergebnisse, z.B. im Fall des Hébert Benchmark und der Brennelemente des C5G7 Benchmarks. Im Gegensatz dazu wies der neue Löser Schwierigkeiten bei der Modellierung von Zuständen mit komplett eingefahrenen Kontrollstäben auf. Außerdem wurde für FENNECS die Verbesserung der Genauigkeit unter der Verwendung der SP_3 Methode, im Verhältnis zur Diffusionstheorie, ausgewertet. Diesbezüglich, wurde gezeigt, dass mit steigende Heterogenität der Geometrie, eine größere Verbesserung der FENNECS SP_3 Ergebnisse beobachtet werden kann, im Verhältnis zur Diffusionsnäherung. Für das Szenario mit komplett eingefahrenen Kontrollstäben wurden bessere Ergebnisse mit dem FENNECS Diffusionlöser mit SPH korrigierten makroskopische Wirkungsquerschnittbibliotheken geliefert, als die aus dem SP_3 Löser, der keine Wirkungsquerschnittskorrektur nutzt.

Contents

Chapter 1

Introduction

1.1 Motivation

In order to design efficient reactors, which fulfil the economic operation and inherent safety requirements, it is essential to predict their behaviour. For this purpose, nuclear simulation codes are a very powerful tool: they allow to simulate operational as well as incident scenarios, allowing to estimate consequences of potential accidents, which can be considered in the design, in order to prevent and mitigate them. The reliable and safe operation of a reactor is coupled to the reliability of its simulation [19]. This means that using simulations results, which precisely predict reactor core parameters, like the neutron flux, is of vital importance. To precisely calculate the neutron flux allows to accurately predict criticality, power and temperature distributions as well as feedback coefficients of reactivity, hence the reactor behaviour. Therefore, it arises the necessity to have a tool to reliably simulate the neutronic behaviour of the reactor. The tool must be developed such that it is able to reliably model compact cores, like Micro Modular Rectors (MMR) and (very) Small Reactors ((v)SMR), which are of big interest nowadays, due to the advantages that will be explained in subsubsection 1.1.2.2. Reliable simulations are of vital importance in order to be able to perform the safety assessment of these reactor systems.

The idea behind neutronic simulation programs is to solve the equation describing the neutronic behaviour of the system. Therefore, an appropriate equation describing it, which takes into account the neutrons gain and loss phenomena, taking place in the nuclear reactor core, must be found [13, 64].

1.1.1 Calculation method

1.1.1.1 The neutron transport equation

A possible approach is to use the neutron transport equation, or Boltzmann equation, which is derived performing a neutrons balance on the differential volume element, as it will be shown in chapter 3. This equation accurately describes the directional neutron flux in an inhomogeneous fissile medium, considering neutron scattering, fission, capture and external neutron sources, as well as neutrons streaming in and out of the control volume [15].

However, to solve the transport equation is difficult and costly, due to the presence of seven independent variables: five of them describe the space-angular dependency and the remaining two account for the time and the energy [4, 13, 34]. In order to reduce the computational costs as well as the calculations duration, approximations must be applied to the transport equation.

1.1.1.2 The diffusion approximation

The most widely used approximation is the diffusion theory. To derive the diffusion equation, which is based on the Fick's law, the following assumptions are applied on the neutron transport equation:

1. scattering is isotropic,
2. neutron absorption is much less probable than scattering, hence $\Sigma_a << \Sigma_s$,
3. the neutron flux varies slowly in space (the first-order Taylor expansion can be applied)

[4, 16, 44, 57].

The first assumption is fulfilled in case of low energy neutron scattering with heavy mass nuclei [16]. The second point is not true for strong absorbers, which are the constituents of the control elements in a nuclear reactor [16, 20]. Furthermore, for large (compared to the mean free path, defined as the inverse of the macroscopic total cross section) homogeneous media, having an uniform source distribution, the third condition is satisfied only a few neutron mean free paths away from the medium boundary [16]. Therefore, this last point is not applicable for compact cores, e.g. MMRs and (v)SMRs and near material interfaces [6, 16]. The complete derivation of the diffusion theory can be found for example in [57].

1.1.1.3 The third order simplified spherical harmonics (SP_3) approximation of the neutron transport equation

Due to the inapplicability of the diffusion approximation on MMR and (v)SMR, discussed in subsubsection 1.1.1.2, and the high costs for solving the Boltzmann equation, addressed in subsubsection 1.1.1.1, it arises the necessity to find an alternative approximation to the transport equation, which allows to describe the neutronic behaviour in compact cores. A suited candidate for this task is the N-th order Simplified Spherical Harmonics, or SP_N, approximation. Its results are more accurate compared to the diffusion approximation, since it considers a larger part of the transport effects [46]. This approach is derived from the N-th order Spherical Harmonics, or P_N, approximation of the neutron transport equation [4]. Here, functions present in the Boltzmann equation, which show a directional dependency, are expanded with the first N spherical harmonics functions [4, 65]. The three-dimensional SP_N approximation is obtained from the one-dimensional P_N equations by replacing the 1D spatial differential operators by the 3D differential operators [4, 46]. The advantage of the SP_N, with respect to the P_N approximation, is the reduced calculation time, due to the smaller number of coupled differential equations, without showing a substantial reduction in the computational accuracy [4, 46].

In this work, the SP_N method with $N = 3$ is chosen. The choice of the third order Simplified Spherical Harmonics, or SP_3, approximation of the neutron transport equation is motivated by the reduced amount of memory and computational time required by this approach compared to higher order SP_N equations. Furthermore, the SP_3 method is constituted by two equations having a similar structure to one of the diffusion approximation [4]. Therefore, it can be implemented more easily in programs, which already provide a diffusion solver [4].

1.1.2 Nuclear reactors with compact cores

1.1.2.1 Definition

Reactors with compact cores include (v)SMRs as well as MMRs. The first part of the acronym, hence "(very) small" and "micro" is related to their size as well as to the delivered power rating [3, 54]. The reduced size causes a high leakage, due to the low volume to surface ratio, leading to large flux gradients [54]. Regarding their power rating, according to the International Atomic Energy Agency (IAEA), if this parameter is below $300MWe$, the facility is considered as a Small Modular Reactor (SMR) [3]. In particular, very Small Modular Reactors (vSMRs), a subcategory of SMRs, are

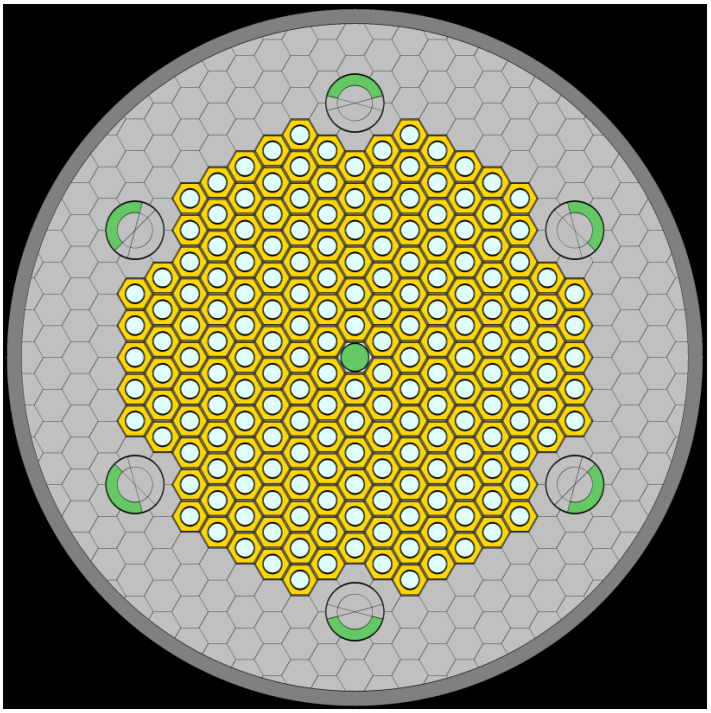

Figure 1.1: Geometry of the Hot Pipe Micro Reactor (HPMR) with control drums. The figure was taken from [30].

distinguished by the power rating below $15MWe$ [3]. MMRs are generation-IV reactors, having a power rating between $1MWe$ and $20MWe$ [3].

The second letter of the acronym, hence the concept of "modular", is related to their construction, which allows to achieve a serial production [31]. This can be accomplished only for reactor concepts having a power ratio below the upper limit of SMRs [31]. The modularization concept is applied to the unit assembly of the nuclear steam supply system (NSSS) [31]. This can be assembled from one or multiple modules, depending on the desired power rating [31]. Furthermore, the modules can be added over time [31].

Additionally, these systems are characterised by irregular, complex and strongly heterogeneous geometries [54]. Their configuration can deviate from the regular lattices [54]. Furthermore, they can show a heterogeneous material composition due to the presence of special fuels and controlling elements, like for example control drums [54], as shown in Figure 1.1.

1.1.2.2 Advantages

The modular construction offers multiple advantages. Firstly, it allows to adapt the desired output power over time [31]. Therefore, this parameter can be changed to fit

the regional load growth or to compensate for old generating stations, which are being dismantled [31].

Secondly, from this characteristic, it follows a second advantage: the possibility to invest less at the beginning, giving the chance to increment the investment, hence the power output, over time [31]. Therefore, at the beginning, the financial risk is reduced [31]. Nevertheless, there is the possibility to increment the investment by using the revenues to increase the desired power by adding modules [31].

Thirdly, the building time is less compared to big facilities [31]. In case of large nuclear reactors, the desired power output must match the load needed many years in the future [31]. On the contrary, here, a projection of the load demand in just a few years must be done, still having the chance to increment the power output later on [31].

Fourthly, remote regions can be supplied matching their small loads [31]. For the same reason, they are used also for industrial applications [31].

Finally, one advantage of MMRs, over (v)SMRs, is their transportability [3]. For all the reasons stated here, the interest in these concepts is increasing.

1.2 Objectives

Due to the increasing interest in (v)SMRs and MMRs, motivated in subsubsection 1.1.2.2, it arises the need to develop a neutronic tool, able to reproduce the characteristics of these systems, listed in subsubsection 1.1.2.1, in order to perform their safety assessment. For this reason, a steady state SP_3 solver is implemented in the neutronics code Finite ElemeNt NEutroniCS (FENNECS), developed at Gesellschaft für Anlagen- und Reaktorsicherheit (GRS) gGmbH, which relies on the finite elements method and it offers a high geometrical flexibility. Then, its verification is carried out. As described in section 2.2, this code already provides a diffusion solver. Therefore, as discussed in the previous paragraph, it results convenient to implement an SP_3 solver here.

1.3 Methodology

To achieve the goals of this work, discussed in section 1.2, a work plan is developed. As shown in Figure 1.2, this includes multiple working packages, grouped in the following three phases:

- theoretical derivation of the steady state SP_3 methodology in the Galerkin formalism
- implementation of the steady state SP_3 solver in the FENNECS code
- verification of the steady state SP_3 solver.

The packages included in the three phases have to be completed in the order shown.

Firstly, the theoretical derivation of the SP_3 approximation is carried out. The first step here is to set up the neutron transport equation in 3D as in subsection 3.1.1, which is then simplified to 1D, as shown in subsection 3.1.2. Since no transient scenarios are of interest in this work, the time dependency is removed, as in subsection 3.1.4. Expanding the angular terms present in the steady state transport equation in 1D with the first N Legendre polynomials, the steady state P_N approximation in 1D is obtained in subsection 3.2.2. By imposing $N = 3$, in section 3.3, which includes [41], the P_3 approximation in 1D is obtained, from which, performing a simplified transition to 3D, the steady state SP_3 equations in 3D is set up. In addition, also the boundary conditions, are obtained. These are then included in the two SP_3 equations. In [41], also the last step of this phase is performed, which consists in obtaining the Galerkin representation of the steady state SP_3 equations, including the boundary conditions. This step is essential for the implementation of the equations in a finite element based code, like FENNECS.

Secondly, ad hoc algorithms are designed to solve the Galerkin form of the SP_3 equations and these can be found in section 3.3. The required algorithms are created from scratch or they are designed expanding the idea behind the ones used for the diffusion solver. The algorithms of the first step of the second phase are then written in the same programming language as FENNECS, hence FORTRAN, and included in the GRS neutronics program.

Thirdly, in the last phase, explained in chapter 4, the verification of the new solver is carried out. At the beginning, this is performed using test cases, where the macroscopic cross section libraries were not generated, but freely defined by the authors of these exercises. This step allows to prove the correct functionality of the work designed in the second phase, excluding effects of the cross section generation process. Then, to show also the applicability of the new SP_3 solver on realistic nuclear data, test cases with macroscopic cross section libraries generated with appropriate programs are simulated. For the analysis, reference results, obtained from a more accurate approach, than the one of the FENNECS SP_3 solver, were used. For example, in many test cases, the reference results were obtained with Monte Carlo codes. Deviations, with respect to the reference, were calculated for the results of the FENNECS SP_3 solver, as well as

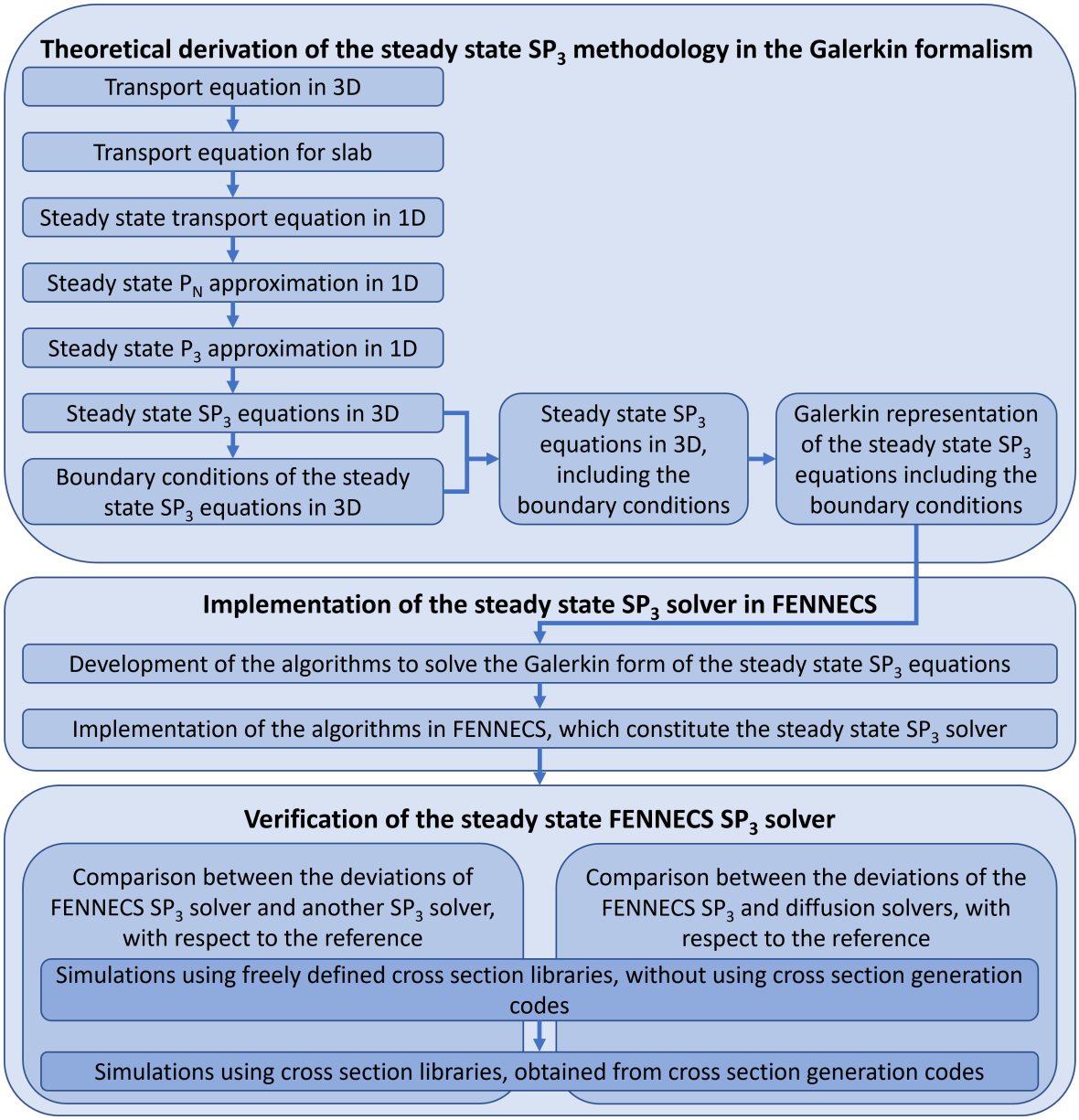

Figure 1.2: Working packages for the implementation and verification of a steady state SP_3 solver in FENNECS.

other SP_3 and diffusion solvers. Comparing the deviations of the FENNECS SP_3 solver with the ones of other SP_3 solvers has the goal to prove the correct implementation of the new FENNECS solver. The evaluation of the results deviations for the FENNECS SP_3 solver and diffusion solvers aims to evaluate the gain in accuracy by using the new method.

Finally, in chapter 5, the conclusions can be found. Additionally, further improvements and extensions of the code are proposed.

Chapter 2

State of the art

The aim of this chapter is to give to the reader a short overview of the available neutronic codes. In section 2.1, this topic will be addressed with the focus on the applicability on compact cores, like (v)SMRs, and MMRs, whose characteristics were described in subsubsection 1.1.2.1. Finally, in section 2.2, the features of FENNECS will be shown. In particular, in subsection 2.2.2, an application of the FENNECS code, performed before the implementation of the SP_3 solver, will be shown.

2.1 Neutronics codes available

Two main options are available to model the neutronic behaviour of reactor systems with a high neutron leakage as well as complex and irregular geometries, as (v)SMRs MMRs. The first one is to use Monte Carlo codes, which will be discussed in subsection 2.1.1. The second option is given by deterministic codes and some examples will be given in subsection 2.1.2.

2.1.1 Monte Carlo codes

Monte Carlo codes allow to get the best available knowledge regarding the neutron interactions [36]. Additionally, this kind of codes offers a high geometrical flexibility, which is particularly advantageous for complex and irregular geometries, like the ones of (v)SMRs and MMRs [63]. Furthermore, this family of codes is able to calculate group constants [36]. Beside these powerful advantages, this method suffers also from limitations. The biggest disadvantage is the large requirement of computational resources, which makes them unsuited for routine calculations as well as for transient simulations [36]. Additionally, it should be considered that the results are obtained

through a stochastic process [27].

An example of a Monte Carlo code is Serpent, which has been developed at the VTT Technical Research Centre in Finland [35]. In particular, it is a 3D continuous energy code [36]. In this work, Serpent will be used in chapter 4 for the generation of the multi-energy-groups macroscopic cross sections libraries as well as to calculate the reference results.

2.1.2 Deterministic codes

On the contrary to Monte Carlo codes, deterministic codes provide an exact solution [36]. Furthermore, they are computationally cheaper, allowing them to perform transient calculations [36]. In the next paragraphs, some examples for this type of codes will be given.

One example of 3D neutron kinetics code suited for complex geometries is GeN-Foam, which has been developed at the Paul Scherrer Institut (PSI) [22]. It is a multiphysics code based on OpenFOAM, offering originally only a diffusion solver [21]. The discretization and solution of the partial differential equations are performed using the Finite Volume Method [21]. GeN-Foam couples three sub-solvers, which treat the thermal-hydraulics, thermal-mechanics, and neutron diffusion [21]. Successively, to better model the CROCUS reactor [48], an SP_3 solver was included [22].

A second example is Rattlesnake that has been developed at the Idaho National Laboratory [61]. It is an application for the calculation of radiation transport, based on MOOSE (Multiphysics Object-Oriented Simulation Environment) [61]. In the code, this phenomenon is described with the linear Boltzmann transport equation or the radiation transport equation, depending on whether the neutron flux or radiation is of interest [61]. The geometry discretization is performed by finite elements with an unstructured grid [60, 61]. The angular discretization is performed with the diffusion approximation, the discrete ordinates (S_N), as well as the spherical harmonics (P_N) expansion method [61].

A further example is DYN3D. It has been developed at the Helmholtz-Zentrum Dresden-Rossendorf (HZDR) [19]. DYN3D is capable to model quadratic as well as hexagonal lattices [7]. It solves the steady state as well as transient diffusion equation [7, 25]. Successively, it was equipped with a steady state SP_3 solver [19]. To solve the neutronic equation, the nodal expansion method is used [7]. Additionally, DYN3D has been already coupled to the thermal hydraulics codes Analysis of THermal-hydraulics of LEaks and Transients (ATHLET) and RELAP5/MOD3 [25].

An additional code is the Purdue Advanced Reactor Core Simulator (PARCS). However, its SP_3 solver can be used only to calculate Cartesian geometries [18]. The multigroup calculation can be performed for steady state as well as transient scenarios [18]. PARCS provides a two group diffusion solver, as well as an SP_3 solver [18].

The last example is FEMFUSION [58], which is based on the finite element method. The continous Galerkin approach is used for the spatial discretization [58]. It is capable to solve the multigroup diffusion as well as the SP_N equations in up to three dimensions [23]. This code is open source and written in C++ [14, 59].

Further examples of neutronic codes will be encountered in chapter 4. Here, these will be used, together with some of the programs mentioned here, to perform the verification of the SP_3 solver in FENNECS.

2.2 FENNECS

2.2.1 Main features of FENNECS

The SP_3 approximation of the neutron transport equation was implemented in FENNECS, a 3D few-group neutron kinetics code, based on the finite element method (FEM) [55]. This code does not show limitations for the modelling of (v)SMRs or MMR, like it was the case for some of the codes listed in section 2.1, which suffered, for example, from a long calculation duration, or a limitation to two energy groups.

Before the implementation of the SP_3 solver, FENNECS provided the solution of the time dependent as well as steady state three dimensional few-group diffusion equation in the Galerkin finite element representation [9, 55]. Upright triangular prism with linear basis functions are used as spatial elements [9, 55].

The meshing can be performed for regular quadratic and hexagonal lattices, using the internal meshing module. Besides this tool, a further tool to generate the mesh data needed by FENNECS is offered, which is the Python External Meshing Tool with Yaml input (PEMTY) [8]. This can be used also in case of irregular geometries, typical of (v)SMRs, and MMRs [8, 9]. For example, it is able to model also control drums [9].

In order to get the thermal-hydraulic feedback, FENNECS can be run coupled to ATHLET [8, 9]. Macroscopic cross sections libraries in NEMTAB format are required to run the calculations [9]. This holds for coupled as well as stand-alone calculations. Furthermore, the libraries can be parametrized with respect to up to six thermal-hydraulic feedback parameters using linear cross-section interpolation [9]. In

addition, to accelerate the convergence of the eigenvalue problem, Wieland iteration can be applied [55]. FENNECS also allows to perform pre- and post-processing for displaying the input geometry and the materials distribution as well as the distribution of the output parameters, like the power density, the neutron flux and thermal-hydraulic quantities [9].

2.2.2 Demonstration of FENNECS applications

In this section, an application of the FENNECS diffusion solver will be shown. Here, the China Experimental Fast reactor (CEFR) was modelled and compared to the results obtained with Serpent [43].

SIMULATION OF CEFR NEUTRONIC START-UP TESTS WITH FENNECS AND COUPLED PIN-BY-PIN MODEL OF A CEFR SUBASSEMBLY

Silvia lo Muzio
Gesellschaft für Anlagen- und Reaktorsicherheit (GRS) gGmbH
Forschungszentrum, Boltzmannstr. 14, D-85748 Garching, Germany
silvia.lo-muzio@grs.de

Armin Seubert, Liancheng Guo
Gesellschaft für Anlagen- und Reaktorsicherheit (GRS) gGmbH
Forschungszentrum, Boltzmannstr. 14, D-85748 Garching, Germany
armin.seubert@grs.de, liancheng.guo@grs.de

ABSTRACT

Within the frame of the IAEA Coordinated Research Program I31032, FENNECS was used to simulate Neutronic Start-up Tests, performed at the China Experimental Fast Reactor (CEFR). The FENNECS simulations showed a good agreement with the measurements as well as with the results obtained by Serpent. In addition, a high-fidelity coupled FENNECS/ATHLET model of a single CEFR fuel assembly using pin cell-homogenized and parameterized cross section libraries was developed for first test calculations.

CEFR NEUTRONIC START-UP TESTS

The China Experimental Fast Reactor CEFR is a pool-type sodium cooled fast reactor with a thermal power of 65 MW and UO_2 as fuel. The first core loading consisted of up to 79 fuel subassemblies (SA), 8 control SAs, one neutron source SA, 394 stainless steel (SS) SAs, and 230 boron shielding SAs. The control SAs comprehend two regulating rods (RE-1 and RE-2) and three shim rods (SH-1, SH-2, SH-3), which form the first shut down system, as well as three safety rods (SA-1, SA-2, SA-3), constituting the second shut down system. In the shim and safety rods, the enrichment of ^{10}B in the B_4C absorber is 90% and 20% in the regulating rods.

During the CEFR physical start-up in 2010, the obtained measurements of several experiments (e.g., net criticality, control rod integral and differential worth, void reactivity effects and subassembly exchange reactivity effects [1]) were provided in the frame of an IAEA CRP for benchmark analysis.

THE NEUTRON KINETICS CODE FENNECS

The Finite ElemeNt NEutroniCS code FENNECS is a steady-state and time-dependent 3-d few-group finite element-based diffusion code [2][3]. It applies the continuous Galerkin weighted residual approach using upright triangular prisms with linear basis functions as spatial elements. FENNECS provides a high geometrical flexibility that allows to model complex and irregular geometries. For the spatial meshing of the problem geometry, the Python Enhanced Meshing Tool with Yaml input PEMTY is developed [4]. PEMTY can also provide the mesh with pin cell-wise resolution for high-fidelity coupled simulations of cartesian and hexagonal lattices, as well as of e.g., control drums.

FENNECS requires macroscopic cross sections libraries in a NEMTAB-like format that may be parameterized with respect to thermal hydraulic feedback parameters with linear cross section interpolation. Thermal-hydraulic feedback is considered by a coupling with the GRS thermal-hydraulic system code ATHLET [5].

MONTE CARLO MODELS IN SERPENT

Two types of Monte Carlo models were built to provide a comparison for FENNECS and to generate the cross sections. For both, the Serpent version 2.1.31 with ENDF/B-VII.0 nuclear basis data was used. To compare the FENNECS results of the start-up tests, full core Monte Carlo calculations were performed. Here, the geometry was reproduced in detail. The thermal expansion was considered in the geometric dimensions as well as in the mass and nuclide densities using linear thermal expansion correlations. This effect was included in the Monte Carlo simulations using an extended Serpent version [6] based on version 2.1.31. For the cross sections generation, a single full-scale fuel assembly was modelled in a radial infinite lattice. Assemblies containing non-fissile materials were simulated using supercell models (according to the approach described in [7]): the model includes a non-fuel assembly surrounded by six fuel SAs halves. The macroscopic cross sections are generated in 10 energy groups.

DETERMINISTIC MODELS IN FENNECS

In the FENNECS model of the CEFR, each hexagonal assembly is composed radially by at least six triangular prismatic finite elements. The axial mesh size ranges between 0.006 cm and 7 cm, leading to 58 layers. Consequently, the geometry comprehends 247776 elements, represented by 131924 nodes.

The nuclear data generated by Serpent were directly used as input for FENNECS, except the absorption cross sections of strong neutron absorbers, hence the highly enriched B_4C axial section, located in shim and safety rods. A suited correction must be applied to these cross sections to avoid that the reactivity of the control rods is overestimated. Therefore, the absorption cross sections of the highly enriched B_4C axial section were multiplied by an iteratively determined factor of 0.9158333 (applied to all energy groups) such that FENNECS exactly reproduces the Serpent multiplication factor of $k_{eff} = 1.01427$.

SIMULATION RESULTS OBTAINED BY FENNECS

FUEL LOADING AND CRITICALITY

Before the start-up, the fuel positions were loaded with mock-up fuel SAs. Criticality was reached by substituting them stepwise with fuel SAs. Actually, during the experiment at the CEFR, when the core was loaded with 71 fuel SAs, this was subcritical, as foreshown by the calculation. FENNECS predicted supercriticality with 72 fuel SAs. Accordingly, the final criticality state was reached with 72 fuel rods at a measured temperature of 245 °C and with RE2 positioned at 70 mm, as shown in Table 1.

Table 1: Core states and criticality obtained for various fuel loading with 7 control rods out of the core.

Number of fuel SAs loaded	Position of RE2	Core state	keff FENNECS	keff Serpent	Reactivity difference w.r.t. Serpent (pcm)
70	Out-of-core	Subcritical	0.99296	0.99533	-240
71	Out-of-core	End of subcritical process	0.99751	0.99936	-186
72	190	Supercritical	1.00146	1.00301	-154
72	70	Critical (Predicted)	1.00100	1.00260	-159

CONTROL ROD WORTH

During the control rod worth experiments, the core uniform temperature was 250°C and it contained 79 fuel assemblies and two additional SS SAs. The control rod worth is derived from the reactivity difference arising from the insertion of one or multiple rods. 14 scenarios were simulated and their description, together with the obtained results, can be found in Figure 1. The FENNECS results agree with the experiments within the measurement errors and slightly overestimate the rod worths, except for RE1 and RE2. For RE2, SA3 and the first shutdown system with SH1 stuck, the highest discrepancies (up to 14 %) were observed. In the other cases, the difference was below 4.2%.

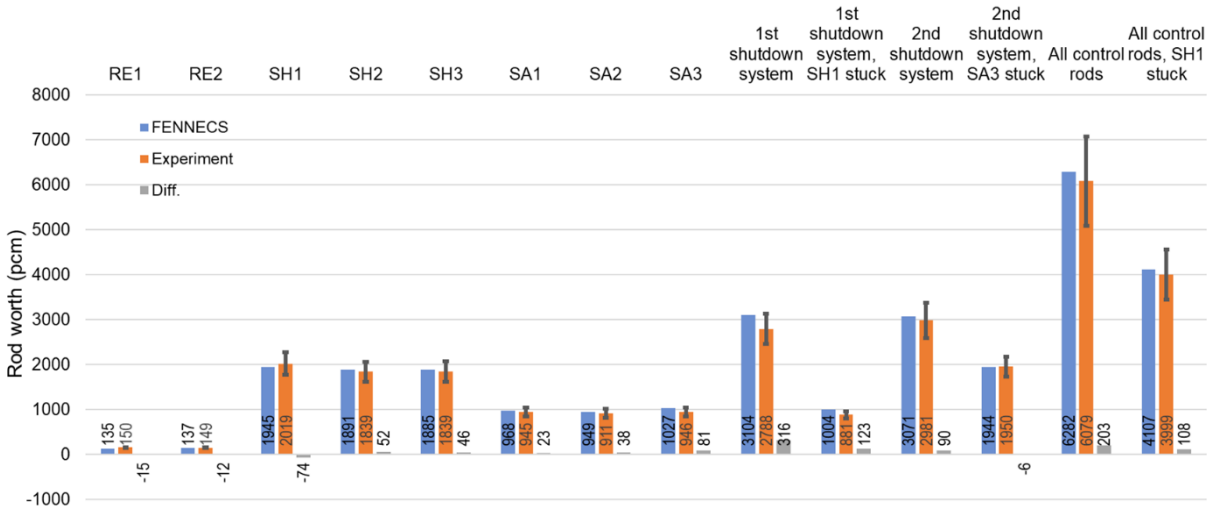

Figure 1: Control rod worth simulations obtained with FENNECS (blue) in comparison with measurements (orange). Differences are shown in grey bars. Error bars denote measurement errors.

Additionally, integral and differential control rod worth curves were determined with FENNECS as well as with Serpent. From both graphs, depicted in Figure 2, the different characteristics of the SAs are clearly visible: regulating rods, containing natural ^{10}B abundance, show flatter curves compared to rods made of enriched ^{10}B. For all rods, the FENNECS results satisfactory match the Serpent simulations.

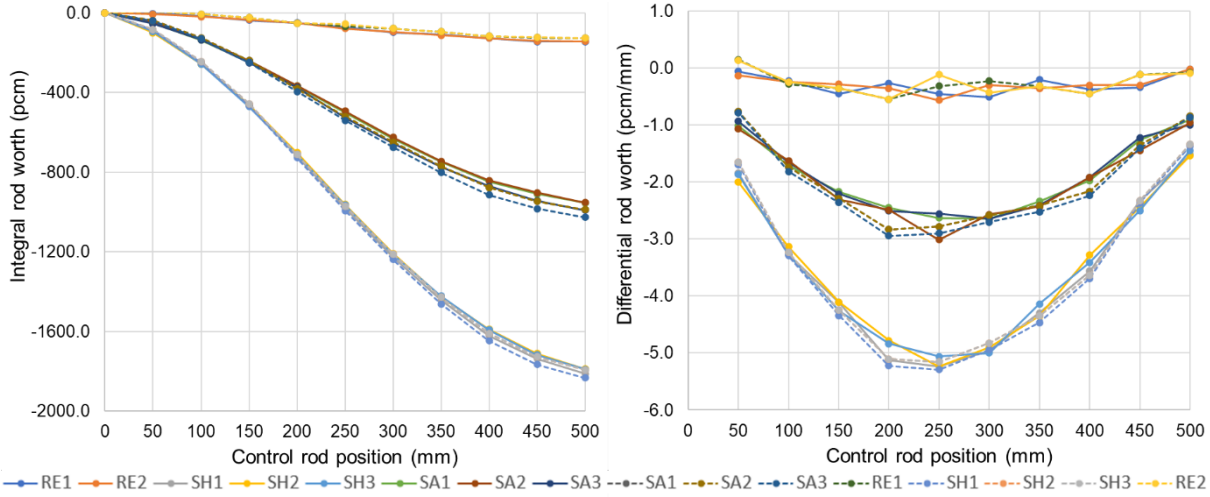

Figure 2: Integral (left) and differential (right) control rod worth curves for the eight control rods obtained by FENNECS (solid lines) and compared with Serpent (dashed) lines.

SODIUM VOID REACTIVITY

The sodium void reactivity is measured by replacing a fuel rod with a voided one in combination with the measurement of the change in the critical control rod position. The replaced SA are marked with blue labels in the right panel of Figure 3.

As shown in the left panel of Figure 3, the void reactivity is negative for all measurement positions. This can be attributed to the small size of the CEFR. Therefore, the (negative) neutron leakage contribution dominates over the positive spectrum hardening effect due to the voiding. Even though, the measurements are slightly overestimated, the FENNECS results are within the measurement errors.

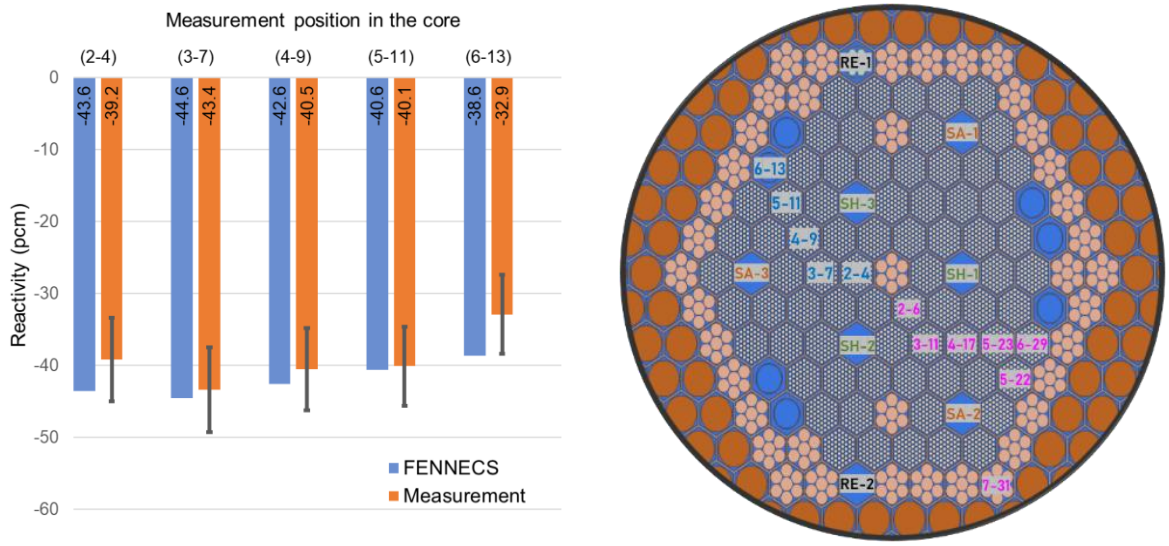

Figure 3: Left: Sodium void reactivity calculated by FENNECS (blue) in comparison with measurements (orange). Error bars denote measurement errors. **Right:** Active core region with assembly labels.

SUBASSEMBLY SWAP REACTIVITY

To simulate the consequences of fuel loading errors, the swap reactivities were measured for 6 fuel rods and 2 SS SAs that are indicated with pink labels in the right panel of Figure 3. In this experiment, the positions of single control rods as well as multiple rods were adjusted and the results can be seen in the left and right panel of Figure 4, respectively. FENNECS slightly underestimates the measured swap reactivities, with deviations between 27 pcm and 118 pcm. However, all calculation results are still within the measurement uncertainties.

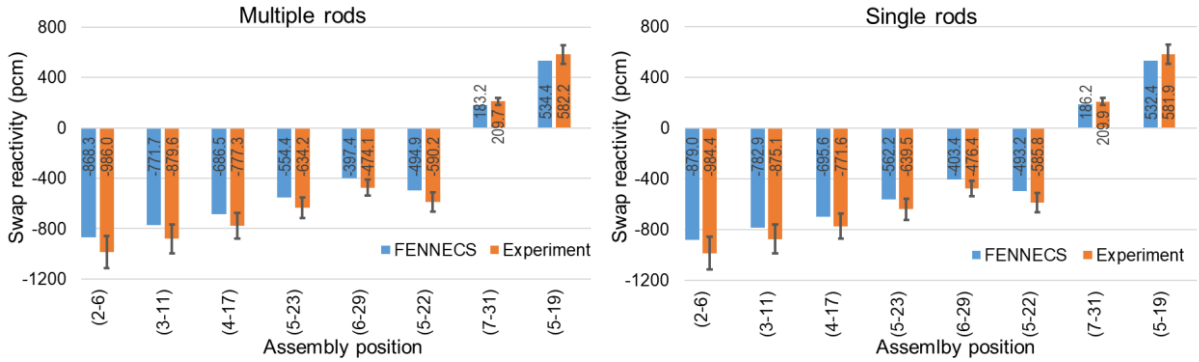

Figure 4: FENNECS results (blue) for the control rod swap reactivities obtained by multiple (left) and single control rods (right) in comparison with measurements (orange). Error bars denote measurement errors.

COUPLED PIN-BY-PIN FENNECS/ATHLET MODEL OF A CEFR SUBASSEMBLY

In the scope of this work, coupled pin-by-pin FENNECS/ATHLET models of the active axial section of a single CEFR fuel assembly and a minicore using pin cell-homogenized and parameterized cross section libraries were developed. This extends the coupled high-fidelity multiphysics simulation methods already available for LWR [8][9][10] to Generation IV and other innovative systems.

Although there are considerable efforts in extending the subchannel code CTF to simulate sodium [11], a release of CTF for sodium is not yet available. Therefore, fluid dynamic and heat transfer are simulated by the thermal hydraulic system code ATHLET [12] in a subchannel-like approach [13]. In this model, the parallel subchannels of the sodium flow around pins, which included 37 inner, 18 edge and 6 corner ones (see left panel of Figure 5), were simulated by individual thermo-fluid-dynamic objects (TFO). The heat transfer between pin and sodium was treated by the heat-conduction objects (HCO). It should be

noted that simulation limitations arise from the restriction of the current rod model of ATHLET, where a HCO can be coupled to only one TFO. In FENNECS, a pin cell-resolved neutron kinetics model of both a single CEFR assembly and a minicore consisting of seven assemblies has been developed (see right panel of Figure 5). The pin cell-homogenized cross section libraries have been calculated by Serpent based on the models described above and are parameterized with respect to fuel temperature, sodium density, cladding temperature and pin lattice pitch to capture thermal hydraulic feedback. For the fuel temperature, six support points have been set between 518 K and 2100 K. For each of the remaining feedback parameters, three support points have been chosen, for the sodium density between 0.74 g/cm^3 and 0.927 g/cm^3, for the cladding temperature between 518 K and 1200 K, and for the pin lattice pitch between 6.124 cm and 6.1996 cm.

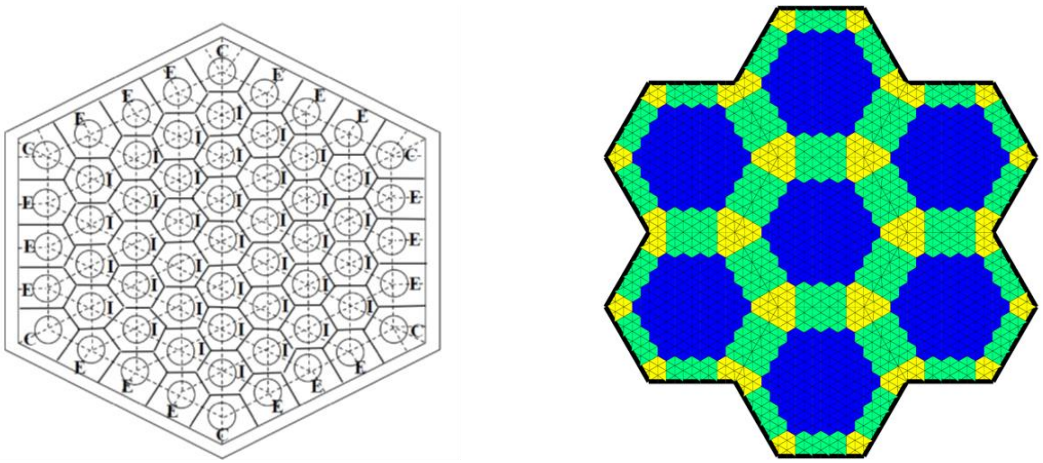

Figure 5: Left: Schematic description and ATHLET mesh setup of the CEFR fuel assembly with inner (I), edge (E) and corner (C) channels. **Right:** Material (cross section library) distribution in inner (blue), edge (green) and corner (yellow) pin cells of a minicore model in FENNECS.

Both for the single CEFR fuel assembly and the minicore, a 1-by-1 feedback mapping between FENNECS and ATHLET is applied, i.e. one pin cell of FENNECS is coupled to only one parallel subchannel in ATHLET. The left panel of Figure 6 shows the steady state fuel temperature distribution in the minicore axial midplane. The temporal evolutions of the minicore power as well as the average and maximum fuel temperature obtained by FENNECS/ATHLET for a transient initiated by a temporary 200 K inlet temperature decrease is shown in the right panel of Figure 6. Although the applicability of ATHLET is questionable for such modeling requirements, the results appear physically plausible and demonstrate the basic applicability of FENNECS to coupled SFR multiphysics simulations including transients. In the future, ATHLET is expected to be replaced by the subchannel code CTF to simulate sodium flow and heat transfer.

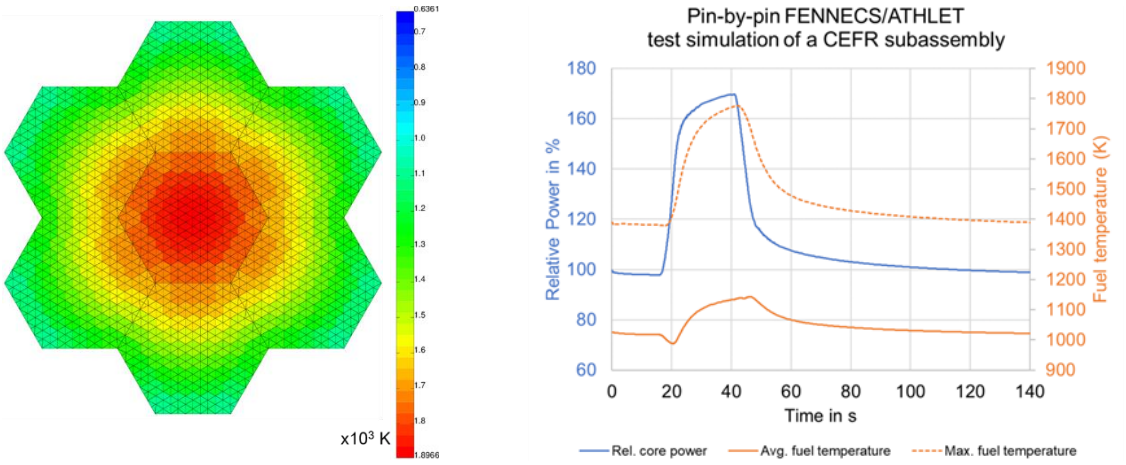

Figure 6: Left: Steady state fuel temperature distribution at the core midplane of the CEFR minicore obtained by FENNECS/ATHLET. **Right:** FENNECS/ATHLET simulation of a transient in a CEFR fuel assembly.

SUMMARY AND CONCLUSION

In this paper, CEFR start-up tests were simulated with the deterministic neutron kinetics code FENNECS in the frame of an IAEA coordinated research project. The criticality, control rod worth, as well as sodium void and subassembly swap reactivities were simulated with FENECCS. Satisfactory agreements were obtained between FENNECS and measurements as well as with Serpent Monte Carlo simulations, thus contributing to the validation of FENNECS. Finally, coupled pin-by-pin steady state and transient simulations were performed for a CEFR single fuel assembly as well as for a minicore using FENNECS/ATHLET. The obtained results demonstrate the basic applicability of FENNECS to coupled SFR multiphysics simulations including transients.

ACKNOWLEDGEMENT

This work has been supported by the German Federal Ministry of Economic Affairs and Energy. The data and information presented in this paper are part of the IAEA coordinated research project on "Neutronics Benchmark of CEFR Start-Up Tests – CRP-I31032".

REFERENCES

[1] X. Huo, Technical Specifications for Neutronics Benchmark of CEFR Start-up Tests, Presentation at the 2nd RCM of the IAEA CRP I31032 on Neutronics Benchmark of CEFR Start-up Tests, October 2019, Beijing, China (2019).
[2] A. Seubert, A 3-d Finite Element Few-group Diffusion Code and its Application to Generation IV Reactor Concepts, PHYSOR 2020: Transition to a Scalable Nuclear Future, Cambridge, United Kingdom, March 29 – April 2 (2020).
[3] A. Seubert, J. Bousquet, R. Henry, Recent Advances of the FENNECS Neutronics Code for Safety Assessment of (v)SMRs, Generation IV and Other Innovative Concepts, Proceedings of ANS M&C 2021, Raleigh, North Carolina, April 11–15 (2021).
[4] J. Bousquet, A. Seubert, R. Henry, New Finite Element Neutron Kinetics Coupled Code System FENNECS/ATHLET for Safety Assessment of (very) Small and Micro Reactors, Journal of Physics: Conference Series, 1689, pp. 012008 (2020).
[5] A. Wielenberg, L. Lovasz, P. Pandazis, A. Papukchiev, L. Tiborcz, P. Schöffel, C. Spengler, M. Sonnenkalb, A. Schaffrath, Recent Improvements in the System Code Package AC^2 2019 for the Safety Analysis of Nuclear Reactors, Nuclear Engineering and Design, 354, pp. 110211 (2019).
[6] A. Seubert, Parameterized Input Decks in Serpent using Variables and Arithmetic Expressions, 10th International Serpent User Group Meeting, Garching, Germany, October 27-30 (2020).
[7] E. Fridman, J. Leppänen, On the use of the Serpent Monte Carlo code for few-group cross section generation, Ann. Nucl. Energy, 38 (6), pp. 1399-1405 (2011).
[8] A. Seubert, Y. Périn, R. Henry, High-fidelity multi-physics pin-by-pin model of a SVEA-96 Optima2 assembly with TORT-TD/CTF, PHYSOR 2020: Transition to a Scalable Nuclear Future, Cambridge, United Kingdom, March 29th-April 2nd, 2020.
[9] Y. Périn, A. Seubert, High-Fidelity Multi-physics Critical Heat Flux Assessment and Stability Simulations of a SVEA-96 Optima2 BWR assembly with TORT-TD/CTF, 19th International Topical Meeting on Nuclear Reactor Thermal Hydraulics (NURETH-19), Brussels, Belgium, March 6 - 11, 2022.
[10] D. Ferraro et al., Serpent/SUBCHANFLOW pin-by-pin coupled transient calculations for the SPERT-IIIE hot full power tests, Annals of Nuclear Energy 142 (2020) 107387.
[11] A. Aly et al., Extending CTF modeling capabilites to SFRs and validation against SHRT tests, PHYSOR 2020: Transition to a Scalable Nuclear Future, Cambridge, United Kingdom, March 29th-April 2nd, 2020.
[12] A. Wielenberg et al., Recent improvements in the system code package AC2 2019 for the safety analysis of nuclear reactors, Nuclear Engineering and Design 354, (2019) 110211.
[13] J. Bousquet in: A. Seubert et al., Further development of calculation methods for the safety assessment of innovative reactor concepts also including P&T perspectives, research project RS1547, final report, GRS-553, (2019).

Chapter 3

Mathematical models

In this chapter, following the steps of the first phase, described in Figure 1.2, the SP_3 equations in the Galerkin formalism, including the boundary conditions, will be obtained. The starting point will be the neutron transport equation, which will be derived in section 3.1. Then, the P_N approximation will be obtained in subsection 3.2.2, from which the SP_3 approximation will be gained in section 3.3. Here, the steady state SP_3 equations will be taken into the Galerkin form, in order to allow their implementation in the finite element code FENNECS. In the same section, the algorithms developed within the first step of the second phase, hence the ones necessary to solve the system of SP_3 equations in the Galerkin formalism, will be explained.

3.1 Derivation of the steady state neutron transport equation in 1D with discretized energy groups

3.1.1 The neutron transport equation in 3D

At time t, the number of neutrons at position $\vec{r}$, travelling in direction $\vec{\Omega}$, and having an energy equal to E is described by the particle distribution function $Q(\vec{r}, \vec{\Omega}, E, t)$. $Q(\vec{r}, \vec{\Omega}, E, t)d\vec{r}d\vec{\Omega}dE$ describes the total number of neutrons contained in the volume element $d\vec{r}$ at position $\vec{r}$ with energy in the range between E and $E+dE$, which move in the cone of directions $d\vec{\Omega}$ in direction $\vec{\Omega}$, depicted in Figure 3.1 [37]. An expression for $Q(\vec{r}, \vec{\Omega}, E, t)$ can be found, performing a balance on the differential cylindrical volume element. As depicted in Figure 3.2, this has a cross section area equal to dA, which surrounds the neutron direction of motion, and a length of dl [37]. The length of the

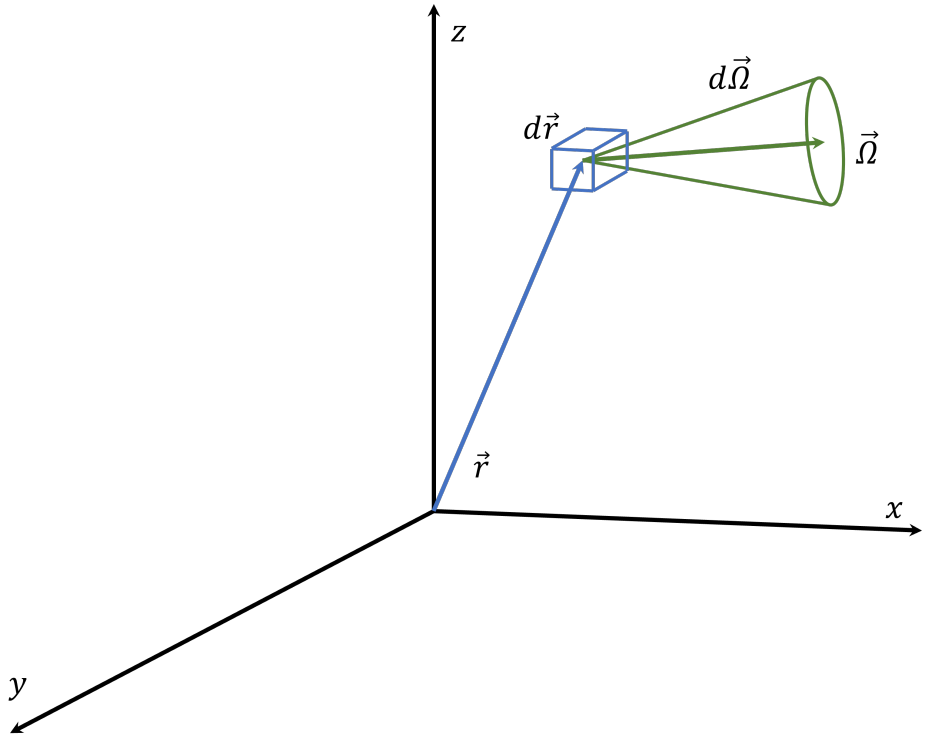

Figure 3.1: Differential volume element for particles in $d\vec{r}$ located in $\vec{r}$, which move in the cone $d\vec{\Omega}$ in direction $\vec{\Omega}$.

differential cylindrical volume element can be expressed as

$$dl = v(E)dt \tag{3.1}$$

where $v(E)$ is the energy-dependent neutron speed [37]. Firstly, the rate of change of the number of neutrons inside the control volume, hence $\frac{\partial}{\partial t}Q(\vec{r},\vec{\Omega},E,t)d\vec{r}d\vec{\Omega}dE$, depends on the rate of neutrons moving in the cone $d\vec{\Omega}$ in direction $\vec{\Omega}$ and energy between E and $E+dE$ that are entering and leaving the considered volume [57]. $v(E)Q(\vec{r},\vec{\Omega},E,t)$ is the rate of neutrons travelling in direction $\vec{\Omega}$, which enter the cylindrical control volume from the left side [57]. To this quantity, the rate of neutrons leaving the cylindrical control volume from the right cross section, hence at position $\vec{r}+\vec{\Omega}dl$, must be subtracted [37]. This rate is given by $v(E)Q(\vec{r}+\vec{\Omega}dl,\vec{\Omega},E,t)$ [37]. Secondly, for the evaluation of $\frac{\partial}{\partial t}Q(\vec{r},\vec{\Omega},E,t)d\vec{r}d\vec{\Omega}dE$, also sources of neutrons must be considered. The first source of neutrons is scattering of neutrons in $\vec{r}$, whose direction of travelling and energy will change from $\vec{\Omega}'$ to $\vec{\Omega}$ ($\vec{\Omega}' \rightarrow \vec{\Omega}$) and from E' to E ($E' \rightarrow E$), respectively, due to the event [57]. Quantities followed by an apostrophe address the neutrons before a scattering or fission event. The scattering contribution to the rate of change of neutrons in the control volume is expressed by $\int_0^\infty \left\{ \int_0^{4\pi} \left[\Sigma_s(\vec{r},\vec{\Omega}' \rightarrow \vec{\Omega}, E' \rightarrow E)v(E)Q(\vec{r},\vec{\Omega}',E',t)d\vec{r}d\vec{\Omega}dE \right] d\vec{\Omega}' \right\} dE'$, where Σ_s is the

macroscopic scattering cross section. The integration over $\vec{\Omega}'$, from 0 to 4π, and E', between 0 and infinity, is necessary to consider all the neutrons that after the scattering event travel in direction $\vec{\Omega}$ with energy E, independently from their original properties. The second source is related to neutrons in $\vec{r}$ with energy between E' and $E' + dE'$ that cause fission events [57]. This fission event produces neutrons, which travel in direction $\vec{\Omega}$ with energy between E and $E + dE$ [57]. This source is described by $\frac{\chi(\vec{r},E)}{4\pi}\int_0^\infty \left\{\int_0^{4\pi}\left[\bar{\nu}(\vec{r},E')\Sigma_f(\vec{r},E)v(E')Q(\vec{r},\vec{\Omega}',E',t)d\vec{r}d\vec{\Omega}dE\right]d\vec{\Omega}'\right\}dE'$, where $\chi(\vec{r},E)$, $\bar{\nu}(\vec{r},E')$, and Σ_f are the fission spectrum, the average number of neutrons emitted per fission reaction, and the macroscopic fission cross section, respectively. The last source of neutrons is represented by an external source of neutrons, which emits neutrons in $\vec{r}$ that move in direction $\vec{\Omega}$ with energy between E and $E + dE$ [57]. The rate of neutrons emitted by the external source is described by $S_{ex}(\vec{r},\vec{\Omega},E)d\vec{r}d\vec{\Omega}dE$. Thirdly, sinks of neutrons inside the control volume must be evaluated. Losses are caused by absorption and scattering of neutrons. The rate at which neutrons are lost is $[\Sigma_a(\vec{r},E) + \Sigma_s(\vec{r},E)]\, v(E)Q(\vec{r},\vec{\Omega},E,t)d\vec{r}d\vec{\Omega}dE$, where Σ_a is the macroscopic absorption cross section [57]. Summarizing all these considerations, the balance can be expressed by the following equation:

$$\begin{aligned}\frac{\partial}{\partial t}Q(\vec{r},\vec{\Omega},E,t)d\vec{r}d\vec{\Omega}dE = v(E)\left[Q(\vec{r},\vec{\Omega},E,t) - Q(\vec{r}+\vec{\Omega}dl,\vec{\Omega},E,t)\right]dAd\vec{\Omega}dE+\\ +\int_0^\infty\left\{\int_0^{4\pi}\left[\Sigma_s(\vec{r},\vec{\Omega}'\to\vec{\Omega},E'\to E)v(E)Q(\vec{r},\vec{\Omega}',E',t)d\vec{r}d\vec{\Omega}dE\right]d\vec{\Omega}'\right\}dE'+\\ +\frac{\chi(\vec{r},E)}{4\pi}\int_0^\infty\left\{\int_0^{4\pi}\left[\bar{\nu}(\vec{r},E')\Sigma_f(\vec{r},E)v(E')Q(\vec{r},\vec{\Omega}',E',t)d\vec{r}d\vec{\Omega}dE\right]d\vec{\Omega}'\right\}dE'+\\ +S_{ex}(\vec{r},\vec{\Omega},E)d\vec{r}d\vec{\Omega}dE - \left[\Sigma_a(\vec{r},E)+\Sigma_s(\vec{r},E)\right]v(E)Q(\vec{r},\vec{\Omega},E,t)d\vec{r}d\vec{\Omega}dE.\end{aligned} \tag{3.2}$$

The cylindrical volume element $d\vec{r}$, depicted in Figure 3.2, can be written in terms of the differential cross section area and length of the differential volume, hence in the following manner:

$$d\vec{r} = dAdl \Rightarrow dA = \frac{d\vec{r}}{dl} \tag{3.3}$$

[37]. Applying Equation 3.3, the streaming term, present in Equation 3.2, can be rewritten as

$$\begin{aligned}v(E)\left[Q(\vec{r},\vec{\Omega},E,t) - Q(\vec{r}+\vec{\Omega}dl,\vec{\Omega},E,t)\right]dAd\vec{\Omega}dE = v(E)\Big[Q(\vec{r},\vec{\Omega},E,t)+\\ -Q(\vec{r}+\vec{\Omega}dl,\vec{\Omega},E,t)\Big]\frac{d\vec{r}}{dl}d\vec{\Omega}dE.\end{aligned} \tag{3.4}$$

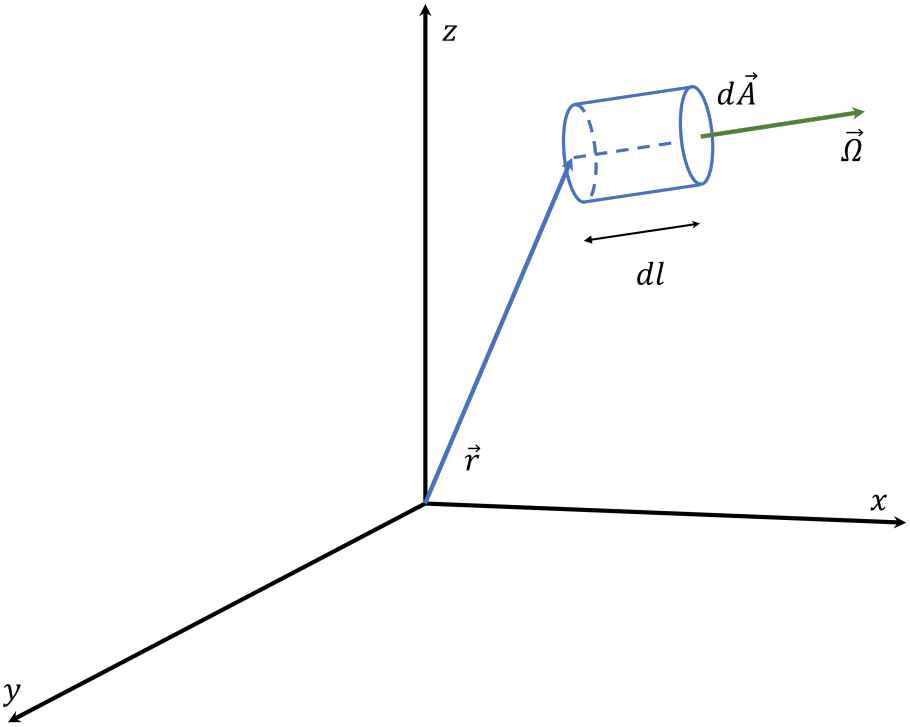

Figure 3.2: Cylindrical differential volume element for neutrons located in $\vec{r}$, which move in direction $\vec{\Omega}$.

Dividing Equation 3.2 by dE and $d\vec{r}$ and inserting Equation 3.4, leads to the following formulation of the balance equation:

$$\begin{aligned}\frac{\partial}{\partial t}Q(\vec{r},\vec{\Omega},E,t)d\vec{\Omega} = v(E)\left[Q(\vec{r},\vec{\Omega},E,t) - Q(\vec{r}+\vec{\Omega}dl,\vec{\Omega},E,t)\right]\frac{d\vec{\Omega}}{dl}+\\ +\int_0^\infty\left\{\int_0^{4\pi}\left[\Sigma_s(\vec{r},\vec{\Omega}'\to\vec{\Omega},E'\to E)v(E)Q(\vec{r},\vec{\Omega}',E',t)d\vec{\Omega}\right]d\vec{\Omega}'\right\}dE'+\\ +\frac{\chi(\vec{r},E)}{4\pi}\int_0^\infty\left\{\int_0^{4\pi}\left[\bar{\nu}(\vec{r},E')\Sigma_f(\vec{r},E)v(E')Q(\vec{r},\vec{\Omega}',E',t)d\vec{\Omega}\right]d\vec{\Omega}'\right\}dE'+\\ +S_{ex}(\vec{r},\vec{\Omega},E)d\vec{\Omega} - \left[\Sigma_a(\vec{r},E)+\Sigma_s(\vec{r},E)\right]v(E)Q(\vec{r},\vec{\Omega},E,t)d\vec{\Omega}.\end{aligned} \tag{3.5}$$

The new formulation of the streaming term in Equation 3.5 can be rewritten in the following way, by swapping the order of the in and out streaming terms:

$$\begin{aligned}v(E)\left[Q(\vec{r},\vec{\Omega},E,t) - Q(\vec{r}+\vec{\Omega}dl,\vec{\Omega},E,t)\right]\frac{d\vec{\Omega}}{dl} = -v(E)\Big[Q(\vec{r}+\vec{\Omega}dl,\vec{\Omega},E,t)+\\ -Q(\vec{r},\vec{\Omega},E,t)\Big]\frac{d\vec{\Omega}}{dl}.\end{aligned} \tag{3.6}$$

Equation 3.6 can be further manipulated recalling the definition of derivative. The

derivative of any function $w(x)$ at a fixed point x_0 is defined as

$$\frac{dw(x_0)}{dx} = \lim_{x \to x_0} \frac{w(x) - w(x_0)}{x - x_0} = \lim_{\Delta x \to 0} \frac{w(x_0 + \Delta x) - w(x_0)}{\Delta x} \tag{3.7}$$

where $\Delta x = x - x_0$ [12]. The definition given by Equation 3.7 can be applied to Equation 3.6, leading to the following reformulation of the streaming term:

$$-v(E)\Big[Q(\vec{r} + \vec{\Omega}dl, \vec{\Omega}, E, t) - Q(\vec{r}, \vec{\Omega}, E, t)\Big]\frac{d\vec{\Omega}}{dl} = -v(E)\frac{dQ(\vec{r}, \vec{\Omega}, E, t)}{dl}d\vec{\Omega} \tag{3.8}$$

[37].

Here, the term $\frac{d}{dl}$ can be rewritten in terms of Cartesian coordinates as

$$\frac{d}{dl} = \frac{\partial}{\partial x}\frac{dx}{dl} + \frac{\partial}{\partial y}\frac{dy}{dl} + \frac{\partial}{\partial z}\frac{dz}{dl} \tag{3.9}$$

where

$$\frac{dx}{dl} = \vec{\Omega} \cdot \vec{\epsilon_x} \tag{3.10}$$

$$\frac{dy}{dl} = \vec{\Omega} \cdot \vec{\epsilon_y} \tag{3.11}$$

$$\frac{dz}{dl} = \vec{\Omega} \cdot \vec{\epsilon_z} \tag{3.12}$$

[37]. In Equation 3.10, 3.11, and 3.12 the vectors $\vec{\epsilon_x}$, $\vec{\epsilon_y}$, and $\vec{\epsilon_z}$ are the three basis vectors of the coordinate system. Inserting these three equations in Equation 3.9 leads to the following expression:

$$\frac{d}{dl} = \vec{\Omega} \cdot \vec{\epsilon_x}\frac{\partial}{\partial x} + \vec{\Omega} \cdot \vec{\epsilon_y}\frac{\partial}{\partial y} + \vec{\Omega} \cdot \vec{\epsilon_z}\frac{\partial}{\partial z} = \vec{\Omega} \cdot \vec{\nabla} \tag{3.13}$$

[37]. After inserting Equation 3.13 in Equation 3.8, the streaming term takes the following form:

$$-v(E)\frac{dQ(\vec{r}, \vec{\Omega}, E, t)}{dl}d\vec{\Omega} = -v(E)\vec{\Omega} \cdot \vec{\nabla}Q(\vec{r}, \vec{\Omega}, E, t)d\vec{\Omega}. \tag{3.14}$$

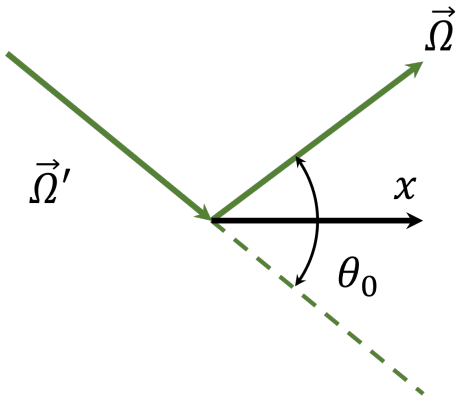

Figure 3.3: Scattering event of a particle travelling in direction $\vec{\Omega}'$. After the scattering process, its direction will be $\vec{\Omega}$. The angle between the two directions of motions is θ_0.

Including Equation 3.8 in Equation 3.5, the balance equation can be formulated as:

$$\begin{aligned}\frac{\partial}{\partial t}Q(\vec{r},\vec{\Omega},E,t)d\vec{\Omega} = -v(E)\vec{\Omega}\cdot\vec{\nabla}Q(\vec{r},\vec{\Omega},E,t)d\vec{\Omega}+\\ +\int_0^\infty\left\{\int_0^{4\pi}\left[\Sigma_s(\vec{r},\vec{\Omega}'\to\vec{\Omega},E'\to E)v(E)Q(\vec{r},\vec{\Omega}',E',t)d\vec{\Omega}\right]d\vec{\Omega}'\right\}dE'+\\ +\frac{\chi(\vec{r},E)}{4\pi}\int_0^\infty\left\{\int_0^{4\pi}\left[\bar{\nu}(\vec{r},E')\Sigma_f(\vec{r},E)v(E')Q(\vec{r},\vec{\Omega}',E',t)d\vec{\Omega}\right]d\vec{\Omega}'\right\}dE'+\\ +S_{ex}(\vec{r},\vec{\Omega},E)d\vec{\Omega}-\left[\Sigma_a(\vec{r},E)+\Sigma_s(\vec{r},E)\right]v(E)Q(\vec{r},\vec{\Omega},E,t)d\vec{\Omega}.\end{aligned} \tag{3.15}$$

In Equation 3.15, the neutron distribution is always multiplied by the neutron velocity. Therefore, at this stage, it results convenient to introduce the directional or angular flux distribution, which is defined as:

$$\psi(\vec{r},\vec{\Omega},E,t) = v(E)Q(\vec{r},\vec{\Omega},E,t) \tag{3.16}$$

[37, 57]. By replacing the definition of directional flux and by dividing Equation 3.15 by $d\vec{\Omega}$, the following more compact formulation is achieved:

$$\begin{aligned}\frac{1}{v(E)}\frac{\partial}{\partial t}\psi(\vec{r},\vec{\Omega},E,t)+\vec{\Omega}\cdot\vec{\nabla}\psi(\vec{r},\vec{\Omega},E,t)+\\ \left[\Sigma_a(\vec{r},E)+\Sigma_s(\vec{r},E)\right]\psi(\vec{r},\vec{\Omega},E,t) =\\ =\int_0^\infty\left\{\int_0^{4\pi}\left[\Sigma_s(\vec{r},\vec{\Omega}'\to\vec{\Omega},E'\to E)\psi(\vec{r},\vec{\Omega}',E',t)\right]d\vec{\Omega}'\right\}dE'+\\ +\frac{\chi(\vec{r},E)}{4\pi}\int_0^\infty\left\{\int_0^{4\pi}\left[\bar{\nu}(\vec{r},E')\Sigma_f(\vec{r},E)\psi(\vec{r},\vec{\Omega}',E',t)\right]d\vec{\Omega}'\right\}dE'+\\ +S_{ex}(\vec{r},\vec{\Omega},E).\end{aligned} \tag{3.17}$$

Before arriving at the final expression of the neutron transport equation, some considerations regarding the macroscopic scattering cross sections are necessary. Firstly, assuming isotropic scattering, a scattering event from $\vec{\Omega}'$ to $\vec{\Omega}$, like in Figure 3.3, depends only on $\vec{\Omega}' \cdot \vec{\Omega}$ [57]. Here, applying the definition of scalar product between the two vectors and considering that $\vec{\Omega}'$ as well as $\vec{\Omega}$ are unitary vectors, leads to the following expression

$$\begin{aligned} \vec{\Omega}' \cdot \vec{\Omega} &= \left[|\vec{\Omega}'| \cdot |\vec{\Omega}| \right] cos(\theta_0) \\ &= cos(\theta_0) \end{aligned} \tag{3.18}$$

where θ_0 is the angle between the two directions of motions [11, 56]. Now, the following notation can be introduced:

$$\mu_0 \equiv cos(\theta_0). \tag{3.19}$$

Equation 3.18, together with Equation 3.19, can be used to rewrite $\Sigma_s(\vec{r}, \vec{\Omega}' \rightarrow \vec{\Omega}, E' \rightarrow E)$ as

$$\begin{aligned} \Sigma_s(\vec{r}, \vec{\Omega}' \rightarrow \vec{\Omega}, E' \rightarrow E) &= \Sigma_s(\vec{r}, \vec{\Omega}' \cdot \vec{\Omega}, E' \rightarrow E) \\ &= \Sigma_s(\vec{r}, \mu_0, E' \rightarrow E). \end{aligned} \tag{3.20}$$

Secondly, based on the scattering and on the absorption macroscopic cross sections, the total macroscopic cross section can be introduced:

$$\Sigma_t(\vec{r}, \vec{\Omega}', E) = \Sigma_a(\vec{r}, \vec{\Omega}', E) + \int_0^{4\pi} \Sigma_s(\vec{r}, \vec{\Omega}' \rightarrow \vec{\Omega}, E) d\vec{\Omega}. \tag{3.21}$$

Both sides of the equation can be integrated by $d\vec{\Omega}'$ as follows:

$$\begin{aligned} \int_0^{4\pi} \Sigma_t(\vec{r}, \vec{\Omega}', E) d\vec{\Omega}' = \int_0^{4\pi} \Sigma_a(\vec{r}, \vec{\Omega}', E) d\vec{\Omega}' + \\ + \int_0^{4\pi} \left[\int_0^{4\pi} \Sigma_s(\vec{r}, \vec{\Omega}' \rightarrow \vec{\Omega}, E) d\vec{\Omega}. \right] d\vec{\Omega}' \end{aligned} \tag{3.22}$$

Computing the integrals leads to the following definition of the total macroscopic cross section:

$$\Sigma_t(\vec{r}, E) = \Sigma_a(\vec{r}, E) + \Sigma_s(\vec{r}, E) \tag{3.23}$$

[57]. The expressions for the scattering and total cross sections, given in Equation 3.20, and 3.23, respectively, can be inserted in Equation 3.17, leading to the transport

equation, formulated as follows:

$$\begin{aligned}\frac{1}{v(E)}\frac{\partial}{\partial t}\psi(\vec{r},\vec{\Omega},E,t)+\vec{\Omega}\cdot\vec{\nabla}\psi(\vec{r},\vec{\Omega},E,t)+\Sigma_t(\vec{r},E)\psi(\vec{r},\vec{\Omega},E,t)=\\ =\int_0^\infty\left\{\int_0^{4\pi}\left[\Sigma_s(\vec{r},\mu_0,E'\rightarrow E)\psi(\vec{r},\vec{\Omega}',E',t)\right]d\vec{\Omega}'\right\}dE'+\\ +\frac{\chi(\vec{r},E)}{4\pi}\int_0^\infty\left\{\int_0^{4\pi}\left[\bar{\nu}(\vec{r},E')\Sigma_f(\vec{r},E)\psi(\vec{r},\vec{\Omega}',E',t)\right]d\vec{\Omega}'\right\}dE'+\\ +S_{ex}(\vec{r},\vec{\Omega},E).\end{aligned} \tag{3.24}$$

The last two lines of the equation represent both neutron sources. These are the fission and external source. These two terms can be summarised by the source term $S(\vec{r},\vec{\Omega},E,t)$ that is defined as

$$\begin{aligned}S(\vec{r},\vec{\Omega},E,t)=\frac{\chi(\vec{r},E)}{4\pi}\int_0^\infty\left\{\int_0^{4\pi}\left[\bar{\nu}(\vec{r},E')\Sigma_f(\vec{r},E)\psi(\vec{r},\vec{\Omega}',E',t)\right]d\vec{\Omega}'\right\}dE'+\\ +S_{ex}(\vec{r},\vec{\Omega},E).\end{aligned} \tag{3.25}$$

3.1.2 The neutron transport equation for a slab

Before arriving at the neutron transport equation for a slab, some considerations are necessary. Firstly, as it can be seen from Figure 3.4, the direction vector $\vec{\Omega}$ can be described through the angles ω and θ, where

$$\mu \equiv cos(\theta) \tag{3.26}$$

[11]. This definition can be used to develop the expression present in the second term of Equation 3.24 as

$$\vec{\Omega}\cdot\vec{\nabla}=\mu\frac{\partial}{\partial x}+sin(\theta)cos(\omega)\frac{\partial}{\partial y}+sin(\theta)sin(\omega)\frac{\partial}{\partial z} \tag{3.27}$$

[11]. Secondly, for $\vec{\Omega}$, the following relationship can be established:

$$\int_0^{4\pi}d\vec{\Omega}=\frac{1}{4\pi}\int_0^{2\pi}d\omega\int_{-1}^{1}d\mu \Rrightarrow d\vec{\Omega}=\frac{d\omega d\mu}{4\pi} \tag{3.28}$$

where the factor $\frac{1}{4\pi}$ is due to normalization [37]. Thirdly, in Equation 3.24, the dependency on $\vec{r}$ is substituted by the one on x. The dependency of the angular flux on $\vec{r}$ as well as on $\vec{\Omega}$ is replaced by x and μ, respectively. Therefore, no dependency on ω is introduced, since a planar geometry is considered. Including these considerations

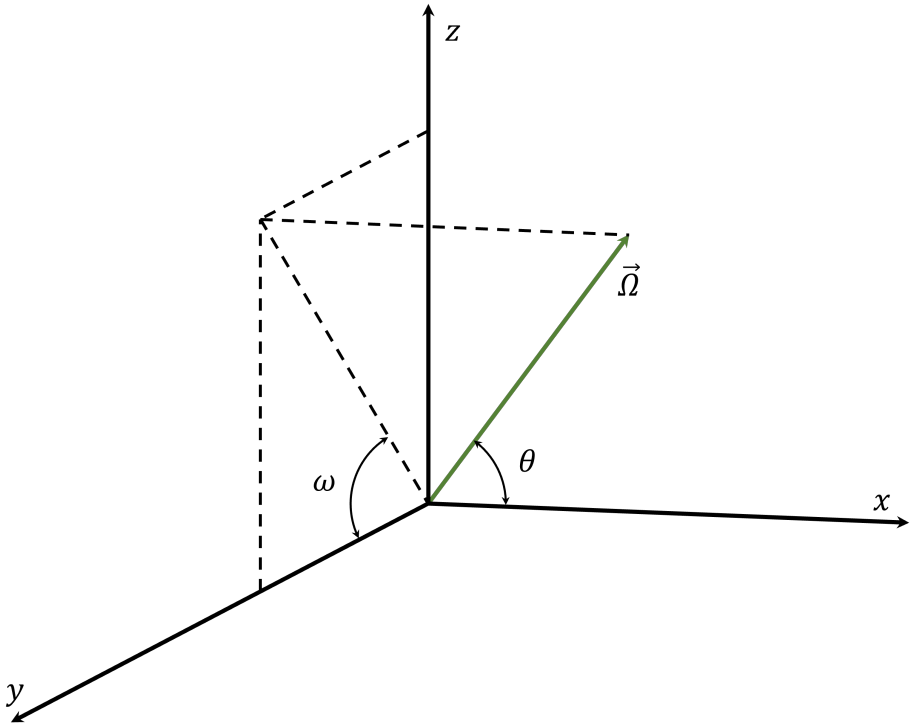

Figure 3.4: Coordinate system used for the derivation.

in Equation 3.24 leads to the following form of the transport equation for planar geometries:

$$\begin{aligned}\frac{1}{v(E)}\frac{\partial}{\partial t}\psi(x,\mu,E,t)+\mu\frac{\partial}{\partial x}\psi(x,\mu,E,t)+\Sigma_t(x,E)\psi(x,\mu,E,t)=\\ =\frac{1}{4\pi}\int_0^\infty\left\{\int_{-1}^1\left[\int_0^{2\pi}\Sigma_s(x,\mu_0,E'\to E)\psi(x,\mu',E',t)d\omega'\right]d\mu'\right\}dE'+\\ +S(x,\mu,E,t)\end{aligned} \tag{3.29}$$

where

$$\begin{aligned}S(x,\mu,E,t)=\frac{\chi(x,E)}{4\pi}\int_0^\infty\left\{\int_{-1}^1\left[\int_0^{2\pi}\bar{\nu}(x,E')\Sigma_f(x,E')\cdot\right.\right.\\ \left.\left.\cdot\psi(x,\mu',E',t)d\omega'\right]d\mu'\right\}dE'+S_{ex}(x,\mu,E).\end{aligned} \tag{3.30}$$

Here, the fission term has no dependency on the angle ω'. Furthermore, μ' affects only the directional flux. Therefore, the integrals can be computed. Integrating the angular flux over ω' and μ', the angular dependency is lost and the scalar flux $\phi_0(x,E',t)$ is

obtained. Therefore, Equation 3.30 can be written as:

$$S(x,\mu,E,t) = \chi(x,E)\int_0^\infty \left[\bar{\nu}(x,E')\Sigma_f(x,E')\phi_0(x,E',t)\right] dE' + S_{ex}(x,\mu,E). \quad (3.31)$$

3.1.3 Energy discretization

Since in FENNECS input cross sections have a discrete spectrum, at this point, it is convenient to introduce the energy discretization in the derivation. The energy spectrum is divided in G groups, where $g \in (1,...G)$ [19]. Here, $g = 1$ corresponds to the fastest energy group [19]. Therefore, the energy dependence will be replaced by an index g, or g', and the integrals by summations from 1 to G, hence from the fastest to the slowest energy group. Consequently, considering energy group g, Equation 3.29 and 3.31 can be written as:

$$\begin{aligned} &\frac{1}{v_g}\frac{\partial}{\partial t}\psi_g(x,\mu,t) + \mu\frac{\partial}{\partial x}\psi_g(x,\mu,t) + \Sigma_{t,g}(x)\psi_g(x,\mu,t) = \\ &= \frac{1}{4\pi}\sum_{g'=1}^{G}\left\{\int_{-1}^{1}\left[\int_0^{2\pi}\Sigma_{s,g'g}(x,\mu_0)\psi_{g'}(x,\mu',t)d\omega'\right]d\mu'\right\} + S_g(x,\mu,t) \end{aligned} \quad (3.32)$$

$$S_g(x,\mu,t) = \chi_g(x)\sum_{g'=1}^{G}\left[\bar{\nu}_{g'}(x)\Sigma_{f,g'}(x)\phi_{0,g'}(x,t)\right] + S_{ex,g}(x,\mu). \quad (3.33)$$

3.1.4 The one dimensional steady state neutron transport equation with energy discretization

Considering steady state scenarios leads firstly to the loss of the time dependancy in all the terms present in Equation 3.32 and 3.33. Secondly, the derivative over the time becomes zero, such that the first term of Equation 3.32 vanishes. Thirdly, the external neutron source $S_{ex,g}(x,\mu)$ is set to zero, and the effective multiplication factor k_{eff} is introduced. Therefore, as in [11, 19, 37, 57], Equation 3.32 and 3.33 can be written as

$$\begin{aligned} &\mu\frac{\partial}{\partial x}\psi_g(x,\mu) + \Sigma_{t,g}(x)\psi_g(x,\mu) = \\ &= \frac{1}{4\pi}\sum_{g'=1}^{G}\left\{\int_{-1}^{1}\left[\int_0^{2\pi}\Sigma_{s,g'g}(x,\mu_0)\psi_{g'}(x,\mu')d\omega'\right]d\mu'\right\} + S_g(x,\mu) \end{aligned} \quad (3.34)$$

$$S_g(x,\mu) = \frac{\chi_g(x)}{k_{eff}} \sum_{g'=1}^{G} \left[\bar{\nu}_{g'}(x)\Sigma_{f,g'}(x)\phi_{g'}(x)\right]. \tag{3.35}$$

3.2 The steady state P_N-approximation of the transport equation

As already mentioned, the SP_3 approximation is derived from the P_N approximation. Here, the angular dependencies of the transport equation are modelled with spherical harmonics expansions in multi-dimensions and with Legendre polynomials in case of one dimension [24, 26, 65]. Therefore, to derive the P_N approximation of Equation 3.34 and 3.35, which are for planar geometries, the Legendre polynomials will be used.

3.2.1 Theorems of the Legendre polynomials

Before starting to insert the Legendre polynomials in the derived transport equation, some considerations about them are necessary. Firstly, the property of the Legendre polynomials that will be mostly used hereafter is the orthogonality relation, which is

$$\int_{-1}^{1} P_n(\mu)P_m(\mu)d\mu = \frac{2}{2n+1}\delta_{nm} \tag{3.36}$$

where $P_n(x)$ and $P_m(x)$ are Legendre polynomials of order n and m, respectively, with $n, m \in \mathbb{N}$, which is the set of the natural numbers [57]. δ_{nm} is the Kroneker delta, defined as

$$\delta_{nm} = \begin{cases} 1, & \text{for} \quad n = m \\ 0, & \text{for} \quad n \neq m \end{cases} \tag{3.37}$$

[45].

Secondly, the recursion rule will be useful, which is defined as:

$$\mu P_n(\mu) = \frac{n}{2n+1}P_{n-1}(\mu) + \frac{n+1}{2n+1}P_{n+1}(\mu) \tag{3.38}$$

[37, 57].

Thirdly, another useful property is the addition theorem, which reads as follows

$$P_n(\mu_0) = \sum_{h=-n}^{n} \frac{(n-h)!}{(n+h)!} P_n^h(\mu) P_n^h(\mu') e^{ih(\omega-\omega')} \tag{3.39}$$

where h indicates an exponent [57].

Finally, any function $w(\mu)$, continuous in $\mu \in [-1, 1]$, can be expressed in this interval in terms of Legendre polynomials as

$$w(\mu) = \sum_{m=0}^{\infty} w_m P_m(\mu) \tag{3.40}$$

where w_m must be found [11, 37, 32]. By multiplying both sides of the equation by $P_n(\mu)$ and by integrating μ from -1 to 1 leads to

$$\int_{-1}^{1} w(\mu) P_n(\mu) d\mu = \sum_{n=0}^{\infty} w_m \int_{-1}^{1} P_n(\mu) P_m(\mu) d\mu \tag{3.41}$$

[32]. For the integral on the right hand side, the orthogonality theorem can be applied [32]. Therefore, inserting Equation 3.36 in 3.44 leads to

$$\int_{-1}^{1} w(\mu) P_m(\mu) d\mu = \frac{2}{2m+1} w_m \tag{3.42}$$

[32]. From Equation 3.42, a definition of w_m can be found, which is

$$w_m = \frac{2}{2m+1} \int_{-1}^{1} w(\mu) P_m(\mu) d\mu \tag{3.43}$$

[32]. Inserting the definition of w_m in Equation 3.40 leads to

$$w(\mu) = \sum_{m=0}^{\infty} \frac{2}{2m+1} P_m(\mu) \int_{-1}^{1} w(\mu) P_m(\mu) d\mu = \sum_{m=0}^{\infty} (2m+1) P_m(\mu) w_m \tag{3.44}$$

where

$$w_m = \frac{1}{2} \int_{-1}^{1} w(\mu) P_m(\mu) d\mu \tag{3.45}$$

[32].

3.2.2 Mathematical derivation of the P_N method

The P_N method consists in approximating the angular dependency present in the transport equation with the first $N+1$ Legendre polynomials. Therefore, firstly, the variables, which were showing an angular dependency in Equation 3.34 must be identified. These are the angular flux $\psi_g(x,\mu)$, $\Sigma_{s,g'g}(x,\mu_0)$, and $S_g(x,\mu)$. In order to derive the Legendre expansion of these three quantities, Equation 3.44 and 3.45 can be applied. However, in order to derive the P_N equations, the angular dependency is approximated using only the first $N+1$ Legendre polynomials. Therefore, in Equation 3.44 and 3.45, the summations up to infinity will be replaced by summations up to N. Consequently, the Legendre expansion of the angular flux takes the following form:

$$\psi_g(x,\mu) \approx \sum_{m=0}^{N}(2n+1)P_n(\mu)\phi_{n,g}(x) \tag{3.46}$$

where

$$\phi_{n,g}(x) = \frac{1}{2}\int_{-1}^{1}\psi_g(x,\mu)P_n(\mu)d\mu \tag{3.47}$$

[11, 37, 57]. $\phi_{n,g}(x)$ represents the n-th order neutron flux. Similarly, also the scattering cross section can be expanded as

$$\Sigma_{s,g'g}(x,\mu_0) \approx \sum_{m=0}^{N}(2n+1)P_n(\mu)\Sigma_{s,n,g'g}(x) \tag{3.48}$$

where

$$\Sigma_{s,n,g'g}(x) = \frac{1}{2}\int_{-1}^{1}\Sigma_{s,g'g}(x,\mu_0)P_n(\mu_0)d\mu_0 \tag{3.49}$$

[11, 37, 57]. In Equation 3.48 and 3.49, $\Sigma_{s,n,g'g}(x)$ is the n-th order macroscopic cross section for the scattering from g to g'. The same procedure can be repeated also for the source term:

$$S_g(x,\mu) \approx \sum_{m=0}^{N+1}(2n+1)P_n(\mu)S_{n,g}(x) \tag{3.50}$$

where

$$S_{n,g}(x) = \frac{1}{2}\int_{-1}^{1}S_g(x,\mu)P_n(\mu)d\mu \tag{3.51}$$

[11, 37, 57]. $S_{n,g}(x)$ is the n-th order source distribution.

Now, Equation 3.46, 3.48, and 3.50 can be inserted step by step in the transport equation, hence in Equation 3.34. At the beginning, only the scattering term of Equation 3.34 is considered. Firstly, the scattering cross section is expanded, hence Equation 3.48 is inserted as follows:

$$\begin{aligned} &\frac{1}{4\pi}\sum_{g'=1}^{G}\left\{\int_{-1}^{1}\left[\int_{0}^{4\pi}\Sigma_{s,g'g}(x,\mu_0)\psi_{g'}(x,\mu')d\omega'\right]d\mu'\right\}\approx \\ \approx &\frac{1}{4\pi}\int_{-1}^{1}\left\{\int_{0}^{2\pi}\sum_{n=0}^{N}\left[(2n+1)P_n(\mu_0)\sum_{g'=1}^{G}\Sigma_{s,n,g'g}(x)\psi_{g'}(x,\mu')\right]d\omega'\right\}d\mu'. \end{aligned} \tag{3.52}$$

Successively, the addition theorem of Equation 3.39 can be applied leading to

$$\begin{aligned} &\frac{1}{4\pi}\int_{-1}^{1}\left\{\int_{0}^{2\pi}\sum_{n=0}^{N+1}\left[(2n+1)P_n(\mu_0)\sum_{g'=1}^{G}\Sigma_{s,n,g'g}(x)\psi_{g'}(x,\mu')\right]d\omega'\right\}d\mu' = \\ &= \frac{1}{4\pi}\int_{-1}^{1}\left\{\sum_{n=0}^{N}\left[(2n+1)\sum_{g'=1}^{G}\left(\psi_{g'}(x,\mu')\cdot\right.\right.\right. \\ &\left.\left.\left.\cdot\sum_{h=-n}^{n}P_n^h(\mu)P_n^h(\mu')e^{im(\omega-\omega')}\Sigma_{s,n,g'g}(x)\right)\right]d\omega'\right\}d\mu' = \\ &= \frac{1}{4\pi}\sum_{n=0}^{N}\left\{(2n+1)\sum_{h=-n}^{n}\left[P_n^h(\mu)\int_{0}^{2\pi}e^{im(\omega-\omega')}d\omega'\cdot\right.\right. \\ &\left.\left.\cdot\int_{-1}^{1}\sum_{g'=1}^{G}\psi_{g'}(x,\mu')\Sigma_{s,n,g'g}(x)P_n^h(\mu')d\mu'\right]\right\}. \end{aligned} \tag{3.53}$$

[57]. The obtained expression can be further manipulated by applying the product rule of the exponents, defined in the following way:

$$e^x e^y = e^{x+y} \tag{3.54}$$

[33]. Therefore, with the help of Equation 3.54, Equation 3.53 can be written as:

$$\begin{aligned}
&\frac{1}{4\pi}\sum_{n=0}^{N}\left\{(2n+1)\sum_{h=-n}^{n}\left[P_n^h(\mu)\int_0^{2\pi}e^{ih(\omega-\omega')}d\omega'\cdot\right.\right.\\
&\left.\left.\cdot\int_{-1}^{1}\sum_{g'=1}^{G}\psi_{g'}(x,\mu')\Sigma_{s,n,g'g}(x)P_n^h(\mu')d\mu'\right]\right\}=\\
&=\frac{1}{4\pi}\sum_{n=0}^{N}\left\{(2n+1)\sum_{h=-n}^{n}\left[P_n^h(\mu)\int_0^{2\pi}e^{ih\omega}e^{-ih\omega'}d\omega'\cdot\right.\right.\\
&\left.\left.\cdot\sum_{g'=1}^{G}\left(\Sigma_{s,n,g'g}(x)\int_{-1}^{1}\psi_{g'}(x,\mu')P_n^h(\mu')d\mu'\right)\right]\right\}=\\
&=\frac{1}{4\pi}\sum_{n=0}^{N}\left\{(2n+1)\sum_{h=-n}^{n}\left[P_n^h(\mu)e^{ih\omega}\int_0^{2\pi}e^{-ih\omega'}d\omega'\right.\right.\\
&\left.\left.\cdot\sum_{g'=1}^{G}\left(\Sigma_{s,n,g'g}(x)\int_{-1}^{1}\psi_{g'}(x,\mu')P_n^h(\mu')d\mu'\right)\right]\right\}.
\end{aligned}\tag{3.55}$$

Depending on the value of h, it can be distinguished between two cases: for h different from zero and for h equal to zero. For the first case, hence h different from zero, the evaluation of the first integral in Equation 3.55 leads to

$$\begin{aligned}
&\frac{1}{4\pi}\sum_{n=0}^{N}\left\{(2n+1)\sum_{h=-n,h=-n}^{n}\left[P_n^h(\mu)e^{ih\omega}\int_0^{2\pi}e^{-ih\omega'}d\omega'\cdot\right.\right.\\
&\left.\left.\cdot\sum_{g'=1}^{G}\left(\Sigma_{s,n,g'g}(x)\int_{-1}^{1}\psi_{g'}(x,\mu')P_n^h(\mu')d\mu'\right)\right]\right\}=\\
&=\frac{1}{4\pi}\sum_{n=0}^{N}\left\{(2n+1)\sum_{h=-n,h\neq 0}^{n}\left[P_n^h(\mu)e^{im\omega}\left[e^{-ih\omega'}\right]_{\omega'=0}^{\omega'=2\pi}\cdot\right.\right.\\
&\left.\left.\cdot\sum_{g'=1}^{G}\left(\Sigma_{s,n,g'g}(x)\int_{-1}^{1}\psi_{g'}(x,\mu')P_n^h(\mu')d\mu'\left(-\frac{1}{ih}\right)\right)\right]\right\}.
\end{aligned}\tag{3.56}$$

In order to evaluate the last term, the Euler's formula can be applied, which is defined as:

$$e^{ix}=cos(x)+isin(x)\tag{3.57}$$

[49]. Therefore, inserting Equation 3.57 in the expression obtained for Equation 3.56

leads to the following formulation:

$$\begin{aligned}\frac{1}{4\pi}\sum_{n=0}^{N}\Bigg\{(2n+1)\sum_{h=-n,m\neq 0}^{n}\Bigg[-\frac{1}{ih}P_n^h(\mu)e^{im\omega}\left[cos(h\omega')-isin(h\omega')\right]_{\omega'=0}^{\omega'=2\pi}\cdot \\ \cdot\left(\sum_{g'=1}^{G}\Sigma_{s,n,g'g}(x)\int_{-1}^{1}\psi_{g'}(x,\mu')P_n^m(\mu')d\mu'\right)\Bigg]\Bigg\}= \\ =\frac{1}{4\pi}\sum_{n=0}^{N}\Bigg\{(2n+1)\sum_{h=-n,m\neq 0}^{n}\Bigg[-\frac{1}{ih}P_n^m(\mu)e^{im\omega}\left(cos(2\pi h)-isin(2\pi h)+\right. \\ \left.-cos(0\cdot h)+isin(0\cdot h)\right)\left(\sum_{g'=1}^{G}\Sigma_{s,n,g'g}(x)\int_{-1}^{1}\psi_{g'}(x,\mu')P_n^h(\mu')d\mu'\right)\Bigg]\Bigg\}\end{aligned} \tag{3.58}$$

where

$$\begin{aligned}cos(2\pi h)&=h\\ sin(2\pi h)&=1\\ cos(0\cdot h)&=1\\ sin(0\cdot h)&=0.\end{aligned} \tag{3.59}$$

Inserting these considerations in Equation 3.58 leads to

$$\begin{aligned}\frac{1}{4\pi}\sum_{n=0}^{N}\Bigg\{(2n+1)\sum_{h=-n,h\neq 0}^{n}\Bigg[-\frac{1}{ih}P_n^h(\mu)e^{ih\omega}(1-1)\cdot \\ \cdot\left(\sum_{g'=1}^{G}\Sigma_{s,n,g'g}(x)\int_{-1}^{1}\psi_{g'}(x,\mu')P_n^h(\mu')d\mu'\right)\Bigg]\Bigg\}=0.\end{aligned} \tag{3.60}$$

For the second case, hence h equal zero, Equation 3.55 can be evaluated as:

$$\begin{aligned}\frac{1}{4\pi}\sum_{n=0}^{N}\left[(2n+1)P_n(\mu)\int_0^{2\pi}d\omega'\sum_{g'=1}^{G}\left(\Sigma_{s,n,g'g}(x)\int_{-1}^{1}\psi_{g'}(x,\mu')P_n(\mu')d\mu'\right)\right]= \\ =\sum_{n=0}^{N}\left[(2n+1)P_n(\mu)\sum_{g'=1}^{G}\left(\Sigma_{s,n,g'g}(x)\int_{-1}^{1}\frac{1}{2}\psi_{g'}(x,\mu')P_n(\mu')d\mu'\right)\right].\end{aligned} \tag{3.61}$$

The last integral is equivalent to Equation 3.47. Therefore, the scattering term takes

the following form:

$$\sum_{n=0}^{N}\left[(2n+1)P_n(\mu)\sum_{g'=1}^{G}\left(\Sigma_{s,n,g'g}(x)\int_{-1}^{1}\frac{1}{2}\psi_{g'}(x,\mu')P_n(\mu')d\mu'\right)\right] = \\ =\sum_{n=0}^{N}\left[(2n+1)P_n(\mu)\sum_{g'=1}^{G}\Sigma_{s,n,g'g}(x)\phi_{n,g'}(x)\right]. \tag{3.62}$$

Inserting the evaluated scattering term, hence Equation 3.60, and 3.62, and the Legendre expansion for the angular flux, hence Equation 3.46, in Equation 3.34, leads to the following expression:

$$\mu\frac{\partial}{\partial x}\left[\sum_{n=0}^{N}(2n+1)P_n(\mu)\phi_{n,g}(x)\right]+\Sigma_{t,g}(x)\sum_{n=0}^{N}(2n+1)P_n(\mu)\phi_{n,g}(x) = \\ =\sum_{n=0}^{N}\left[(2n+1)P_n(\mu)\sum_{g'=1}^{G}\Sigma_{s,n,g'g}(x)\phi_{n,g'}(x)\right]+S_g(x,\mu). \tag{3.63}$$

Multiplying both sides by $\frac{1}{2}P_m(\mu)$ and integrating over the domain of μ, leads to

$$\frac{1}{2}\frac{\partial}{\partial x}\left[\sum_{n=0}^{N}(2n+1)\phi_{n,g}(x)\int_{-1}^{1}\mu P_m(\mu)P_n(\mu)d\mu\right]+ \\ +\frac{1}{2}\Sigma_{t,g}(x)\sum_{n=0}^{N}\left[(2n+1)\phi_{n,g}(x)\int_{-1}^{1}P_m(\mu)P_n(\mu)d\mu\right]= \\ =\frac{1}{2}\sum_{n=0}^{N}\left[(2n+1)\sum_{g'=1}^{G}\Sigma_{s,n,g'g}(x)\phi_{n,g'}(x)\int_{-1}^{1}P_m(\mu)P_n(\mu)d\mu\right]+ \\ +\frac{1}{2}\int_{-1}^{1}P_m(\mu)S_g(x,\mu)d\mu. \tag{3.64}$$

For the integrals present in the second and third line, the orthogonality relation, defined in Equation 3.36, can be applied. Furthermore, the last term corresponds to $S_{m,g}(x)$, as given in Equation 3.51 [57]. After the insertion of these considerations and some mathematical manipulations, Equation 3.64 takes the following form:

$$\frac{1}{2}\sum_{n=0}^{N}\left[\frac{\partial\phi_{n,g}(x)}{\partial x}\int_{-1}^{1}(2n+1)\mu P_m(\mu)P_n(\mu)d\mu\right]+\Sigma_{t,g}(x)\sum_{m=0}^{M}\phi_{m,g}(x) = \\ =\sum_{m=0}^{M}\left[\sum_{g'=1}^{G}\Sigma_{s,m,g'g}(x)\phi_{m,g'}(x)+S_{m,g}(x)\right] \tag{3.65}$$

[11, 37, 57].

For the first integral of the equation, the recursion theorem of Equation 3.38 can be applied as follows:

$$\begin{aligned}\int_{-1}^{1}(2n+1)\mu P_m(\mu)P_n(\mu)d\mu = \int_{-1}^{1}\mu P_m(\mu)\left[nP_{n-1}(\mu)+(n+1)P_{n+1}(\mu)d\mu\right] = \\ =n\int_{-1}^{1}P_m(\mu)P_{n-1}(\mu)d\mu+ \\ +(n+1)\int_{-1}^{1}P_m(\mu)P_{n+1}(\mu)d\mu.\end{aligned} \tag{3.66}$$

For both integrals, the orthogonality relation of Equation 3.36 can be applied, leading to

$$\begin{aligned}n\int_{-1}^{1}P_m(\mu)P_{n-1}(\mu)d\mu+(n+1)\int_{-1}^{1}P_m(\mu)P_{n+1}(\mu)d\mu = \frac{2n}{2m+1}\delta_{n-1,m}+ \\ +\frac{2(2n+1)}{2m+1}\delta_{m,n+1}\end{aligned} \tag{3.67}$$

[37]. By inserting this formulation in Equation 3.65, the following expression is obtained:

$$\begin{aligned}\frac{1}{2}\sum_{n=0}^{N}\left\{\frac{\partial\phi_{n,g}(x)}{\partial x}\left[\frac{2n}{2m+1}\delta_{n-1,m}+\frac{2(2n+1)}{2m+1}\delta_{m,n+1}\right]\right\}+\Sigma_{t,g}(x)\sum_{m=0}^{M}\phi_{m,g}(x) = \\ =\sum_{m=0}^{M}\left[\sum_{g'=1}^{G}\Sigma_{s,m,g'g}(x)\phi_{m,g'}(x)+S_{m,g}(x)\right].\end{aligned} \tag{3.68}$$

[37]. At this point, the two Kronecker deltas must be evaluated. From the first one, it follows $n-1=m$, hence $n=m+1$. The second one, imposes $m=n+1$, therefore $n=m-1$. Including these in Equation 3.68 leads to

$$\begin{aligned}\sum_{m=0}^{M}\left[\frac{m+1}{2m+1}\frac{\partial\phi_{m+1,g}(x)}{\partial x}+\frac{m}{2m+1}\frac{\partial\phi_{m-1,g}(x)}{\partial x}\right]+\Sigma_{t,g}(x)\sum_{m=0}^{M}\phi_{m,g}(x) = \\ =\sum_{m=0}^{M}\left[\sum_{g'=1}^{G}\Sigma_{s,m,g'g}(x)\phi_{m,g'}(x)+S_{m,g}(x)\right]\end{aligned} \tag{3.69}$$

where, from Equation 3.35,

$$S_{m,g}(x)=\frac{\chi_g(x)}{k_{eff}}\sum_{g'=1}^{G}\left[\bar{\nu}_{g'}(x)\Sigma_{f,g'}(x)\phi_{0,g'}(x)\right]. \tag{3.70}$$

It should be remarked that ϕ_0 is the scalar neutron flux [11, 37, 57].

The scattering term can be splitted into scattering within the same energy group and scattering between different energy groups, hence

$$\sum_{g'=1}^{G} \Sigma_{s,m,g'g}(x)\phi_{m,g'}(x) = \begin{cases} \Sigma_{s,m,gg}(x)\phi_{m,g}(x), & \text{for} \quad g' = g \\ \sum_{g'=1}^{G} \Sigma_{s,m,g'g}(x)\phi_{m,g'}(x), & \text{for} \quad g' \neq g \end{cases} = \\ = \Sigma_{s,m,gg}(x)\phi_{m,g}(x) + \sum_{g'=1, g'\neq g}^{G} \Sigma_{s,m,g'g}(x)\phi_{m,g'}(x). \tag{3.71}$$

Including the separation of the scattering term in Equation 3.69, the following expression is obtained:

$$\sum_{m=0}^{M} \left[\frac{m+1}{2m+1} \frac{\partial \phi_{m+1,g}(x)}{\partial x} + \frac{m}{2m+1} \frac{\partial \phi_{m-1,g}(x)}{\partial x} \right] + \Sigma_{t,g}(x) \sum_{m=0}^{M} \phi_{m,g}(x) = \\ = \sum_{m=0}^{M} \left[\Sigma_{s,m,gg}(x)\phi_{m,g}(x) + \sum_{g'=1, g'\neq g}^{G} \Sigma_{s,m,g'g}(x)\phi_{m,g'}(x) + S_{m,g}(x) \right]. \tag{3.72}$$

The scattering between energy groups can be seen as a neutron source, therefore it can be included in the source term, together with the external neutron source and the fission source. Relabelling m with n, the source term takes the following form

$$\tilde{S}_{n,g}(x) = \sum_{g'=1, g'\neq g}^{G} \Sigma_{s,n,g'g}(x)\phi_{n,g'}(x) + S_{n,g}(x) = \\ = \sum_{g'=1, g'\neq g}^{G} \Sigma_{s,n,g'g}(x)\phi_{n,g'}(x) + \frac{\chi_g(x)}{k_{eff}} \sum_{g'=1}^{G} \bar{\nu}_{g'}(x)\Sigma_{f,g'}(x)\phi_{0,g'}(x) \tag{3.73}$$

[57]. Finally, relabelling also in Equation 3.72 m with n and M with N, the general formulation of the one dimensional P_N approximation can be achieved, which is constituted by Equation 3.73, together with the following expression:

$$\sum_{n=0}^{N} \left\{ \frac{n+1}{2n+1} \frac{\partial \phi_{n+1,g}(x)}{\partial x} + \frac{n}{2n+1} \frac{\partial \phi_{n-1,g}(x)}{\partial x} + \right. \\ \left. + \left[\Sigma_{t,g}(x) - \Sigma_{s,n,gg}(x) \right] \phi_{n,g}(x) \right\} = \sum_{n=0}^{N} \tilde{S}_{n,g}(x) \tag{3.74}$$

[11, 37, 57].

3.3 Towards the steady state SP_3 approximation of the transport equation, to its Galerkin representation and the algorithms implemented in FENNECS to solve it

For the SP_N approximation, a review of its mathematical as well as numerical aspects can be found in [53]. In [41], which is included in this section, the derivation of the steady state P_3 approximation of the neutron transport equation in 1D will be carried out, starting from the one-dimensional steady state P_N method, described by Equation 3.73, and 3.74. The P_3 approximation of the neutron transport equation in 1D will be used to obtain the three dimensional steady state SP_3 approximation of the neutron transport equation, together with the boundary conditions. These will be incorporated in the two coupled equations of the SP_3 methodology. As next step, the SP_3 equations, including the boundary conditions, will be taken into the Galerkin form, necessary to implement this methodology in a finite element based code, like FENNECS. With this last step, the first phase of Figure 1.2 is concluded.

In [41], the first step of the second phase is accomplished: the algorithms, necessary to solve the steady state SP_3 equations (in Galerkin form), which were not present in FENNECS, or which had to be modified to support the new methodology, are explained.

Annals of Nuclear Energy 200 (2024) 110303

Contents lists available at ScienceDirect

Annals of Nuclear Energy

journal homepage: www.elsevier.com/locate/anucene

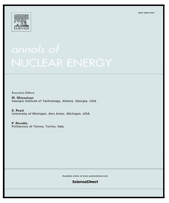

Implementation of the steady state simplified P3 (SP3) transport solver in the finite element neutronic code FENNECS, Part 1: Theory

Silvia lo Muzio *, Armin Seubert

Gesellschaft fur Anlagen- und Reaktorsicherheit (GRS) gGmbH Safety Research Division, Nuclear Fuel Department, Boltzmannstr. 14, D-85748 Garching, Germany

ARTICLE INFO

Keywords:
SP_3 approximation
FENNECS
Galerkin form
Transport equation
P_N
Finite element method

ABSTRACT

Codes based on the neutron transport equation require large computational resources if the code is deterministic, and even more if the code is Monte Carlo based. Additionally, the amount of required resources increases drastically for transient scenarios, particularly for Monte Carlo codes. Approximations can be applied to reduce the costs. Diffusion theory is the most widely used. However, it shows limitations for small and heterogeneous configurations, like (v)SMR and MMR. An alternative is the SP_3 approximation. Therefore, the GRS neutronics code FENNECS was extended by a steady state SP_3 solver in order to be able to perform the safety assessment of (v)SMR and MMR. In this work, firstly, the system of the steady state SP_3 equations was derived, including the boundary conditions. Since FENNECS is a finite element based code, the Galerkin form of the equations was obtained. Finally, the algorithms used to solve the SP_3 equations are briefly explained.

1. Introduction

(Very) small modular reactors ((v)SMR) and micro modular rectors (MMR) are receiving a big interest in the last years. As consequence, it follows the necessity to find adequate neutronics tools for their safety assessment.

The search starts by analysing the two main families of neutronic codes: Monte Carlo and deterministic ones (Ghasabyan, 2013). The codes of the first category are renomated for their high geometrical flexibility, essential to model small and heterogeneous systems, like (v)SMR and MMR, but also for the long calculation time, which makes them quite unpractical for routine calculations (Ghasabyan, 2013; Willert et al., 2013; Cao and Wu, 2021). Furthermore, Monte Carlo results suffer from statistical fluctuations (Harrison, 2010). On the contrary, deterministic codes deliver in a short time invariated results (Ghasabyan, 2013). Due to their shorter computational times, they are more practical to simulate transient scenarios.

There exist various types of deterministic codes, depending on if they solve the neutron transport equation or just and approximation of it and if this is the case, on which approximation they solve. Codes solving the neutron transport equation, which describes the angular neutron flux, are the most accurate ones (Cox et al., 2019). However, to solve the neutron transport equation is computationally expensive, due to the presence of seven independent variables (Cao and Wu, 2021; Avvakumov et al., 2019). Therefore, to reduce the calculation times, it is necessary to apply approximations.

The most popular one is diffusion theory, which is derived from Fick's law (Stacey, 2007; Mohanakrishnan et al., 2021). This approximation of the neutron transport equation consists in assuming isotropic scattering, much smaller probability of absorption compared to scattering and a slow varying neutron flux in space (Avvakumov et al., 2019; Stacey, 2007; Marguet, 2018; Devan and Bachchan, 2021). The first assumption is true for low energy scattering with heavy mass nuclei (Devan and Bachchan, 2021). The second one is not fulfilled for strong absorbers, like the control elements (Devan and Bachchan, 2021; Hore-Lacy, 2010). Regarding the last assumption, even for large and homogeneous media, this is satisfied only a few mean free paths away from the medium boundary (Devan and Bachchan, 2021). Thus, the diffusion approximation may not be applicable near material interfaces and for small and heterogeneous cores, like (v)SMR and MMR (Devan and Bachchan, 2021; Bal and Ryzhik, 2000).

A more accurate approximation, suited for the modelling of (v)SMR and MMR, is the third order simplified spherical harmonics approximation of the transport equation (SP_3), originally proposed in Gelbard (1960). It is obtained by expanding the angular terms of the 1D transport equation with Legendre's polynomials up to the third order and by extending the equations to 3D, without replacing the Legendre's polynomials with spherical harmonics functions (Stacey, 2007).

Independently on the equation solved by the code, a program able to model the complex and heterogeneous geometries of (v)SMR and MMR must be found. A candidate is Finite ElemeNt NeutroniCS

* Corresponding author.
E-mail address: silvia.lo-muzio@grs.de (S. lo Muzio).

https://doi.org/10.1016/j.anucene.2023.110303
Received 4 July 2023; Received in revised form 24 October 2023; Accepted 12 December 2023
Available online 1 February 2024
0306-4549/© 2024 Elsevier Ltd. All rights reserved.

(FENNECS), originally a diffusion code, whose main advantage is its geometrical flexibility (Seubert, 2020). Since the diffusion as well as the SP_3 equations have a similar structure, it is particularly convenient to extend FENNECS by an SP_3 solver, in order to be able to perform the safety assessment of (v)SMR and MMR with a high accuracy, but low resources demand.

Since FENNECS is not the only code offering an SP_3 solver, in Section 2 a short overview of similar codes will be given. Afterwards, in Section 3, the main features of FENNECS will be explained, in order to understand why this code is different from the others. Then, starting from the neutron transport equation, the two equations of the steady state SP_3 approximation are obtained. Finally, since FENNECS is based on the finite element method, in order to implement the derived SP_3 equations in FENNECS, their Galerkin form is found.

2. Codes offering an SP_3 solver

Examples of codes, which offer an SP_3 solver are PARCS, TRIVAC, FEMFFUSION, SPNDYN and the Denovo radiation transport code. These will be shortly introduced in the next paragraphs.

The first code able to solve the multigroup SP_3 equations is the Purdue Advanced Reactor Core Simulator (PARCS), which additionally provides a diffusion solver (Downar et al., 2012). With the PARCS SP_3 solver, only Cartesian configurations can be modelled. Steady state as well as in transient scenarios can be reproduced (Downar et al., 2012).

Another example is developed at "École Polytechnique de Montréal" and is a multigroup and multidimensional code, capable to calculate the neutron flux for hexagonal as well as Cartesian configurations (Hébert, 2012). The calculation is based on the discretization of the diffusion or SP_N equations, forming a matrix system (Hébert, 2012). The discretization is done with multiple techniques, like mesh centred finite difference or finite element method (Hébert, 2012). This system is then solved using iterative methods, like preconditioned or inverse power method, as well as triangular factorization (Hébert, 2012).

Also FEMFFUSION is based on the finite element method and the spatial discretization is performed with the continuous Galerkin approach (Vidal Ferràndiz et al., 2023). It solves the diffusion as well as SP_N equations in up to three dimensions (Vidal Ferràndiz et al., 2023).

A further neutronic code, based on the continuous Galerkin finite element approach and which offers an SP_3 solver is SPNDYN (Babcsány et al., 2022). This code is also able to calculate the hybrid finite element solution of these equations (Babcsány et al., 2022). This approach provides also a module for the calculation of discontinuity factors (Babcsány et al., 2022).

Finally, in Hamilton and Evans (2015), the implementation of the SP_N equations in the Denovo radiation transport code is explained. Here, multiple eigensolvers based on different methodologies are available (Hamilton and Evans, 2015). These are the power, inverse power and Rayleigh quotient iteration as well as Arnoldi and Davidson method (Hamilton and Evans, 2015). For each of them, in total three different preconditioners are considered (Hamilton and Evans, 2015). These are firstly a threshold incomplete LU factorization, secondly an algebraic multigrid and thirdly a multigrid in energy (Hamilton and Evans, 2015).

3. FENNECS

FENNECS is a deterministic neutronics code, recently developed at Gesellschaft für Anlagen- und Reaktorsicherheit gGmbH (GRS) (Seubert et al., 2021). At the beginning, it was a 3D few group finite element based steady state and transient diffusion code (Seubert et al., 2021; Bousquet et al., 2020). FENNECS applies the finite element method (FEM) with the Galerkin weighted residual approach, where the spatial discretization is performed with upright triangular prisms with linear basis functions (Bousquet et al., 2020). The code, written in FORTRAN, is a module of the GRS code package AC^2 (ATHLET, ATHLET-CD, COCOSYS).[1]

4. The finite element method

The definition of the Finite Element Method is based on two pillars. The first one is the discretized problem domain (Zienkiewicz et al., 2013). Therefore, the geometry is subdivided into a finite number of parts, hence elements, that are upright triangular prisms in the case of FENNECS, which are connected to each other through nodes (Bousquet et al., 2020; Zienkiewicz et al., 2013, 2005b). The behaviour of the elements is described by their properties. The second pillar concerns the solution of the set of elements: all the elements obey to the same rules (Zienkiewicz et al., 2005b).

In the first step, for each of the in total K elements composing the geometry, the linear local system of equations must be set up. This is done by defining, for all K elements, a matrix with the nodes properties that must be multiplied by the searched unknown quantity of each node (Zienkiewicz et al., 2005b). Then, all the local matrices are assembled together and a global system matrix, known as "stiffness matrix" in structural mechanics, is composed (Zienkiewicz et al., 2005b). This matrix is multiplied by a vector containing the unknowns for each node, which are displacements in the case of structural mechanics (Zienkiewicz et al., 2005b). In the next step, a vector for each element with the remaining properties not subjected to a multiplication by the searched unknowns is assembled. The obtained K vectors are then assembled. Afterwards, the boundary conditions are included in the system of equations. This step is essential in order to solve the system of equations. Finally, the linear system of equations is solved.

In structural mechanics, the unknown quantities are normally the displacements. Consider a set of differential equations, where the function $F(\vec{r})$ is the unknown function, such that the right hand side of all equations is zero (Zienkiewicz et al., 2005a). Similarly holds also for the boundary conditions. The solution for a certain element e may be approximated as

$$F^e(\vec{r}) \approx \sum_{j=1}^{J} \varphi_j(\vec{r}) f_j^e = \vec{\varphi}(\vec{r})\vec{f}^e, \forall \vec{r} \in e \tag{1}$$

where J is the number of nodes of the finite element, φ_j the shape or test function of node j and the unknown quantity f is the expansion coefficient related to node j in the element e (Zienkiewicz et al., 2005a). It should be remarked that the test functions are defined locally for the elements (Zienkiewicz et al., 2005a). Considering the set of differential equations and boundary conditions, the weak, or Galerkin approach consist in imposing that the integral over the problem domain of the set of differential equations, multiplied by the test functions added to the boundary conditions multiplied by the test functions and integrated over the domain boundary must be zero (Zienkiewicz et al., 2005a).

5. From the neutron transport equation to the system of SP_3 equations

For the derivation of the steady state SP_3 approximation, the starting point is the one dimensional steady state neutron transport equation with discretized energy groups, obtained from (Stacey, 2007; Burrone, 2018; Dürigen, 2013; Lewis and Miller, 1984), which looks as follows:

$$\mu \frac{\partial}{\partial x}\psi_g(x,\mu) + \Sigma_{t,g}(x)\psi_g(x,\mu) = \\ = \frac{1}{4\pi}\sum_{g'=1}^{G}\left\{\int_{-1}^{1}\left[\int_0^{2\pi}\Sigma_{s,g'g}(x,\mu_0)\psi_{g'}(x,\mu')d\omega'\right]d\mu'\right\} + S_g(x,\mu) \tag{2}$$

[1] A copy of the current FENNECS release can be obtained from GRS upon request

where

$$S_g(x,\mu) = \frac{\chi_g(x)}{k_{eff}} \sum_{g'=1}^{G} \left[\bar{\nu}_{g'}(x)\Sigma_{f,g'}(x)\phi_{g'}(x)\right] + S_{ex,g}(x,\mu) \tag{3}$$

is the neutron source term. The energy discretization is performed such that $g \in (1,\dots,G)$, where $g = 1$ is the fastest energy group and $g = G$ the slowest one. In Eq. (2), μ is the cosine of θ, which together with ω, are the angles of the neutron travelling direction with respect to the x and y axis, respectively. The main quantity of interest is ψ, which describes the angular neutron flux. The cross sections are represented by Σ and the subscripts t, s, and f indicate the total, scattering and fission cross sections, respectively. The quantities followed by an apostrophe represent the neutron state before the scattering or fission reaction. In particular, $\Sigma_{s,g'g}(x,\mu_0)$ is the scattering from energy group g' to g, where μ_0 is the cosine of the angle between the travelling direction before and after the scattering event. In Eq. (3), χ, k_{eff}, and $\bar{\nu}$ are the fission spectrum, the effective multiplication factor and the average number of neutrons emitted per fission reaction, respectively. Finally, ϕ is the scalar flux and S_{ex} is an external neutron source.

5.1. The one dimensional P_3 approximation

Since the SP_3 is a simplification of the third order spherical (P_3) approximation of the transport equation, which is derived from the N-th order spherical harmonics (P_N) approximation, the first step is to obtain the equations for the P_N approximation in 1D. This last approach consists in expanding with N Legendre's polynomials the angular terms of the one dimensional neutron transport equation (Stacey, 2007; Lewis and Miller, 1984). From Burrone (2018), Lewis and Miller (1984), Kaplan (1992), for any function $w(\mu)$, its expansion reads as follows:

$$w(\mu) \approx \sum_{n=0}^{N} (2n+1) P_n(\mu) w_n \tag{4}$$

where

$$w_n = \frac{1}{2}\int_{-1}^{1} w(\mu) P_n(\mu) d\mu. \tag{5}$$

Here, P_n is the n-th order Legendre's function. Therefore, by replacing with Eq. (4) the terms of Eq. (2), which have an angular dependency, hence the angular neutron flux, the scattering cross section, and the source term, the P_N approximation is obtained (Stacey, 2007; Burrone, 2018; Lewis and Miller, 1984; Dürigen, 2013). At this point, the P_3 approximation is obtained by inserting $n = 0,1,2,3$, hence by considering only the first four orders, obtaining the following four equations

$$\frac{\partial \phi_{1,g}(x)}{\partial x} + \left[\Sigma_{t,g}(x) - \Sigma_{s,0,gg}(x)\right]\phi_{0,g}(x) = \tilde{S}_{0,g}(x) \tag{6}$$

$$\frac{2}{3}\frac{\partial \phi_{2,g}(x)}{\partial x} + \frac{1}{3}\frac{\partial \phi_{0,g}(x)}{\partial x} + \left[\Sigma_{t,g}(x) - \Sigma_{s,1,gg}(x)\right]\phi_{1,g}(x) = 0 \tag{7}$$

$$\frac{3}{5}\frac{\partial \phi_{3,g}(x)}{\partial x} + \frac{2}{5}\frac{\partial \phi_{1,g}(x)}{\partial x} + \left[\Sigma_{t,g}(x) - \Sigma_{s,2,gg}(x)\right]\phi_{2,g}(x) = 0 \tag{8}$$

$$\frac{3}{7}\frac{\partial \phi_{2,g}(x)}{\partial x} + \left[\Sigma_{t,g}(x) - \Sigma_{s,3,gg}(x)\right]\phi_{3,g}(x) = 0 \tag{9}$$

where

$$\begin{aligned}\tilde{S}_{0,g}(x) &= \sum_{g'=1,g'\neq g}^{G} \Sigma_{s,0,g'g}(x)\phi_{0,g'}(x) + S_{0,g}(x) = \\ &= \sum_{g'=1,g'\neq g}^{G} \Sigma_{s,0,g'g}(x)\phi_{0,g'}(x) + \\ &\quad + \frac{\chi_g(x)}{k_{eff}} \sum_{g'=1}^{G} \bar{\nu}_{g'}(x)\Sigma_{f,g'}(x)\phi_{0,g'}(x) + S_{ex,0,g}(x)\end{aligned} \tag{10}$$

(Stacey, 2007; Burrone, 2018; Dürigen, 2013; Lewis and Miller, 1984). Similarly to Dürigen (2013), also here, it is assumed that the higher order scattering between energy groups is neglected. From this assumption, the within-group form is obtained (Dürigen, 2013). If the higher order scattering between energy groups would be considered, to solve such system would require a very large resources demand Dürigen (2013). However, in Section 6, an approach is presented to account for the first order scattering between energy groups, without increasing the resources demand. Furthermore, the external neutron source can be assumed to be isotropic, implying that only $S_{ex,0,g}(x)$ is unequal zero. From Eq. (7), the neutron current $\phi_{1,g}(x)$ can be obtained:

$$\phi_{1,g}(x) = -D_{0,g}(x)\frac{\partial}{\partial x}\left[\phi_{0,g}(x) + 2\phi_{2,g}(x)\right] \tag{11}$$

(Dürigen, 2013). Using Eq. (9), an expression for the third order flux can be written:

$$\phi_{3,g}(x) = -D_{1,g}(x)\frac{\partial}{\partial x}\phi_{2,g}(x) \tag{12}$$

(Dürigen, 2013). Here, $D_{0,g}$ and $D_{1,g}$ are the zeroth and first order diffusion coefficients, respectively, which are defined as

$$D_{0,g}(x) = \frac{1}{3\left[\Sigma_{t,g}(x) - \Sigma_{s,1,gg}(x)\right]} \tag{13}$$

$$D_{1,g}(x) = \frac{3}{7\left[\Sigma_{t,g}(x) - \Sigma_{s,3,gg}(x)\right]} \tag{14}$$

(Stacey, 2007; Dürigen, 2013). By defining $F_{0,g}(x)$ and $F_{1,g}(x)$ as follows

$$F_{0,g}(x) = \phi_{0,g}(x) + 2\phi_{2,g}(x) \tag{15}$$

$$F_{1,g}(x) = \phi_{2,g}(x). \tag{16}$$

Eq. (11), and (12) can be rewritten as

$$\phi_{1,g}(x) = -D_{0,g}(x)\frac{\partial}{\partial x}F_{0,g}(x) \tag{17}$$

and

$$\phi_{3,g}(x) = -D_{1,g}(x)\frac{\partial}{\partial x}F_{1,g}(x) \tag{18}$$

respectivelly.

The next step is to insert the equations with an odd n in the ones with an even n. Therefore, in Eqs. (6) and (8), the definitions of the neutron current, third order flux as well as of $F_{0,g}$ and $F_{1,g}$ are inserted, leading to

$$\begin{aligned}-\frac{\partial}{\partial x}\left[D_{0,g}(x)\frac{\partial}{\partial x}F_{0,g}(x)\right] + F_{0,g}(x)\left[\Sigma_{t,g}(x) - \Sigma_{s,0,gg}(x)\right] + \\ -2F_{1,g}(x)\left[\Sigma_{t,g}(x) - \Sigma_{s,0,gg}(x)\right] = \tilde{S}_{0,g}(x)\end{aligned} \tag{19}$$

$$\begin{aligned}-\frac{2}{3}F_{0,g}(x)\left[\Sigma_{t,g}(x) - \Sigma_{s,0,gg}(x)\right] - \frac{\partial}{\partial x}\left[D_{1,g}(x)\frac{\partial}{\partial x}F_{1,g}(x)\right] + \\ +F_{1,g}(x)\left\{\frac{4}{3}\left[\Sigma_{t,g}(x) - \Sigma_{s,0,gg}(x)\right] + \frac{5}{3}\left[\Sigma_{t,g}(x) - \Sigma_{s,2,gg}(x)\right]\right\} = \\ = -\frac{2}{3}\tilde{S}_{0,g}(x).\end{aligned} \tag{20}$$

Including also in the source term the definitions for $F_{0,g}$ and $F_{1,g}$, this is expressed as follows:

$$\begin{aligned}\tilde{S}_{0,g}(x) = \sum_{g'=1,g'\neq g}^{G} \Sigma_{s,0,g'g}(x)\left[F_{0,g'}(x) - 2F_{1,g'}(x)\right] + \\ +\frac{\chi_g(x)}{k_{eff}}\sum_{g'=1}^{G}\bar{\nu}_{g'}(x)\Sigma_{f,g'}(x)\left[F_{0,g'}(x) - 2F_{1,g'}(x)\right] + S_{ex,0,g}(x).\end{aligned} \tag{21}$$

6. Alternative definition of the zeroth order diffusion coefficient

At this point, some considerations must be made regarding the zeroth order diffusion coefficient. For this quantity, an alternative definition can be found, if the first order scattering between energy groups is not neglected. Hence, considering the zeroth as well as first

order scattering between energy groups, the zeroth order diffusion coefficient is written as follows

$$D_{0,g}(x) = \frac{1}{3\left[\Sigma_{t,g}(x) - \sum_{g'=1}^{G}\Sigma_{s,1,g'g}(x)\right]}. \tag{22}$$

As explained in Bell and Glasstone (1970), considering a continuous energy spectrum, the following assumption can be adopted:

$$\int \Sigma_{s,1}(x, E' \to E)\phi_1(x, E')dE' \approx \int \Sigma_{s,1}(x, E \to E').\phi_1(x, E)dE. \tag{23}$$

This assumption is based on the argument that for the left hand side of Eq. (23) the contribution from the slowing down region, hence from scattering processes with $E' > E$, is nearly the same as the one from the slowing down region for the right hand side, hence for scattering processes with $E > E'$ (Bell and Glasstone, 1970; Beckert and Grundmann, 2007).

Reformulating the macroscopic scattering cross section of first order, the left hand side can be written as

$$\int \Sigma_{s,1}(x, E \to E')\phi_1(x, E')dE' = \Sigma_{s,0}\bar{\mu}_0(x, E)(x, E \to E')\phi_1(x, E)dE \tag{24}$$

where $\bar{\mu}_0(x, E)$ is the average cosine of the scattering angle, which is θ_0 (Beckert and Grundmann, 2007).

$\bar{\mu}_0(x, E)$ is also involved in the definition of the macroscopic transport cross section, which can be written as

$$\Sigma_{tr}(x, E) \equiv \Sigma_t(x, E)\int \Sigma_{s,1}(x, E \to E')dE' = \Sigma_t(x, E) - \bar{\mu}_0(x, E)\Sigma_{s,0}(x, E) \tag{25}$$

(Beckert and Grundmann, 2007).

Discretizing the energy spectrum in Eq. (25), the following definition of the transport cross section is obtained

$$\Sigma_{tr,g}(x) \equiv \Sigma_{t,g}(x) - \sum_{g'=1}^{G}\Sigma_{s,1,g'g}(x) \tag{26}$$

(Beckert and Grundmann, 2007).

Inserting Eq. (26) in the definition of $D_{0,g}(x)$, hence Eq. (22), leads to the following alternative formulation of the zeroth order diffusion coefficient:

$$D_{0,g}(x) = \frac{1}{3\Sigma_{tr,g}(x)} \tag{27}$$

(Beckert and Grundmann, 2007). Based on the assumption of Eq. (23), this approach allows to consider for the first order scattering between energy groups, without drastically increasing the resources demand for the computation. In FENNECS, both definitions of the zeroth order diffusion coefficient are implemented. However, the definition given in Eq. (13) is the most used one, and therefore it is the default option.

6.1. The SP_3 approximation

The SP_3 approximation of the transport equation is obtained by extending the one-dimensional P_3 approximation to three-dimensional, without substituting the Legendre's polynomials with spherical harmonics functions (Stacey, 2007). As explained in Section 4, in the finite element method, the geometry is discretized into elements. At this point, a first step towards the finite elements discretization can be done: it is assumed that the nuclear data are constant within the finite element e. Consequently, the two equations of the SP_3 approximation can be written as

$$\left\{-D^e_{0,g}\Delta + \left[\Sigma^e_{t,g} - \Sigma^e_{s,0,gg}\right]\right\}F_{0,g}(\vec{r}) - 2\left[\Sigma^e_{t,g} - \Sigma^e_{s,0,gg}\right]F_{1,g}(\vec{r}) = \\ = \tilde{S}_{0,g}(\vec{r}), \forall\vec{r} \in e \tag{28}$$

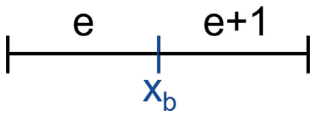

Fig. 1. Neighbouring elements e and $e+1$, touching in x_b.

$$-\frac{2}{3}\left[\Sigma^e_{t,g} - \Sigma^e_{s,0,gg}\right]F_{0,g}(\vec{r}) + \left\{D^e_{1,g}\Delta + \frac{4}{3}\left[\Sigma^e_{t,g} - \Sigma^e_{s,0,gg}\right] + \right. \\ \left. + \frac{5}{3}\left[\Sigma^e_{t,g} - \Sigma^e_{s,2,gg}\right]\right\}F_{1,g}(\vec{r}) = -\frac{2}{3}\tilde{S}_{0,g}(\vec{r}), \forall\vec{r} \in e \tag{29}$$

with

$$\tilde{S}_{0,g}(\vec{r}) = \sum_{g'=1,g'\neq g}^{G}\Sigma^e_{s,0,g'g}\left[F_{0,g'}(\vec{r}) - 2F_{1,g'}(\vec{r})\right] + \\ + \frac{\chi^e_g}{k_{eff}}\sum_{g'=1}^{G}\bar{\nu}^e_{g'}\Sigma^e_{f,g'}\left[F_{0,g'}(\vec{r}) - 2F_{1,g'}(\vec{r})\right] + S_{ex,0,g}(\vec{r}), \forall\vec{r} \in e \tag{30}$$

and

$$F_{0,g}(\vec{r}) = \phi_{0,g}(\vec{r}) + 2\phi_{2,g}(\vec{r}) \tag{31}$$

$$F_{1,g}(\vec{r}) = \phi_{2,g}(\vec{r}). \tag{32}$$

6.2. Interface boundary condition

The interface, or continuity, boundary condition has the goal to ensure that the angular neutron flux is continuous between finite elements. As it was done for the two SP_3 equations, the derivation will be firstly carried out in 1D and then extended for 3D. To ensure the continuity for the two elements e and $e+1$, represented in Fig. 1, it must be imposed that the angular neutron flux must be identical in the touching point x_b, hence

$$\psi^e_g(x_b, \mu) = \psi^{e+1}_g(x_b, \mu) \tag{33}$$

(Dürigen, 2013). Here, applying the P_3 approximation, hence expanding the angular flux in terms of Legendre's polynomials up to the third order, leads to the following four equations:

$$\phi^e_{m,g}(x_b) = \phi^{e+1}_{m,g}(x_b), m = 0, 1, 2, 3 \tag{34}$$

(Dürigen, 2013).

After the inclusion of the expressions for the neutron current, third order flux, F_0 and F_1, these four equations can be written compactly as

$$F^e_{k,g}(x_b) = F^{e+1}_{k,g}(x_b), k = 0, 1 \tag{35}$$

$$D^e_{k,g}\frac{\partial}{\partial x}F^e_{k,g}(x_b) - D^{e+1}_{k,g}\frac{\partial}{\partial x}F^{e+1}_{k,g}(x_b) = 0, k = 0, 1 \tag{36}$$

(Dürigen, 2013). Inserting the first equation in the second one leads to

$$\left[D^e_{k,g} - D^{e+1}_{k,g}\right]\frac{\partial}{\partial x}F^e_{k,g}(x_b) = 0, k = 0, 1. \tag{37}$$

This equation is fulfilled if

$$D^e_{k,g} - D^{e+1}_{k,g} = 0, k = 0, 1 \tag{38}$$

or

$$\frac{\partial}{\partial x}F^e_{k,g}(x_b) = 0, k = 0, 1. \tag{39}$$

Eq. (38) is true if the coefficients of both finite elements are identical and this cannot be guaranteed. Therefore, Eq. (39) must hold and it constitutes the continuity boundary condition. Extending to 3D, the equation can be written as

$$\nabla F_{k,g}(\vec{r}) = 0, k = 0, 1, \forall\vec{r} \in \partial\Gamma^I. \tag{40}$$

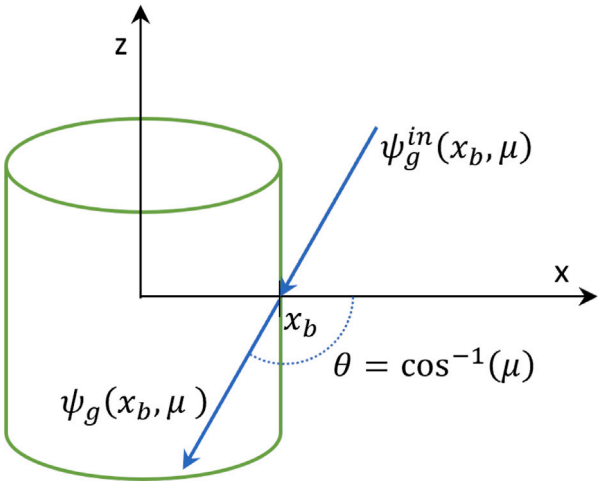

Fig. 2. Representation of the external boundary condition.

Here, $\partial\Gamma^I$ is the common face of the prismatic elements e and $e+1$. Actually, it is the intersection between the two finite elements, hence $\partial\Gamma^I = \partial\Gamma^e \cap \partial\Gamma^{e+1}$. More in general, Eq. (40) can be written as

$$D_{k,g}\nabla F_{k,g}(\vec{r}) = -\frac{1}{\gamma(\vec{r})}\left[\beta_k(\vec{r})F_{0,g}(\vec{r}) + \alpha_k(\vec{r})F_{1,g}(\vec{r})\right], k = 0,1, \forall\vec{r} \in \partial\Gamma^I \quad (41)$$

where, for the continuity boundary condition, the following holds:

$$\frac{1}{\gamma(\vec{r})} = 0, \forall\vec{r} \in \partial\Gamma^I. \quad (42)$$

6.3. External boundary conditions

Also for the external boundary conditions, firstly the one-dimensional geometry will be considered. As depicted in Fig. 2, at the external boundary of the geometry, the angular flux at the boundary, hence $\psi_g(x_b,\mu)$, is equal to the incoming $\psi_g^{in}(x_b,\mu)$ angular flux, if $-1 \le \mu \le 0$, hence:

$$\psi_g(x_b,\mu) = \psi_g^{in}(x_b,\mu), -1 \le \mu \le 0. \quad (43)$$

By expanding $\psi_g(x_b,\mu)$ with the first three Legendre's polynomials and by multiplying both sides of the equation by $P_m(\mu)$, after the integration over μ, Eq. (43) can be written as

$$\sum_{n=0}^{3}\phi_{n,g}(x_b)\int_{-1}^{0}P_n(\mu)P_m(\mu)d\mu = \int_{-1}^{0}\psi_g^{in}(x_b,\mu)P_m(\mu)d\mu, -1 \le \mu \le 0. \quad (44)$$

Since only the odd Legendre's polynomials indicate the directionality, after the evaluation of the integrals for $m = 1$ and $m = 3$, the following two equations are obtained:

$$-\frac{1}{2}\phi_{0,g}(x_b) + \phi_{1,g}(x_b) - \frac{5}{8}\phi_{2,g}(x_b) = \int_{-1}^{0}\psi_g^{in}(x_b,\mu)P_1(\mu)d\mu \quad (45)$$

$$\frac{1}{8}\phi_{0,g}(x_b) - \frac{5}{8}\phi_{2,g}(x_b) + \phi_{3,g}(x_b) = \int_{-1}^{0}\psi_g^{in}(x_b,\mu)P_3(\mu)d\mu. \quad (46)$$

The so-called Marshak boundary condition is obtained by inserting the expressions for the odd order fluxes as well as for F_0 and F_1, obtaining the following expressions:

$$-\frac{1}{2}F_{0,g}(x_b) + \frac{3}{8}F_{1,g}(x_b) - D_{0,g}\frac{\partial}{\partial x}F_{0,g}(x_b) = \int_{-1}^{0}\psi_g^{in}(x_b,\mu)P_1(\mu)d\mu \quad (47)$$

$$\frac{1}{8}F_{0,g}(x_b) - \frac{7}{8}F_{1,g}(x_b) - D_{1,g}\frac{\partial}{\partial x}F_{1,g}(x_b) = \int_{-1}^{0}\psi_g^{in}(x_b,\mu)P_3(\mu)d\mu \quad (48)$$

(Dürigen, 2013).

At this point, $\psi_g^{in}(x_b,\mu)$ must be evaluated, which depends on the type of boundary condition. For the three types of boundary conditions, $\psi_g^{in}(x_b,\mu)$ can be expressed as

$$\psi_g^{in}(x_b,\mu) = \tau(x_b)\psi_g(x_b,-\mu), -1 \le \mu \le 0 \quad (49)$$

with

$$\tau(x_b) = \begin{cases} 0, & \text{vacuum boundary condition, hence } \forall x_b \in \partial\Gamma^V \\ 1, & \text{reflective boundary condition, hence } \forall x_b \in \partial\Gamma^R \\ -1, & \text{zero-flux boundary condition, hence } \forall x_b \in \partial\Gamma^{ZF} \end{cases} \quad (50)$$

where $\partial\Gamma^V$, $\partial\Gamma^R$, and $\partial\Gamma^{ZF}$ are the vacuum, reflective and zero flux boundary of the geometry, respectivelly (Dürigen, 2013). In Eq. (49), the angular flux can be expanded in terms of Legendre's polynomials and then multiplied by $P_1(\mu)$ and $P_3(\mu)$. After the integration over the domain of μ, the following two equations are obtained:

$$\begin{aligned}&\int_{-1}^{0}\psi_g^{in}(x_b,\mu)P_1(\mu)d\mu = \\ &= \tau(x_b)\int_{-1}^{0}\left[P_1(\mu)P_0(-\mu)\phi_{0,g}(x_b) + 3P_1(\mu)P_1(-\mu)\phi_{1,g}(x_b) + \right. \\ &\left. + 5P_1(\mu)P_2(-\mu)\phi_{2,g}(x_b) + P_1(\mu)P_3(-\mu)\phi_{3,g}(x_b)\right]d\mu\end{aligned} \quad (51)$$

$$\begin{aligned}&\int_{-1}^{0}\psi_g^{in}(x_b,\mu)P_3(\mu)d\mu = \\ &= \tau(x_b)\int_{-1}^{0}\left[P_3(\mu)P_0(-\mu)\phi_{0,g}(x_b) + 3P_3(\mu)P_1(-\mu)\phi_{1,g}(x_b) + \right. \\ &\left. + 5P_3(\mu)P_2(-\mu)\phi_{2,g}(x_b) + P_3(\mu)P_3(-\mu)\phi_{3,g}(x_b)\right]d\mu.\end{aligned} \quad (52)$$

As stated in Phillips (2006), the order of the Legendre's polynomial indicates if the function is odd or even: if the Legendre's polynomial has an even order, it will be an even function and on the contrary, if the order is odd, the function will be odd. For even functions, the following holds:

$$g(-x) = g(x) \quad (53)$$

(Powers, 2007). Similarly, odd functions, obey to the following relation:

$$g(-x) = -g(x) \quad (54)$$

(Powers, 2007). Inserting these properties in Eqs. (51) and (52) and including the formulations for F_0 and F_1, as well as for the odd order fluxes, leads to

$$\int_{-1}^{0}\psi_g^{in}(x_b,\mu)P_1(\mu)d\mu = \tau(x_b)\left[-\frac{1}{2}F_{0,g}(x_b) + \frac{3}{8}F_{1,g}(x_b) + D_{0,g}\frac{\partial}{\partial x}F_{0,g}(x_b)\right] \quad (55)$$

$$\int_{-1}^{0}\psi_g^{in}(x_b,\mu)P_3(\mu)d\mu = \tau(x_b)\left[\frac{1}{8}F_{0,g}(x_b) - \frac{7}{8}F_{1,g}(x_b) + D_{1,g}\frac{\partial}{\partial x}F_{1,g}(x_b)\right]. \quad (56)$$

Here, on the left hand side, the right hand side of the Marshak boundary condition can be recognized. Therefore, Eqs. (47) and (48) can be replaced in Eq. (55), and (56), leading to

$$\begin{aligned}&-\frac{1}{2}F_{0,g}(x_b) + \frac{3}{8}F_{1,g}(x_b) - D_{0,g}\frac{\partial}{\partial x}F_{0,g}(x_b) = \\ &= \tau(x_b)\left[-\frac{1}{2}F_{0,g}(x_b) + \frac{3}{8}F_{1,g}(x_b) + D_{0,g}\frac{\partial}{\partial x}F_{0,g}(x_b)\right]\end{aligned} \quad (57)$$

$$\begin{aligned}&\frac{1}{8}F_{0,g}(x_b) - \frac{7}{8}F_{1,g}(x_b) - D_{1,g}\frac{\partial}{\partial x}F_{1,g}(x_b) = \\ &= \tau(x_b)\left[\frac{1}{8}F_{0,g}(x_b) - \frac{7}{8}F_{1,g}(x_b) + D_{1,g}\frac{\partial}{\partial x}F_{1,g}(x_b)\right].\end{aligned} \quad (58)$$

From Eqs. (57) and (58), the vacuum boundary condition can be obtained inserting $\tau(x_b) = 0$. Finally, generalizing the equations to 3D and using the structure of Eq. (41) leads to

$$D_{0,g}\nabla F_{0,g}(\vec{r}) = -\frac{1}{8}\left[4F_{0,g}(\vec{r}) - 3F_{1,g}(\vec{r})\right], \forall x_b \in \partial\Gamma^V \quad (59)$$

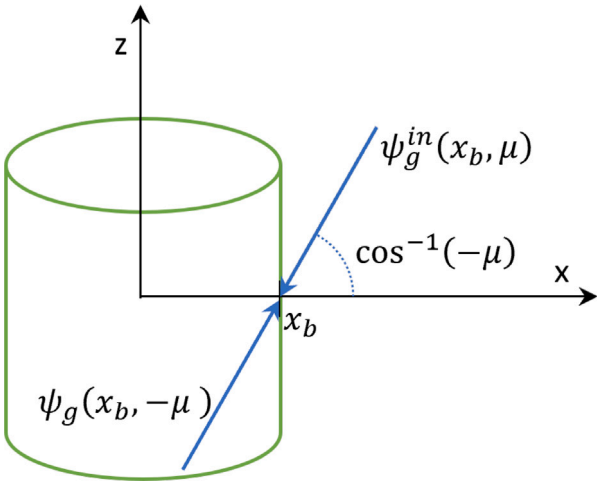

Fig. 3. Representation of the reflective boundary condition.

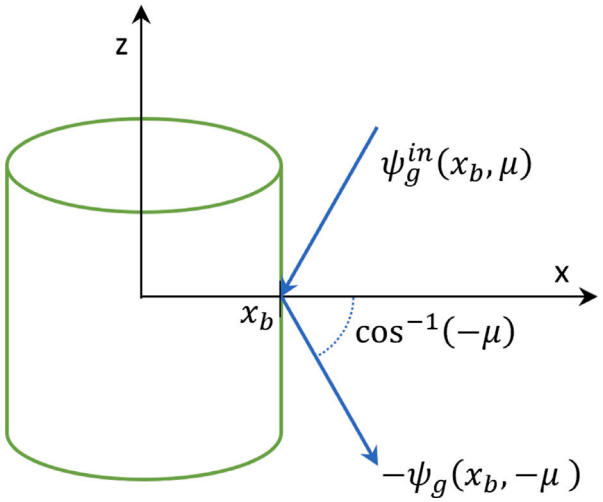

Fig. 4. Representation of the zero-flux boundary condition.

$$D_{1,g}\nabla F_{1,g}(\vec{r}) = -\frac{1}{8}\left[-F_{0,g}(\vec{r}) + 7F_{1,g}(\vec{r})\right], \forall x_b \in \partial\Gamma^V. \tag{60}$$

The reflective boundary condition, represented in Fig. 3, can be obtained with $\tau(x_b) = 1$. Therefore, the equations for 3D can be written as

$$D_{0,g}\nabla F_{0,g}(\vec{r}) = 0, \forall \vec{r} \in \partial\Gamma^R \tag{61}$$

$$D_{1,g}\nabla F_{1,g}(\vec{r}) = 0, \forall \vec{r} \in \partial\Gamma^R. \tag{62}$$

Hence, using the notation of Eq. (41), the reflective boundary condition can be expressed using the following coefficients

$$\frac{1}{\gamma(\vec{r})} = 1, \forall \vec{r} \in \partial\Gamma^R, \tag{63}$$

$$\beta_0(\vec{r}) = 0, \forall \vec{r} \in \partial\Gamma^R, \tag{64}$$

$$\beta_1(\vec{r}) = 0, \forall \vec{r} \in \partial\Gamma^R, \tag{65}$$

$$\alpha_0(\vec{r}) = 0, \forall \vec{r} \in \partial\Gamma^R, \tag{66}$$

$$\alpha_1(\vec{r}) = 0, \forall \vec{r} \in \partial\Gamma^R. \tag{67}$$

The zero-flux boundary condition, depicted in Fig. 4, can be obtained including $\tau(x_b) = -1$. The obtained equations in 3D are the following

$$D_{0,g}\nabla F_{0,g}(\vec{r}) = \infty, \forall \vec{r} \in \partial\Gamma^{ZF} \tag{68}$$

$$D_{1,g}\nabla F_{1,g}(\vec{r}) = \infty, \forall \vec{r} \in \partial\Gamma^{ZF}. \tag{69}$$

Hence, using the notation of Eq. (41), for the zero-flux boundary condition, the coefficients take the following values

$$\frac{1}{\gamma(\vec{r})} = \infty, \forall \vec{r} \in \partial\Gamma^{ZF}, \tag{70}$$

$$\beta_0(\vec{r}) = 4, \forall \vec{r} \in \partial\Gamma^{ZF}, \tag{71}$$

$$\beta_1(\vec{r}) = -1, \forall \vec{r} \in \partial\Gamma^{ZF}, \tag{72}$$

$$\alpha_0(\vec{r}) = -3, \forall \vec{r} \in \partial\Gamma^{ZF}, \tag{73}$$

$$\alpha_1(\vec{r}) = 7, \forall \vec{r} \in \partial\Gamma^{ZF}. \tag{74}$$

7. The Galerkin representation of the SP_3 equations

To derive the Galerkin form of the SP_3 equations, the same approach explained in Section 4, which was used for the diffusion equation in FENNECS, described in Seubert (2020), will be used. Considering that FENNECS uses prismatic upright prism, depicted in Fig. 5, six basis, or test, functions $\varphi_i(x^e, y^e, z^e)$, where $i \in \{1, \dots, 6\}$, are necessary. The six test functions are defined as follows:

$$\varphi_1(x^e, y^e, z^e) = \frac{1}{2}(1 - z^e)x^e \tag{75}$$

$$\varphi_2(x^e, y^e, z^e) = \frac{1}{2}(1 - z^e)y^e \tag{76}$$

$$\varphi_3(x^e, y^e, z^e) = \frac{1}{2}(1 - z^e)(1 - x^e - y^e) \tag{77}$$

$$\varphi_4(x^e, y^e, z^e) = \frac{1}{2}(1 + z^e)x^e \tag{78}$$

$$\varphi_5(x^e, y^e, z^e) = \frac{1}{2}(1 + z^e)y^e \tag{79}$$

$$\varphi_6(x^e, y^e, z^e) = \frac{1}{2}(1 + z^e)(1 - x^e - y^e) \tag{80}$$

(Seubert et al., 2023). As explained in Section 4, the Galerkin representation is obtained by firstly multiplying the two derived equations, hence Eqs. (28) and (29), by the test functions. After integration over Γ^e, hence the finite element domain, the following two equations are obtained:

$$\begin{aligned}\int_{\Gamma^e}\varphi_i(\vec{r})\left\{-D^e_{0,g}\Delta + \left[\Sigma^e_{t,g} - \Sigma^e_{s,0,gg}\right]\right\}F_{0,g}(\vec{r})dV^e + \\ -\int_{\Gamma^e} 2\varphi_i(\vec{r})\left[\Sigma^e_{t,g} - \Sigma^e_{s,0,gg}\right]F_{1,g}(\vec{r})dV^e = \int_{\Gamma^e}\varphi_i(\vec{r})\tilde{S}_{0,g}(\vec{r})dV^e\end{aligned} \tag{81}$$

$$\begin{aligned}-\int_{\Gamma^e}\frac{2}{3}\varphi_i(\vec{r})\left[\Sigma^e_{t,g} - \Sigma^e_{s,0,gg}\right]F_{0,g}(\vec{r})dV^e + \\ +\int_{\Gamma^e}\varphi_i(\vec{r})\left\{D^e_{1,g}\Delta + \frac{4}{3}\left[\Sigma^e_{t,g} - \Sigma^e_{s,0,gg}\right] + \frac{5}{3}\left[\Sigma^e_{t,g} - \Sigma^e_{s,2,gg}\right]\right\}F_{1,g}(\vec{r})dV^e = \\ = -\int_{\Gamma^e}\varphi_i(\vec{r})\frac{2}{3}\tilde{S}_{0,g}(\vec{r})dV^e.\end{aligned} \tag{82}$$

After a closer look to the terms $\int_{\Gamma^e}\varphi_i(\vec{r})D^e_{k,g}\Delta F_{k,g}(\vec{r})dV^e$, with $k = 0, 1$, it can be observed that these can be obtained by applying the product

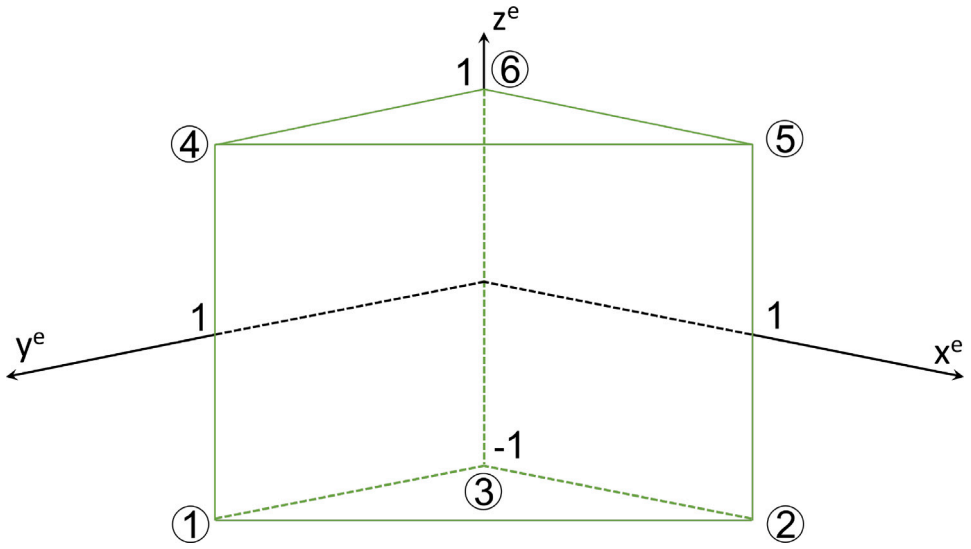

Fig. 5. Local coordinate system of the upright prismatic finite element used in FENNECS, composed by the axes x^e, y^e, and z^e.

rule of differentiation on $D^e_{k,g}\nabla\left[\varphi_i(\vec{r})\nabla F_{k,g}(\vec{r})\right]$, explained for example in Berresford and Rockett (2012), hence

$$\int_{\Gamma^e} D^e_{k,g}\nabla\left[\varphi_i(\vec{r})\nabla F_{k,g}(\vec{r})\right]dV^e = \int_{\Gamma^e} D^e_{k,g}\nabla\varphi_i(\vec{r})\nabla F_{k,g}(\vec{r})dV^e + \\ + \int_{\Gamma^e} D^e_{k,g}\varphi_i(\vec{r})\Delta F_{k,g}(\vec{r})dV^e, k = 0,1. \tag{83}$$

Here, on the left hand side, the Gauss theorem, described for example in Tang (2007), can be applied:

$$\int_{\Gamma^e} D^e_{k,g}\varphi_i(\vec{r})\Delta F_{k,g}(\vec{r})dV^e = -\int_{\Gamma^e} D^e_{k,g}\nabla\varphi_i(\vec{r})\nabla F_{k,g}(\vec{r})dV^e + \\ + \int_{\partial\Gamma^e} D^e_{k,g}\varphi_i(\vec{r})\nabla F_{k,g}(\vec{r})dA^e, k = 0,1. \tag{84}$$

Eq. (84) can now be inserted in Eqs. (81) and (82) leading to

$$\int_{\Gamma^e}\left\{D^e_{0,g}\nabla\varphi_i(\vec{r})\nabla + \left[\Sigma^e_{t,g} - \Sigma^e_{s,0,gg}\right]\varphi_i(\vec{r})\right\}F_{0,g}(\vec{r})dV^e + \\ -\int_{\Gamma^e} 2\varphi_i(\vec{r})\left[\Sigma^e_{t,g} - \Sigma^e_{s,0,gg}\right]F_{1,g}(\vec{r})dV^e = \int_{\Gamma^e}\varphi_i(\vec{r})\tilde{S}_{0,g}(\vec{r})dV^e + \\ + \int_{\partial\Gamma^e} D^e_{0,g}\varphi_i(\vec{r})\nabla F_{0,g}(\vec{r})dA^e, \forall\vec{r}\in e \tag{85}$$

$$-\int_{\Gamma^e}\frac{2}{3}\varphi_i(\vec{r})\left[\Sigma^e_{t,g} - \Sigma^e_{s,0,gg}\right]F_{0,g}(\vec{r})dV^e + \\ + \int_{\Gamma^e}\left\{D^e_{1,g}\nabla\varphi_i(\vec{r})\nabla + \frac{4}{3}\left[\Sigma^e_{t,g} - \Sigma^e_{s,0,gg}\right]\varphi_i(\vec{r}) + \right. \\ \left. + \frac{5}{3}\left[\Sigma^e_{t,g} - \Sigma^e_{s,2,gg}\right]\varphi_i(\vec{r})\right\}F_{1,g}(\vec{r})dV^e = \\ = -\int_{\Gamma^e}\frac{2}{3}\varphi_i(\vec{r})\tilde{S}_{0,g}(\vec{r})dV^e + \int_{\partial\Gamma^e} D^e_{1,g}\varphi_i(\vec{r})\nabla F_{1,g}(\vec{r})dA^e, \forall\vec{r}\in e. \tag{86}$$

Since in FENNECS, the eigenvalue problem is solved, no external neutron source can be present. Therefore, $S_{ex,0,g}(\vec{r}) = 0$ and the neutron source can be written as

$$\int_{\Gamma^e}\tilde{S}_{0,g}(\vec{r})\varphi_i(\vec{r})dV^e = \int_{\Gamma^e}\varphi_i(\vec{r})\left\{\sum_{g'=1,g'\neq g}^{G}\Sigma^e_{s,0,g'g}\left[F_{0,g'}(\vec{r}) - 2F_{1,g'}(\vec{r})\right] + \right. \\ \left. + \frac{\chi^e_g}{k_{eff}}\sum_{g'=1}^{G}\bar{\nu}^e_{g'}\Sigma^e_{f,g'}\left[F_{0,g'}(\vec{r}) - 2F_{1,g'}(\vec{r})\right]\right\}dV^e, \forall\vec{r}\in e. \tag{87}$$

The next step consists in expanding the neutron flux distributions in terms of the test functions, as given by Eq. (1), hence

$$F_{k,g}(\vec{r}) = \sum_{j=1}^{6}\varphi_j(\vec{r})f^e_{k,g,j}, \forall\vec{r}\in e, k = 0,1. \tag{88}$$

where $f^e_{k,g,j}$ are the expansions coefficients. The flux expansions can now be inserted, leading to the weak form of the equations, hence

$$\sum_{j=1}^{6} f^e_{0,g,j}\int_{\Gamma^e}\left\{D^e_{0,g}\nabla\varphi_i(\vec{r})\nabla\varphi_j(\vec{r}) + \left[\Sigma^e_{t,g} - \Sigma^e_{s,0,gg}\right]\varphi_i(\vec{r})\varphi_j(\vec{r})\right\}dV^e + \\ -\sum_{j=1}^{6} f^e_{1,g,j}\int_{\Gamma^e} 2\varphi_i(\vec{r})\varphi_j(\vec{r})\left[\Sigma^e_{t,g} - \Sigma^e_{s,0,gg}\right])dV^e = \int_{\Gamma^e}\varphi_i(\vec{r})\tilde{S}_{0,g}(\vec{r})dV^e + \\ + \sum_{j=1}^{6} f^e_{0,g,j}D^e_{0,g}\sum_{\eta=1}^{5}\int_{\partial\Gamma^e}\varphi_i(\vec{r})\nabla\varphi_j(\vec{r})dA^{e,\eta}, \forall\vec{r}\in e \tag{89}$$

$$-\sum_{j=1}^{6} f^e_{0,g,j}\int_{\Gamma^e}\frac{2}{3}\varphi_i(\vec{r})\varphi_j(\vec{r})\left[\Sigma^e_{t,g} - \Sigma^e_{s,0,gg}\right]dV^e + \\ + \sum_{j=1}^{6} f^e_{1,g,j}\int_{\Gamma^e}\left\{D^e_{1,g}\nabla\varphi_i(\vec{r})\nabla\varphi_j(\vec{r}) + \right. \\ \left. + \frac{4}{3}\left[\Sigma^e_{t,g} - \Sigma^e_{s,0,gg}\right]\varphi_i(\vec{r})\varphi_j(\vec{r}) + \frac{5}{3}\left[\Sigma^e_{t,g} - \Sigma^e_{s,2,gg}\right]\varphi_i(\vec{r})\varphi_j(\vec{r})\right\}dV^e = \\ = -\int_{\Gamma^e}\frac{2}{3}\varphi_i(\vec{r})\tilde{S}_{0,g}(\vec{r})dV^e + \\ + \sum_{j=1}^{6} f^e_{1,g,j}D^e_{1,g}\sum_{\eta=1}^{5}\int_{\partial\Gamma^e}\varphi_i(\vec{r})\nabla\varphi_j(\vec{r})dA^{e,\eta}, \forall\vec{r}\in e \tag{90}$$

with

$$\int_{\Gamma^e}\tilde{S}_{0,g}(\vec{r})\varphi_i(\vec{r})dV^e = \\ = \sum_{j=1}^{6}\int_{\Gamma^e}\varphi_i(\vec{r})\varphi_j(\vec{r})\left\{\sum_{g'=1,g'\neq g}^{G}\Sigma^e_{s,0,g'g}\left[f^e_{0,g',j} - 2f^e_{1,g',j}\right] + \right. \\ \left. + \frac{\chi^e_g}{k_{eff}}\sum_{g'=1}^{G}\bar{\nu}^e_{g'}\Sigma^e_{f,g'}\left[f^e_{0,g',j} - 2f^e_{1,g',j}\right]\right\}dV^e, \forall\vec{r}\in e. \tag{91}$$

Table 1
Values of the boundary conditions coefficients.

	$\frac{1}{\gamma^{e,\eta}}$	$\beta_0^{e,\eta}$	$\beta_1^{e,\eta}$	$\alpha_0^{e,\eta}$	$\alpha_1^{e,\eta}$
Interface boundary condition, $\forall \vec{r} \in \partial\Gamma^I$	0	0	0	0	0
Vacuum boundary condition, $\forall \vec{r} \in \partial\Gamma^V$	$\frac{1}{8}$	4	−1	−3	7
Reflective boundary condition, $\forall \vec{r} \in \partial\Gamma^R$	1	0	0	0	0
Zero flux boundary condition, $\forall \vec{r} \in \partial\Gamma^{ZF}$	∞	4	−1	−3	7

Here, the integral over the surface area of the finite element, hence dA, was split into five integrals, one for each face of the prismatic finite element. Each face of the element is addressed with η.

Now, it arises the necessity to evaluate the last term of Eqs. (89) and (90). The same term is actually obtained by transforming Eq. (41) in the Galerkin form, which consists in performing the multiplication by the test functions, integrating over the surface area and expanding the flux terms. After these steps, Eq. (41) can be written as

$$\begin{aligned} & f^e_{k,g,j} D^e_{k,g} \sum_{\eta=1}^{5} \int_{\partial\Gamma^{e,\eta}} \varphi_i(\vec{r}) \nabla \varphi_j(\vec{r}) dA^{e,\eta} = \\ & = \sum_{\eta=1}^{5} \left[-\frac{1}{\gamma^{e,\eta}} \right] \left[\beta_k^{e,\eta} f^e_{0,g,j} + \alpha_k^{e,\eta} f^e_{1,g,j} \right] \int_{\partial\Gamma^{e,\eta}} \varphi_i(\vec{r}) \varphi_j(\vec{r}) dA^{e,\eta}, \end{aligned} \tag{92}$$

$k = 0, 1, \forall \vec{r} \in \partial\Gamma^e$.

Finally, the general formulation for the boundary conditions, hence Eq. (92), can be inserted in the SP_3 equations. To express the SP_3 equations to implement in FENNECS, the matrix- vector notation will be used. The vectors have $j = 6$ elements. The SP_3 equations, including the source term, can be written as

$$\begin{aligned} & \vec{f}^e_{0,g} \left\{ D^e_{0,g} B^e + \left[\Sigma^e_{t,g} - \Sigma^e_{s,0,gg} \right] C^e - H^e \left[-\sum_{\eta=1}^{5} \frac{\beta_0^{e,\eta}}{\gamma^{e,\eta}} \right] \right\} = \\ & = C^e \left\{ \sum_{g'=1,g'\neq g}^{G} \Sigma^e_{s,0,g'g} \left[\vec{f}^e_{0,g'} - 2\vec{f}^e_{1,g'} \right] + \right. \\ & \left. + \frac{\chi^e_g}{k_{eff}} \sum_{g'=1}^{G} \bar{\nu}^e_{g'} \Sigma^e_{f,g'} \left[\vec{f}^e_{0,g'} - 2\vec{f}^e_{1,g'} \right] \right\} + \\ & + \vec{f}^e_{1,g} \left\{ 2 \left[\Sigma^e_{t,g} - \Sigma^e_{s,0,gg} \right] C^e + H^e \left[-\sum_{\eta=1}^{5} \frac{\alpha_0^{e,\eta}}{\gamma^{e,\eta}} \right] \right\} \end{aligned} \tag{93}$$

$$\begin{aligned} & \vec{f}^e_{1,g} \left\{ D^e_{1,g} B^e + \left[\frac{4}{3} \left(\Sigma^e_{t,g} - \Sigma^e_{s,0,gg} \right) + \frac{5}{3} \left(\Sigma^e_{t,g} - \Sigma^e_{s,2,gg} \right) \right] C^e + \right. \\ & \left. + H^e \left[-\sum_{\eta=1}^{5} \frac{\alpha_1^{e,\eta}}{\gamma^{e,\eta}} \right] \right\} = -\frac{2}{3} C^e \left\{ \sum_{g'=1,g'\neq g}^{G} \Sigma^e_{s,0,g'g} \left[\vec{f}^e_{0,g'} - 2\vec{f}^e_{1,g'} \right] + \right. \\ & \left. + \frac{\chi^e_g}{k_{eff}} \sum_{g'=1}^{G} \bar{\nu}^e_{g'} \Sigma^e_{f,g'} \left[\vec{f}^e_{0,g'} - 2\vec{f}^e_{1,g'} \right] \right\} + \\ & + \vec{f}^e_{0,g} \left\{ \frac{2}{3} \left[\Sigma^e_{t,g} - \Sigma^e_{s,0,gg} \right] C^e + H^e \left[-\sum_{\eta=1}^{5} \frac{\beta_0^{e,\eta}}{\gamma^{e,\eta}} \right] \right\}. \end{aligned} \tag{94}$$

The matrices B, C, and H, which have a size of 6 by 6, are obtained by evaluating the following integrals:

$$B^e = \int_{\Gamma^e} \nabla \vec{\varphi}^T(\vec{r}) \nabla \vec{\varphi}(\vec{r}) dV^e, \forall \vec{r} \in e \tag{95}$$

$$C^e = \int_{\Gamma^e} \vec{\varphi}^T(\vec{r}) \vec{\varphi}(\vec{r}) dV^e, \forall \vec{r} \in e \tag{96}$$

$$H^e = \sum_{\eta=1}^{5} \int_{\partial\Gamma^{e,\eta}} \vec{\varphi}(\vec{r}) \vec{\varphi}(\vec{r}) dA^{e,\eta}, k = 0, 1, \forall \vec{r} \in \partial\Gamma^e. \tag{97}$$

Here, the upper script T indicates the transposed vector. For the coefficients $\alpha^{e,\eta}$, $\beta_k^{e,\eta}$, and $\gamma_k^{e,\eta}$, since each of them correspond to a prisms face, their value must be inserted depending on the boundary condition. These values can be found in Table 1.

8. Algorithm

As stated at the beginning of this paper, FENNECS is a steady state and – for the diffusion approximation only – time-dependent neutron kinetics code. The solution procedure adopts the well-established scheme of nested inner–outer iterations. The outer iteration is dedicated to solve the eigenvalue problem (by either power or inverse vector iteration by Wielandt), based on the current iterate of the fission source distribution which, in turn, depends on the current iterates of the group-wise neutron flux distributions. The inner iteration solves the within-group problems for each energy group taking into account group-to-group scattering. The finite element method applied in FENNECS is used for the spatial discretization. As described by Eqs. (93) and (94), the within-group problem can be cast into a system of linear equations for each energy group. This system of equations and its solution method are explained in the following.

Since FENNECS is a finite element code, as explained in Section 4, it is necessary to formulate the equations with a global system matrix, a vector of unknowns and the so-called load vector, located on the right hand side of the equation. Therefore, firstly, we define the system for each single element, so Eq. (93), and (94) are written as two systems of linear equations, hence

$$L^e_{k,g} \vec{f}^e_{k,g} = \vec{b}^e_{k,g}, k = 0, 1. \tag{98}$$

Here, $L^e_{k,g}$, the system matrix of equation k and energy group g of the element e, which contains the terms present in the curly bracket on the left hand side and it has a size of 6 by 6, since in FENNECS the prismatic elements have 6 nodes. $\vec{b}^e_{k,g}$, load vector of the element e, includes all the right hand side of the equation. In particular, this term can be separated into $\vec{b}^e_{k,g,source}$, which contains the contribution due to scattering and fission, and into the last line of the equation, which depends on the term containing the fluxes. The K systems of equations, where K is the number of elements in the geometry, are assembled in a single global system of equations, hence

$$L_{k,g} \vec{f}_{k,g} = \vec{b}_{k,g}, k = 0, 1. \tag{99}$$

In this section, it will be explained in a very simplified way how the systems of equations are solved. The main steps, which will be explained hereafter, are the following:

- Initialization
- Outer convergence loop
  - Inner convergence loop for the first equation ($k = 0$)
  - Inner convergence loop for the second equation ($k = 1$).

The first step consists in the initialization of the global components of the system of equations, as explained in algorithm 1. As next step, the outer convergence loop, described in algorithm 2 is entered. This last algorithm is repeated until convergence is achieved. Within this loop, firstly, the matrices $L_{0,g}$ and $L_{1,g}$ are assembled, based on algorithm 3. Afterwards, the right hand side is defined, firstly by adding the neutron fission and scattering sources, as in algorithm 4, and then the last line of Eq. (93), and (94), as in algorithm 5. The next step is the calculation of $\vec{f}_{0,g}$ and $\vec{f}_{1,g}$. These are obtained based on the system matrices and load vectors, when the inner convergence loop, based on the preconditioned conjugate method, called here PConjGrad achieves the convergence. Due to the presence of two equations, this procedure is performed twice. Then the scalar flux and effective multiplication factors are obtained. Finally, in the outer loop, based on the power method, the convergence is checked.

Algorithm 1 Initialization

for $g = 1, G, 1$ **do**
  for $k = 0, 1, 1$ **do**
    Set the entries of, $L_{k,g}$, $f_{k,g}$ and $\vec{b}_{k,g}$ to 0.
  end for
end for

Algorithm 2 Outer convergence loop

while convergence=FALSE **do**
  for $g = 1, G, 1$ **do**
    AssembleSysMatrix($L_{0,g}$)
    AssembleSysMatrix($L_{1,g}$)
  end for
  for $g = 1, G, 1$ **do**
    AssembleSourceTerm($\vec{b}_{0,g}$)
    AddFluxTerm($\vec{b}_{0,g}$, $\vec{f}_{1,g}$)
    AssembleSourceTerm($\vec{b}_{1,g}$)
    AddFluxTerm($\vec{b}_{1,g}$, $\vec{f}_{0,g}$)
  end for
  for $g = 1, G, 1$ **do**
    PConjGrad($L_{0,g}$, $\vec{b}_{0,g}$, $\vec{f}_{0,g}$)
    PConjGrad($L_{1,g}$, $\vec{b}_{1,g}$, $\vec{f}_{1,g}$)
  end for
  for $g = 1, G, 1$ **do**
    $\vec{\phi}_{0,g} = \vec{f}_{0,g} - 2\vec{f}_{1,g}$
  end for
  Calculation of k_{eff}
  Convergence check fission source
end while

Algorithm 3 AssembleSysMatrix

for $e = 1, K, 1$ **do**
  Calculate B^e, C^e, and H^e
  if $L_{0,g}$ is given as argument **then**
    Calculate $L^e_{0,g}$
    Insert $L^e_{0,g}$ in $L_{0,g}$
  end if
  if $L_{1,g}$ is given as argument **then**
    Calculate $L^e_{1,g}$
    Insert $L^e_{1,g}$ in $L_{1,g}$
  end if
end for

Algorithm 4 AssembleSourceTerm

if $\vec{b}_{0,g}$ is given as argument **then**
  $b_{0,g}$=0
end if
if $\vec{b}_{1,g}$ is given as argument **then**
  $b_{1,g}$=0
end if
for $e = 1, K, 1$ **do**
  Calculate C^e,
  Calculate the fission and scattering sources and insert them in $\vec{b}^e_{0,g}$
  if $\vec{b}_{0,g}$ is given as argument **then**
    Insert the fission and scattering source terms $\vec{b}^e_{0,g}$
    Add $\vec{b}^e_{0,g}$ to $\vec{b}_{0,g}$
  end if
  if $\vec{b}_{1,g}$ is given as argument **then**
    Insert the fission and scattering source terms $\vec{b}^e_{1,g}$
    $\vec{b}^e_{1,g} = -\frac{2}{3}\vec{b}^e_{1,g}$
    Add $\vec{b}^e_{1,g}$ to $\vec{b}_{1,g}$
  end if
end for

Algorithm 5 AddFluxTerm

for $e = 1, K, 1$ **do**
  Calculate C^e, and H^e
  if $\vec{b}_{0,g}$ is given as argument **then**
    $b^e_{0,g}$=0
    Calculate the last term of the right handy side, which is multiplied by $f^e_{1,g}$ and store it in $b^e_{0,g}$
    Add $\vec{b}^e_{0,g}$ to $\vec{b}_{0,g}$
  end if
  if $\vec{b}_{1,g}$ is given as argument **then**
    $b^e_{1,g}$=0
    Calculate the last term of the right handy side, which is multiplied by $f^e_{0,g}$ and store it in $b^e_{1,g}$
    Add $\vec{b}^e_{1,g}$ to $\vec{b}_{1,g}$
  end if
end for

9. Conclusion

To allow FENNECS to perform the safety assessment of (v)SMR and MMR, the code was extended by an SP_3 solver. In order to equip the FENNECS code with a steady state SP_3 solver, firstly, starting from the one dimensional transport equation, the SP_3 approximation of the neutron transport equation was derived, including the boundary conditions. The derived two equations were cast into the Galerkin form. This step was necessary since the FENNECS code is based on the finite elements formalism. Finally, an overview was given regarding how the algorithms are structured in the SP_3 solver of FENNECS.

As next step, the implemented new solver will be applied on simple core configurations, in order to prove its functionality.

CRediT authorship contribution statement

Silvia lo Muzio: Methodology, Software, Formal analysis, Investigation, Data curation, Writing – original draft, Writing – review & editing, Visualization. **Armin Seubert:** Conceptualization, Funding acquisition, Project administration, Supervision, Resources, Writing – review & editing.

Declaration of competing interest

The authors declare that they have no known competing financial interests or personal relationships that could have appeared to influence the work reported in this paper.

Data availability

Data will be made available on request.

Acknowledgement

This work was supported by the German Federal Ministry for the Environment, Nature Conservation, Nuclear Safety and Consumer Protection.

References

Avvakumov, A.V., Strizhov, V.F., Vabishchevich, P.N., Vasilev, A.O., 2019. Numerical modeling of neutron transport in SP3 approximation by finite element method. CoRR arXiv:1903.11502v1 [cs.CE]. URL http://arxiv.org/pdf/1903.11502v1.

Babcsány, B., Pós, I., Böröczki, Z.I., Kis, D.P., 2022. Hybrid finite-element-based numerical solution of the SP3 equations – SP3 solution of two- and three-dimensional VVER reactor problems. Ann. Nucl. Energy 173, 109117. http://dx.doi.org/10.1016/j.anucene.2022.109117.

Bal, G., Ryzhik, L., 2000. Diffusion approximation of radiative transfer problems with interfaces. SIAM J. Appl. Math. 60 (6), 1887–1912. http://dx.doi.org/10.1137/S0036139999352080.

Beckert, C., Grundmann, U., 2007. A Nodal expansion method for solving the multigroup sp3 equations in the reactor code DYN3D. In: Joint International Topical Meeting on Mathematics & Computation and Supercomputing in Nuclear Applications (M&C + SNA 2007).

Bell, G.I., Glasstone, S., 1970. In: Van Nostrand Reinhold Company (Ed.), Nuclear Reactor Theory. Litton Educational Publishing, Inc.

Berresford, G.C., Rockett, A.M., 2012. Applied Calculus. Cengage Learning.

Bousquet, J., Seubert, A., Henry, R., 2020. New finite element neutron kinetics coupled code system FENNECS/ATHLET for safety assessment of (very) small and micro reactors. J. Phys.: Conf. Ser. http://dx.doi.org/10.1088/1742-6596/1689/1/012008.

Burrone, M., 2018. Study of Eigenvalue Formulations in the PN Approximation of the Neutron Transport Equation (Master's thesis). Politecnico di Torino, Torino.

Cao, L., Wu, H., 2021. Deterministic Numerical Methods for Unstructured-Mesh Neutron Transport Calculation. In: Woodhead Publishing Series in Energy, Elsevier Science & Technology, San Diego.

Cox, A.M.G., Harris, S.C., Horton, E.L., Kyprianou, A.E., 2019. Multi-species neutron transport equation. J. Stat. Phys. 176 (2), 425–455. http://dx.doi.org/10.1007/s10955-019-02307-2.

Devan, K., Bachchan, A., 2021. Chapter 4 - Homogeneous reactor and neutron diffusion equation. In: Mohanakrishnan, P., Singh, O.P., Umasankari, K. (Eds.), Physics of Nuclear Reactors. Academic Press an imprint of Elsevier, London, pp. 193–262. http://dx.doi.org/10.1016/B978-0-12-822441-0.00004-2, URL https://www.sciencedirect.com/science/article/pii/B9780128224410000042.

Downar, T., Xu, Y., Seker, V., 2012. Theory Manual - PARCS v3.0 U.S. NRC Core Neutronics Simulator. Department of Nuclear Engineering and Radiological Sciences, University of Michigan.

Dürigen, S., 2013. Neutron Transport in Hexagonal Reactor Cores Modeled by Trigonal-Geometry Diffusion and Simplified P3 Nodal Methods (Ph.D. thesis). Karlsruhe Institute of Technology, Karlsruhe, URL https://inis.iaea.org/collection/NCLCollectionStore/_Public/48/022/48022303.pdf.

Gelbard, E.M., 1960. Application of spherical harmonics method to reactor problems. In: Bettis Technical Review.

Ghasabyan, L., 2013. Use of Serpent Monte-Carlo code for development of 3D full-core models of Gen-IV fast-spectrum reactors and preparation of group constants for transient analyses with TRACE-PARCS coupled system (Master's thesis). KTH Engineering Sciences, KTH, Stockholm.

Hamilton, S.P., Evans, T.M., 2015. Efficient solution of the simplified P3 equations. J. Comput. Phys. (284).

Harrison, R.L., 2010. Introduction to Monte Carlo simulation. In: AIP Conference Proceedings 1204, 17.

Hébert, A., 2012. A User Guide For TRIVAC Version4. Institut de génie nucléaire, Département de génie mécanique, École Polytechnique de Montréal.

Hore-Lacy, I., 2010. NUCLEAR POWER. In: Hore-Lacy, I. (Ed.), Nuclear Energy in the 21st Century. Elsevier Science, Burlington, pp. 37–53. http://dx.doi.org/10.1016/B978-012373622-2/50006-4.

Kaplan, W., 1992. Advanced Calculus, fourth ed. pp. 508–512, URL https://fac.ksu.edu.sa/sites/default/files/fourier-legendre_series_-_from_wolfram_mathworld.pdf.

Lewis, E.E., Miller, W.F., 1984. Computational Methods of Neutron Transport. Wiley, New York.

Marguet, S., 2018. the Physics of Nuclear Reactors. Springer International Publishing, http://dx.doi.org/10.1007/978-3-319-59560-3.

Mohanakrishnan, P., Singh, O.P., Umasankari, K. (Eds.), 2021. Physics of nuclear reactors. Academic Press an imprint of Elsevier, London.

Phillips, G.M., 2006. Interpolation and Approximation By Polynomials. In: CMS Books in Mathematics, Springer New York.

Powers, D.L., 2007. Boundary Value Problems and Partial Differential Equations, fifith ed. Academic Press, Amsterdam and Heidelberg.

Seubert, A., 2020. A 3-D Finite element few-group diffusion code and its application to generation IV reactor concepts. In: Proceedings of PHYSOR 2020.

Seubert, A., Bousquet, J., Henry, R., 2021. Recent advances of the FENNECS neutronics Code for safety assessment Of (v)smr, generation Iv and other innovative Concepts. In: the International Conference on Mathematics and Computational Methods Applied to Nuclear Science and Engineering.

Seubert, A., Henry, R., lo Muzio, S., 2023. Finite Elements NEutroniCS: Vol. 2: Models & Methods Manual. Gesellschaft für Anlagen- und Reaktorsicherheit (GRS) gGmbH.

Stacey, W.M., 2007. Nuclear Reactor Physics, Second ed., completely rev. and enlarged. WILEY-VCH, Weinheim, http://dx.doi.org/10.1002/978-3-527-61104-1, URL http://site.ebrary.com/lib/alltitles/docDetail.action?docID=10304032.

Tang, K.T., 2007. Vector Analysis, Ordinary Differential Equations and Laplace Transforms. In: Mathematical methods for engineers and scientists / K. T. Tang, vol. 2, Springer, Berlin.

Vidal Ferràndiz, A., Carreño, A., Fontenla, Y., Ginestar, D., Verdú, G., 2023. FEMFFUSION A finite element code to model nuclear reactors: User's Manual. Universitat Politècnica de València.

Willert, J., Kelley, C.T., Knoll, D.A., Park, H., 2013. Hybrid deterministic/Monte Carlo neutronics. SIAM J. Sci. Comput. 35 (5), 62–83. http://dx.doi.org/10.1137/120880021.

Zienkiewicz, O.C., Taylor, R.L., Zhu, J.Z., 2005a. Generalization of the finite element concepts. Galerkin-weighted residual and variational approaches. In: Finite Element Method - Its Basis and Fundamentals. Elsevier, pp. 54–102. http://dx.doi.org/10.1016/B978-075066431-8.50171-5.

Zienkiewicz, O.C., Taylor, R.L., Zhu, J.Z., 2005b. The standard discrete system and origins of the finite element method. In: Finite Element Method - Its Basis and Fundamentals. Elsevier, pp. 1–18. http://dx.doi.org/10.1016/B978-075066431-8.50169-7.

Zienkiewicz, O.C., Taylor, R.L., Zhu, J.Z., 2013. The standard discrete system and origins of the finite element method. In: the Finite Element Method: Its Basis and Fundamentals. Elsevier, pp. 1–20. http://dx.doi.org/10.1016/B978-1-85617-633-0.00001-0.

Chapter 4

Verification

This chapter presents a collection of all the test cases that were used to verify the newly implemented SP_3 solver in FENNECS. Figure 4.1 explains more in detail the approach used for the validation of the solver, including the test cases that were used. The methodology developed is based on two approaches: the source of the macroscopic cross section libraries involved in the simulation and the type of code used for the comparison with the FENNECS SP_3 solver.

Regarding the first approach, firstly, the verification was performed, based on test cases with cross section libraries, which were freely defined by the authors of the exercise. Hence, no cross section generation programs were used. Since the cross sections were defined, and not generated, errors or influences coming from the cross section generation process could be excluded. This step is essential to isolate the functionality of the FENNECS SP_3 solver. Therefore, hereby, it is proven that the SP_3 approach was correctly designed from the point of view of the mathematical model as well as the idea behind the algorithms. Additionally, it is demonstrated that these were correctly implemented in FENNECS. Test cases belonging to this category were found in the literature. Examples of test cases belonging to this group are the homogeneous and heterogeneous slabs, the 2D Cartesian planar benchmark, and the Hébert benchmark. These will be discussed in section 4.1 and more details about the last two can be found in section 4.2. Once this step was completed, the verification could be continued with test cases, where the macroscopic cross section libraries were generated using appropriate codes, like Serpent [35], ERANOS [50], or HELIOS [62]. In this step, the functionality of the new solver was proven using realistic cross section libraries. Hence, beyond the solver functionality, it is proven that it can be applied to realistic nuclear data. Furthermore, this stage allows to observe the effects of the methodology behind the cross section generation program on the SP_3 results. A first attempt to

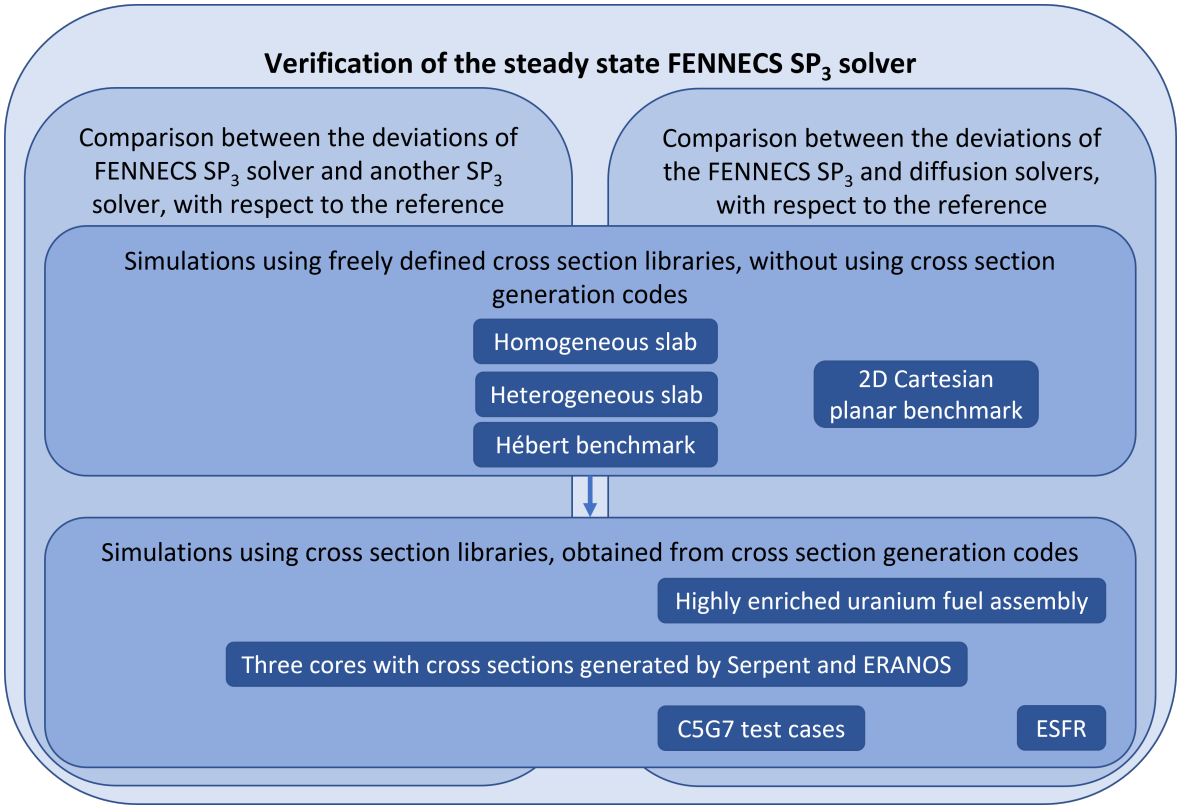

Figure 4.1: Methodology used for the verification of the FENNECS SP_3 solver and the test cases used for this purpose.

address this phenomenon was done within the test case of the three cores with cross sections generated by Serpent [35] and ERANOS [50], discussed in section 4.1. Here, the cross section libraries and the geometries could be found in the literature. In other cases, the libraries were generated within this work and the geometries were found in the literature or designed ad hoc. The advantage of freely design the geometry of the test case to analyse is that particular aspects of the solver can be addressed, like for example particular boundary conditions. This was the case for the highly enriched uranium fuel assembly, whose results are discussed in section 4.1. Here, further test cases with generated cross section libraries are mentioned, which are the C5G7 [10] test cases and the European Sodium fast reactor (ESFR) [51]. However, their detailed analysis can be found in section 4.3, and 4.4, respectively.

The second aspect of the methodology used for the verification deals with the solver used for the comparison with the new FENNECS solver. The comparison can be performed with other SP_3 solvers or with diffusion ones. To perform the evaluation, the first step was always to calculate the discrepancy for the results of the FENNECS SP_3 solver with respect to a reference. The reference results were obtained for example with Serpent [35] or the transport code ONEDANT [17]. This procedure allows to evaluate

the loss in accuracy of the results due to the use of the SP_3 approximation of the neutron transport equation. The discrepancy with respect to the reference is also calculated for results obtained with the other solver considered for the analysis. To use another SP_3 solver for the comparison allows to verify the correct functionality of the FENNECS SP_3 solver, by showing that from both SP_3 solvers similar deviations in the results are obtained. Furthermore, diffusion solvers can be used for the evaluation. On one hand, the SP_3 solver delivers more accurate results, compared to the diffusion method. On the other hand, more calculation resources are needed, compared to diffusion simulations. By comparing the discrepancy obtained by the FENNECS SP_3 solver and the one resulting from the diffusion solver, the gain in accuracy by the application of the SP_3 solver can be quantified. This evaluation allows to identify where the increased costs due to computational resources are worth with respect to an increase in the results accuracy. Since FENNECS provides also a diffusion solver, this type of evaluation was performed for all test cases presented here. On the contrary, the comparison with another SP_3 solver was done only for the homogeneous and heterogeneous slab, the Hébert benchmark and the test cases with cross sections generated by Serpent [35] as well as ERANOS [50].

To evaluate the results, various parameters were used. The effective multiplication factor was used in all test cases. In addition, in some situations, also the normalized power or neutron flux distributions were analysed. These quantities were evaluated with the help of the maximum and minimum deviations as well as the root mean squared (RMS) error. In [39], also the control rod (CR) worth was used for the analysis. Additionally, in [42], the loss in reactivity due to the leakage was considered.

4.1 The homogeneous and heterogeneous slabs, three cores with cross sections generated by Serpent and ERANOS, and the highly enriched uranium fuel assembly

Annals of Nuclear Energy 200 (2024) 110304

Contents lists available at ScienceDirect

Annals of Nuclear Energy

journal homepage: www.elsevier.com/locate/anucene

Implementation of the steady state Simplified P3 (SP3) transport solver in the finite element neutronic code FENNECS, Part 2: Verification

Silvia lo Muzio *, Armin Seubert

Gesellschaft fur Anlagen- und Reaktorsicherheit (GRS) gGmbH, Safety Research Division, Nuclear Fuel Department, Boltzmannstr. 14, D-85748 Garching, Germany

ARTICLE INFO

Keywords:
SP_3 approximation
FENNECS
Finite element method
Academic benchmarks
Cartesian benchmark
Hebert benchmark
C5G7

ABSTRACT

FENNECS, originally a diffusion code developed at GRS, was equipped with a steady state solver based on the Third Order Spherical Harmonics approximation of the transport equation (SP_3). After the theoretical derivation of the SP_3 approximation and its implementation in the code, it was necessary to perform its verification.

In this work, all test cases used for the verification of the new FENNECS SP_3 solver are included. For the verification of the solver, test cases having geometries of various sizes and complexity were chosen. The cross section libraries used were obtained with various approaches. Furthermore, the obtained results were compared with transport codes as well as other SP_3 and diffusion solvers.

1. Introduction

The Finite ElemeNt NeutroniCS (FENNECS) code was developed at Gesellschaft für Anlagen und Reaktorsicherheit gGmbH (GRS). It offers a steady state as well as a transient 3D diffusion solver, based on the Galerkin, or finite element, approach (Seubert et al., 2021; Bousquet et al., 2020). To exploit its advantageous geometrical flexibility, FENNECS was extended by a steady state solver based on the simplified Third Order Spherical Harmonics approximation of the transport equation (SP_3), in order to be able to perform safety assessments of (very) small modular reactors ((v)SMR) and micro modular rectors (MMR). These reactor systems are characterized by complex and heterogeneous geometries (Schaffrath et al., 2021).

The implementation of a new solver must be followed by its verification. On one hand, this step is essential to check its correct implementation. On the other hand, it is useful to evaluate the deviation in the results with respect to a reference code relying on a more accurate method, like for example codes based on the transport equation or Monte Carlo codes. With this regard, it is as well useful to compare these reference results with the ones from codes based also on the SP_3 approximation in order to check if the obtained deviations for the new FENNECS SP_3 solver are in the same order of magnitude, like the ones of other codes providing the same methodology. For this purpose, codes like DYN3D and TRIVAC were used. Also lower order codes were used for the comparison, because their results were also compared with the reference in order to quantify the improvement in the results given by the use of the SP_3 methodology. Here, the diffusion solver of FENNECS was used.

Following the described principle, the verification was carried out with test cases with manufactured given cross section libraries as well as with some where their generation was carried out using appropriate codes. For this last category, the libraries could be found in the literature or they were generated by the authors. The first category of samples is essential in order to look only at the functionality of the solver, since influences in the cross section generation can be excluded and the comparison is performed with codes using the same cross section libraries. However, it is difficult to find many of these examples with all necessary nuclear data. Therefore, additional geometries are modelled firstly to generate the cross section libraries and then these are used within the verification process. This approach allows also to freely choose the geometry on which to test the new solver.

The FENNECS SP_3 calculations reported in this work were performed neglecting higher order scattering between energy groups, based on the following definition of the (zeroth order) diffusion constant, given in lo Muzio and Seubert (2024):

$$D_{0,g}(x) = \frac{1}{3\left[\Sigma_{t,g}(x) - \Sigma_{s,1,gg}(x)\right]}. \tag{1}$$

As also derived in lo Muzio and Seubert (2024), the first order scattering between energy groups can be considered by defining the diffusion constant as

$$D_{0,g}(x) = \frac{1}{3\Sigma_{tr,g}(x)}. \tag{2}$$

In this work, this definition of the (zeroth order) diffusion coefficient is only used when marked explicitly. This is the case in Section 2.2.1. In all other cases, Eq. (1) is used.

* Corresponding author.
E-mail address: silvia.lo-muzio@grs.de (S. lo Muzio).

https://doi.org/10.1016/j.anucene.2023.110304
Received 4 July 2023; Received in revised form 24 October 2023; Accepted 12 December 2023
Available online 1 February 2024
0306-4549/© 2024 Elsevier Ltd. All rights reserved.

Table 1
Mono-energetic macroscopic cross sections $(1/cm)$ for the homogeneous slab for the energy group $g = 1$ (Ragab Fayez, 2016).

$\Sigma_{t,1}$	$\Sigma_{s,0,11}$	$\nu\Sigma_{f,1}$
1	0.9	0.25

Table 2
For the homogeneous slab, difference in the effective multiplication factor (pcm) between the reference, which is ONEDANT, and the ones obtained with FENNECS, and the h-p FEM analytical and numerical method from Ragab Fayez (2016).

	Diffusion solver	SP_3 solver	SP_5 solver
FENNECS	−19375	−2308	
h-p FEM analytical	−19375	−2309	−554
h-p FEM numerical	−19375	−2309	−554

2. Verification

In Section 2.1, cores with already given cross sections libraries were modelled in order to prove the correct functionality of the solver, excluding the influence of the cross section generation procedure. Geometries and related nuclear data were found in the literature. Within this category, a homogeneous and a heterogeneous slab, the Cartesian benchmark and the Hébert benchmark were reproduced. The authors of these benchmarks defined the geometry as well as the nuclear data. Hence, no cross section generation was carried out. On the contrary, for the geometries reproduced in Section 2.2, the cross sections libraries were produced with ERANOS, HELIOS or Serpent. For these test cases, the cross section generation was carried out by the authors, except for the three cores of differnt size, which can be found in Section 2.2.1.

2.1. Test cases with given cross section libraries

2.1.1. Homogeneous slab

The first test case is a homogeneous one-dimensional slab, having a thickness of 2 cm, described in Ragab Fayez (2016). It is modelled as infinite along the x- and y-axis, hence imposing reflective boundary conditions, and vacuum boundary conditions are applied in z direction, hence on the xy-plane. The related one-energy-group macroscopic cross sections can be found in Table 1. For this test case, in Ragab Fayez (2016), effective multiplications factors calculated with an analytical as well as finite element based numerical diffusion, SP_3, and SP_5 solvers are provided. This test case was chosen for three reasons. Firstly, these results allow to see whether the ones of the newly implemented SP_3 solver are similar, proving its correctness. In Ragab Fayez (2016), also a solution obtained with the multigroup transport numerical code ONEDANT (Douglas O'Dell et al., 1982), based on the discrete-ordinates approximation, is given, which is used as reference. For ONEDANT, the angular quadrature set S_{96} was used (Ragab Fayez, 2016). Therefore, secondly, it can be shown by how much the solution of the SP_3 solvers deviates from the more accurate direct transport solution. Thirdly, due to the small thickness of the slab, a strong spatial variation of the neutron flux is expected (Ragab Fayez, 2016). Therefore, finally, using the results of the diffusion solvers, the deficiencies, with respect to SP_3 solvers, for such small configurations can be shown.

Firstly, from Table 2, it can be observed that the effective multiplication factors calculated by the FENNECS solvers, the h-p FEM analytical as well as numerical SP_3 solvers are very similar. In particular, for the FENNECS SP_3 solver, the effective multiplication factor is 0.65296. This result deviates from the other SP_3 solutions considered here by less than 1 pcm. The closeness of the results of the three solvers shows that the FENNECS SP_3 solver works properly. Secondly, comparing the effective multiplication factor of the FENNECS SP_3 solver and ONEDANT, a discrepancy of −2308 pcm can be calculated, which is very high. On one hand, by using both SP_5 solvers of the h-p FEM method the discrepancy is reduced to −554 pcm, which is still high. Therefore, with the SP_5 solvers, an improvement is obtained, since it is a more accurate method, but the discrepancy remains still high due to the very small size of the geometry considered. Thirdly, on the other hand, the discrepancy in the case of the three diffusion solvers is much larger, compared to the one of the SP_3 solvers: in the case of the FENNECS diffusion solver, the discrepancy in the k_{eff} is −19375 pcm, which is unacceptable. This result shows that by using the SP_3 method, instead of the diffusion approximation, the effective multiplication factor can be improved by more than a factor of eight. Overall, it can be concluded that this result shows also that the diffusion approximation is highly inadequate to model such small geometries.

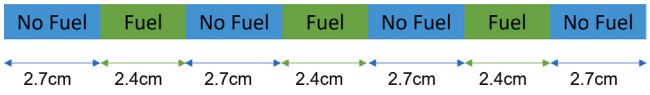

Fig. 1. Geometry of the heterogeneous slab.

Table 3
Mono-energetic macroscopic cross sections $(1/cm)$ for the heterogeneous slab for the energy group $g = 1$ (Ragab Fayez, 2016).

Material	$\Sigma_{t,1}$	$\Sigma_{s,0,11}$	$\nu\Sigma_{f,1}$
Fuel	0.416667	0.334	0.178
No fuel	0.370370	0.334	0.0

Table 4
For the heterogeneous slab, difference in the effective multiplication factor (pcm) between the reference, which is ONEDANT, and the ones obtained with FENNECS, and the numerical h-p FEM method from Ragab Fayez (2016).

	Diffusion solver	SP_3 solver	SP_5 solver
FENNECS	−3736	−1011	
h-p FEM numerical	−3736	−1011	−363

2.1.2. Heterogeneous slab

As second verification example, a heterogeneous slab is modelled, which, as the previous test case, was also taken from Ragab Fayez (2016). As depicted in Fig. 1, the 18 cm thick infinite slab is constituted by fuel and no fuel materials. Like the homogeneous slab, it was modelled as infinite in the x and y direction, where reflective boundary conditions were applied, and vacuum boundary conditions were applied along the z axis, hence on the xy plane. The cross sections can be found in Table 3. This geometry deviates from the one described in Section 2.1.1, such that it is more heterogeneous. To evaluate the effective multiplication factor, the results of the numerical program h-p FEM are used for the direct comparison with FENNECS and the solution of ONEDANT, based on the angular quadrature set S_{96}, is taken as reference (Ragab Fayez, 2016).

As it can be observed in Table 4, comparing the results of FENNECS and of the h-p FEM code, it can be observed that the same solution methods of the two programs deliver the same results. This holds for the diffusion as well as SP_3 solvers. This proves the correct implementation of the new solver and also of the diffusion approximation in FENNECS. Furthermore, using the SP_3 solver, instead of diffusion theory, reduces the error with respect to ONEDANT by more than one third. However, the SP_3 solver of FENNECS as well as of h-p FEM calculate results showing deviations, with respect to ONEDANT, in the order of 1000 pcm, hence which are very far away from the reference. This can be explained by the very small size of the geometry and by its strong heterogeneity. Due to the consideration of higher order Legendre's polynomials, an improvement can be achieved with the SP_5 approximation. However, we can see that such strong heterogeneities are a significant issue also for this method. Although, the SP_5 solver is available only for h-p FEM and not for FENNECS.

Table 5
Mono-energetic macroscopic cross sections $(1/cm)$ for the Cartesian and the Hébert benchamrk for the energy group $g = 1$ (Hébert, 2010; Dürigen, 2013).

Material	$\Sigma_{t,1}$	$\Sigma_{s,0,11}$	$\Sigma_{s,1,11}$	$\nu\Sigma_{f,1}$
Fuel	0.025	0.013	0.0	0.0155
Reflector	0.025	0.024	0.006	0.0
Absorber	0.075	0.334	0.0	0.0

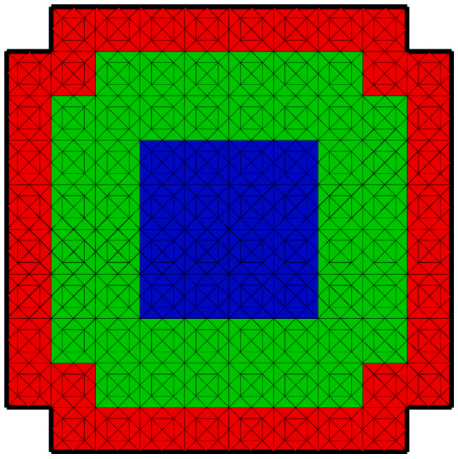

Fig. 2. Geometry of the Cartesian benchmark, constituted by a central region made of fuel (blue), surrounded by a reflector (green) and an absorber (red). The black line represents the vacuum boundary condition. In axial direction, reflective boundary conditions are imposed. The mesh used here divides each assembly in 16.

2.1.3. 2D Cartesian planar benchmark

This 2D Cartesian planar benchmark geometry is composed by squared assemblies, having a pitch of 40 cm (Hébert, 2010). It is constituted by an outer ring made of a pure absorber, which contains a ring of reflector, as depicted in Fig. 2 (Hébert, 2010). The inner part of the core is made of fuel assemblies and its total mean free path is 40 cm, hence it is equivalent to the assembly pitch (Hébert, 2010). Radially, vacuum boundary conditions are applied (Hébert, 2010). Since it is a 2D geometry, axially, reflective boundary conditions are imposed. Therefore, this benchmark presents a small geometry and strong variations between the material properties. For this reason, this is particularly suited to show the performance of the newly implemented SP_3 solver in FENNECS. Within this benchmark, the nuclear data are provided. These are mono-energetic, i.e. they have only one energy group (Hébert, 2010). In this benchmark, the macroscopic cross sections are given and their values can be found in Table 5.

As discussed in lo Muzio and Seubert (2022a), the results of the FENNECS SP_3 and diffusion solvers were compared with two SP_3 solvers of TRIVAC, which are both based on the Raviart–Thomas zeroth order solution. The first one uses analytical integration and the other numerical integration by Gauss–Legendre quadrature (Hébert, 2010). In FENNECS, the calculations were performed with various axial sizes. The discrepancies of the effective multiplication factors obtained by these solvers were evaluated with respect to the solution obtained by the TRIVAC SP_5 solver based on the Raviart–Thomas second order solution with Gauss–Legendre quadrature using a mesh with 16 radial elements per assembly. The k_{eff} obtained here, which will be used as reference, is 0.992160 and this value, including all the results of the TRIVAC calculations were taken from Hébert (2010).

Fig. 3 plots the difference between the effective multiplication factors obtained and the reference as a function of the number of radial elements per assembly, hence the mesh refinement. Firstly, as stated in lo Muzio and Seubert (2022b), it can be observed that for all the solvers considered the discrepancy with the reference decreases by using a finer mesh, hence increasing the number of radial elements

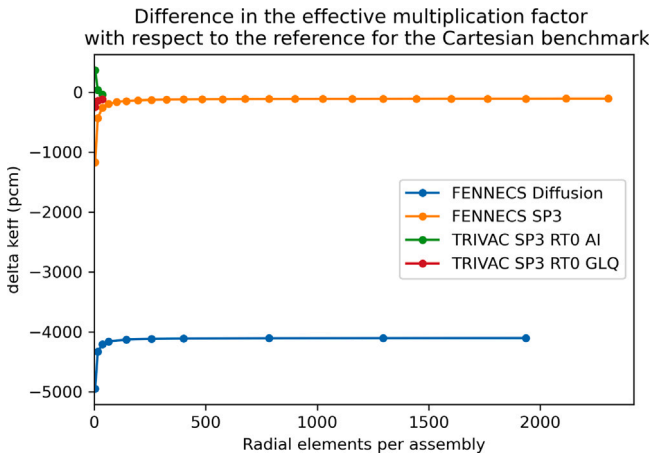

Fig. 3. For the Cartesian benchmark, difference between the reference and the effective multiplication factors obtained with the FENNECS diffusion solver (blue), FENNECS SP_3 solver (orange), TRIVAC SP_3 solver with Raviart–Thomas with zeroth order solution (RT0) and analytical integration (AI) (green), and TRIVAC SP_3 solver with Raviart–Thomas with zeroth order solution (RT0) and Gauss–Legendre quadrature (GLQ) (red), versus the number of radial elements per assembly used for the mesh.

per assembly. In particular, for the FENNECS SP_3 solver, the first mesh refinement step reduces the error, with respect to the reference, to less than a half, whereas for the diffusion solver the improvement is only weak. Starting from 2116 radial elements per assembly, for the FENNECS SP_3 solver, no changes can be observed in the effective multiplication factor if the mesh size is further reduced. In this case, the discrepancy is only 106 pcm. Secondly, from the comparison of the three SP_3 solvers involved in this work, it can be observed that for the same mesh, the TRIVAC solvers deliver a k_{eff} closer to the reference. Finally, the results of the two FENNECS solvers can be compared. The results of the diffusion solver are very far away from the reference, because for both meshes considered, the difference with the reference is above 4000 pcm. This shows that the diffusion approximation is not suited to model such small and heterogeneous cores. In this cases, the FENNECS SP_3 solver should be applied, which shows results by orders of magnitude closer to the reference.

2.1.4. Hébert benchmark

As it can be observed in Fig. 4, the geometry of the Hébert benchmark is very similar to the one of the Cartesian benchmark: it is constituted by the same three materials (fuel, reflector, and pure absorber). The only difference is the shape of the assemblies: it consists of hexagonal fuel assemblies with a pitch of 32.9 cm (Dürigen, 2013). Also the nuclear data structure is similar to the Cartesian benchmark and the values for the one-energy-group cross sections can be found in Table 5. For this benchmark, the comparison is done using the TRIVAC SP_3 solver as reference, as it was done in Dürigen (2013). As in lo Muzio and Seubert (2022a), the SP_3 solver of DYN3D is used for the comparison as a code based on the SP_3 method. For this benchmark, the effective multiplication factor, as well as the normalized flux distributions are used as basis for the evaluation. The results of TRIVAC as well as DYN3D were taken from Dürigen (2013).

Fig. 5 shows the discrepancy in the effective multiplication factor of the FENNECS and DYN3D solvers, with respect to the TRIVAC solution, which is $k_{eff} = 1.000332$. For the FENNECS diffusion solver, for both meshes used, hence 6 and 24 radial elements per assembly, the deviation in the effective multiplication factor is above 4000 pcm, hence not tolerable. Furthermore, the mesh refinement here improves the results minimally. For the calculation with the FENNECS SP_3 solver, for the coarsest mesh, the discrepancy, with respect to TRIVAC, is less than one ninth of that of the diffusion solver for the same mesh, hence 502.4 pcm. However, for the same mesh, the error obtained

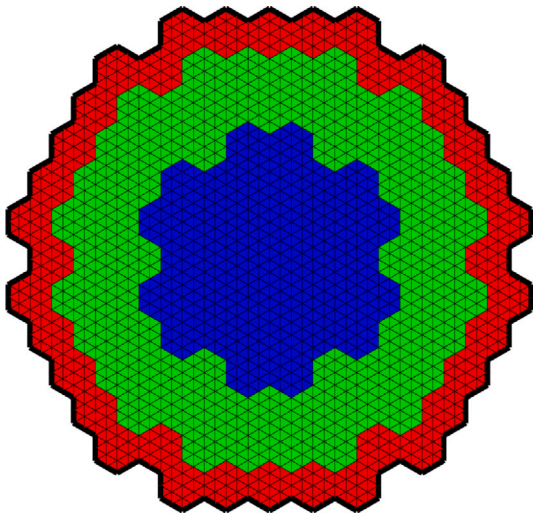

Fig. 4. Geometry of the Hébert benchmark, constituted by a central region made of fuel (blue), surrounded by a reflector (green) and an absorber (red). The black line represents the vacuum boundary condition. In axial direction, reflective boundary conditions are imposed. The mesh used here divides each assembly in 24.

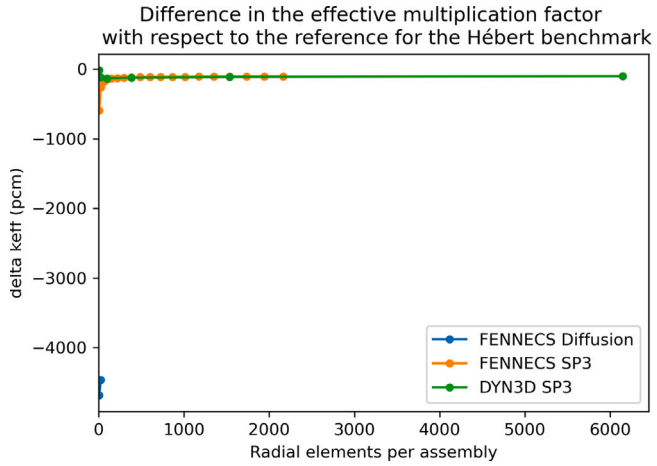

Fig. 5. For the Hébert benchmark, difference between the reference and the effective multiplication factors obtained with the FENNECS diffusion solver (blue), FENNECS SP_3 solver (orange) and the DYN3D SP_3 solver (green), versus the number of radial elements per assembly used for the mesh.

by the DYN3D SP_3 solver is significantly lower: it is only −76.7 pcm. Refining the mesh, the SP_3 solvers rapidly approach the reference. This holds particularly for FENNECS: starting from 384 radial elements per assembly, the effective multiplication factor of the FENNECS SP_3 solver is closer to the reference, compared to the one of the same solver of DYN3D. These results indicate that the new FENNECS solver shows a strong dependency on the mesh.

For this benchmark, also the normalized flux distributions of the FENNECS and DYN3D solvers were analysed with respect to the reference. To perform the evaluation, the root mean squared (RMS) error of the normalized flux distribution was calculated and this can be found in Fig. 6. Furthermore, in Table 6, the maximum and minimum errors can be found. As it can be observed in Fig. 7, and by analysing the RMS and maximum error, for coarse meshes, with DYN3D, results closer to the reference are obtained. Like the effective multiplication factor, also the RMS error of the normalized flux distribution decreases with increasing number of radial elements per assembly. In particular, as it was the case for the effective multiplication factor, also for the error in the nominalized power distribution, a strong decrease can be

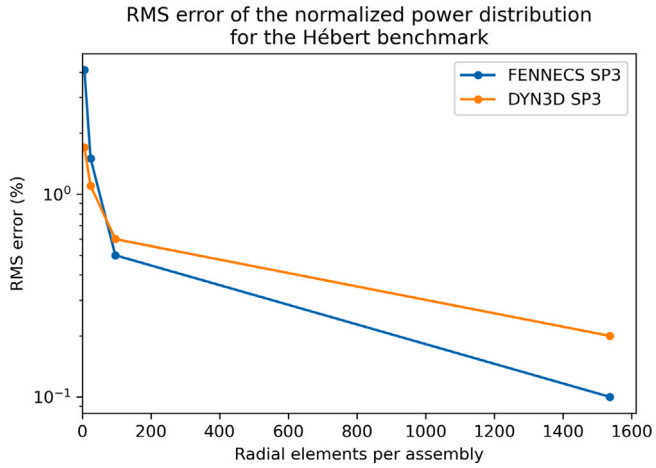

Fig. 6. For the Hébert benchmark, RMS error (%) of the normalized flux distribution, with respect to the reference, for the FENNECS SP_3 solver (blue) and the DYN3D SP_3 solver (orange), versus the number of radial elements per assembly used for the mesh. The *y*-axis has a logarithmic scale.

Table 6
For the Hébert benchmark, maximum errors (%) in the normalized flux distribution, with respect to the reference, for the SP_3 solver of FENNECS and DYN3D.

Radial elements per assembly	FENNECS SP_3	DYN3D SP_3
6	8.3	−2.5
24	3.2	−1.9
96	1.0	1.4
1536	−0.3	−0.5

observed. Actually, starting from 96 radial elements per assembly, with the FENNECS SP_3 solver better results from the point of view of the RMS and maximum error of the normalized flux distribution can be obtained, compared to DYN3D.

2.2. Test cases with generated cross sections

In this section, results of test cases, where the cross section libraries were generated with appropriate codes, are given. Here, the code used for the cross section generation is used also for the reference solution in order to evaluate the errors arising from the diffusion and SP_3 approximation.

2.2.1. Three cores of different size with cross sections generated by Serpent and ERANOS

These exercises were taken from Babcsány et al. (2022), where the goal was to study the effects of flux weighting during the cross section generation process on the solution of the SP_3 approximation of the transport equation with the code SPNDYN. As for the previous examples, in this section, the cross sections were found in the reference, together with the geometry description. However, in the previous examples only the solver functionality, excluding possible influences due to the cross sections generation method, were studied. In the three exercises which follow in this section, the macroscopic cross section libraries were generated with ERANOS and Serpent, hence two sets of cross sections are given. Since FENNECS as well as SPNDYN use the same libraries, discrepancies arising from different cross sections generation procedure can be excluded. Hence, here, the FENNECS results can be compared with the ones of SPNDYN and the influence of the cross section generation process can be observed. The two sets of cross sections are assembly-wise homogenized and have two energy groups. Within these sets of macroscopic cross sections, the (zeroth order) diffusion constant were included, which is equivalent to Eq. (2). Therefore, calculations with the SP_3 solver with the (zeroth order)

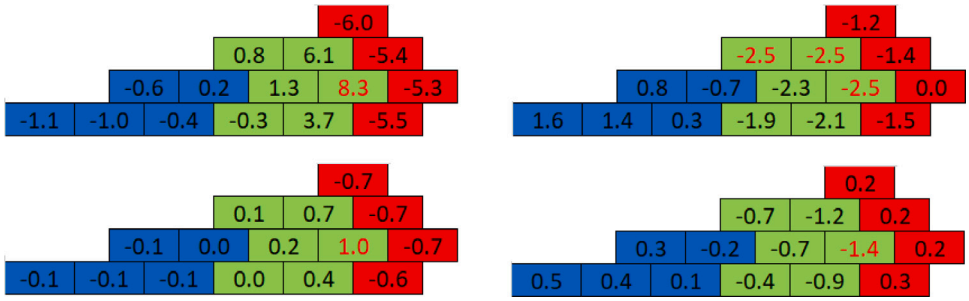

Fig. 7. Deviations (%) from the reference of the normalized neutron flux distributions for the SP_3 solvers of FENNECS (left) and DYN3D (right) with 6 (upper figures) and 96 (lower figures) radial elements per assembly. The red numbers are the maximum deviations. The blue, green and red regions represent the fuel, reflector and absorber assemblies, respectively.

diffusion constant from the reference as well as calculating the diffusion constant as dependent from the total and first order scattering cross sections, based on Eq. (1), will be performed.

Now, some information about the macroscopic cross section generation process is provided. Two families of codes are used for the cross section generation. The first one includes codes designed to generate cross sections for diffusion codes (Babcsány et al., 2022). Generally, they can generate also multi-group higher order anisotropic scattering data, where these are all weighted by the scalar flux, and not by the flux of the same scattering order (Babcsány et al., 2022). Examples of codes performing this scalar flux weighting for higher order anisotropic scattering data are SCALE, the model of HELIOS-2 based on the collision probability method, and Serpent 2 (Babcsány et al., 2022). According to Babcsány et al. (2022), this approach can cause an insufficient accuracy for codes using these higher order scattering data, especially for systems having a small size, or high leakage or for fast reactors. Actually, in the case of Serpent, scattering data up to the seventh order can be obtained. However, their applicability in higher order deterministic codes was not properly verified and validated yet (Cai, 2014). Actually in Lin and Yang (2020), the authors stated that the anisotropic scattering cross sections of Serpent 2 may not be adequate for fast reactors, where the consideration of the anisotropic scattering may be more relevant than, for example, for light water reactors (LWR). Furthermore, also the topic of the influence of the statistical uncertainties for the higher order scattering data should be addressed, particularly when the values of the scattering data are small. The codes of the second family perform higher-order angular flux weighting, hence the neutron flux of the corresponding scattering order is used (Babcsány et al., 2022). An example of a code in this category is the MoC method implemented in HELIOS-2, which applies the angular flux-moment weighting (Babcsány et al., 2022). Therefore, it condenses the anisotropic scattering matrices by performing the current weighting (Babcsány et al., 2022). The angular flux-moment weighting is a generalization of the P_1 consistent method implemented in the ECCO module of the ERANOS program (Babcsány et al., 2022).

In the test case shown here, 3 cores of different radial sizes, having an assembly pitch of 18.45 cm, are modelled. The three cores are a small one, a medium one and a large one, consisting of 3×3, 9×9, and 19×19 standard rectangular fuel assemblies, respectively, which are depicted in Fig. 8. Radially, vacuum boundary conditions are applied and axially reflective ones. In addition, with the same cross sections, also a core of infinite size, hence with radially and axially reflective boundary conditions, was modelled. The results of the FENNECS SP_3 and diffusion solver will be compared with the ones of SPNDYN, which provides the same solution methods. Concerning the SP_3 solvers, here, the results will be obtained using the (zeroth order) diffusion constant, hence D_0 as defined in the first part of this work, where the definition is based on the total and first order macroscopic scattering cross section, hence as in Eq. (1), as well as using the (zeroth order) diffusion constant as defined in the diffusion approximation, based on Eq. (2). In the following tables, with SP_3 the simulations relying on the first approach, hence on Eq. (1), will be meant. Calculations performed with the second approach will be addressed with SP_3 TR, since they rely on the transport cross section, as it can be seen in Eq. (2). As reference, effective multiplication factors obtained from the respective Serpent reference model will be used, independently of the set of cross sections applied. Additionally, in order to obtain the reactivity decrease due to the reactor size, hence due to the leakage, also the effective multiplication factor for the infinite core is calculated, hence k_∞. These reactivity due to the neutron leakage is calculated as the difference between the inverse of k_∞ and the inverse of the obtained k_{eff} with the same solver mesh and cross sections, hence as follows:

$$\rho_{leakage} = \frac{1}{k_\infty} - \frac{1}{k_{eff}}. \tag{3}$$

This quantity is used to measure the leakage of each geometry, hence the normalized leakage rate, expressed in pcm. The evaluation of this quantity is performed to judge the ability of the methodology in modelling systems with different magnitudes of leakage. The cross sections as well as the results of SPNDYN, Serpent and ERANOS are taken from Babcsány et al. (2022).

The deviations between the infinite multiplication factors and Serpent and ERANOS references, which are 1.312280 ± 0.00004 and 1.307050, respectively, can be found in Table 7. Here, it can be observed that if the same set of cross sections is used, all the three solvers of both codes deliver the same errors, with respect to the same reference. This is reasonable, since in the infinite multiplication factor no leakage is considered. Therefore, here the infinite multiplication factor just shows that the numerics of the codes are correct and it can be seen as a verification test. In particular, in the case where Serpent is used for the cross sections generation as well as a reference, the error is within the statistical uncertainty. The error becomes slightly higher if ERANOS cross sections are used: if the comparison is performed with ERANOS, the error is around 16 pcm and if Serpent is used as reference, the error is one order of magnitude higher and this is the only case where the error is negative. Hence, the multiplication factor is underestimated. This high deviation can be explained by the fact that different codes are used for the cross sections generation and as reference.

Firstly, the large core will be analysed. As it can be observed in Table 8, the results obtained by FENNECS and SPNDYN differ by maximum 2 pcm. Like for k_∞, considerable differences can be observed if Serpent is used as reference and if Serpent or ERANOS cross sections are used. With this regard, the k_{eff} obtained with Serpent cross sections show smaller discrepancies to the Serpent effective multiplication factor, which is $k_{eff} = 1.30151 \pm 0.00002$. For the FENNECS calculations, refining the mesh, hence from 4 radial elements per pin cell to 16, does not influence the effective multiplication factor. Here, the best results are given by the SP_3 solver using the diffusion coefficient calculated by Serpent. Similar results are given also by the diffusion solvers. Larger deviations are given by the SP_3 solvers, which calculate the diffusion coefficient based on the higher order scattering cross sections. In particular, here, the effective multiplication factor as well as the reactivity

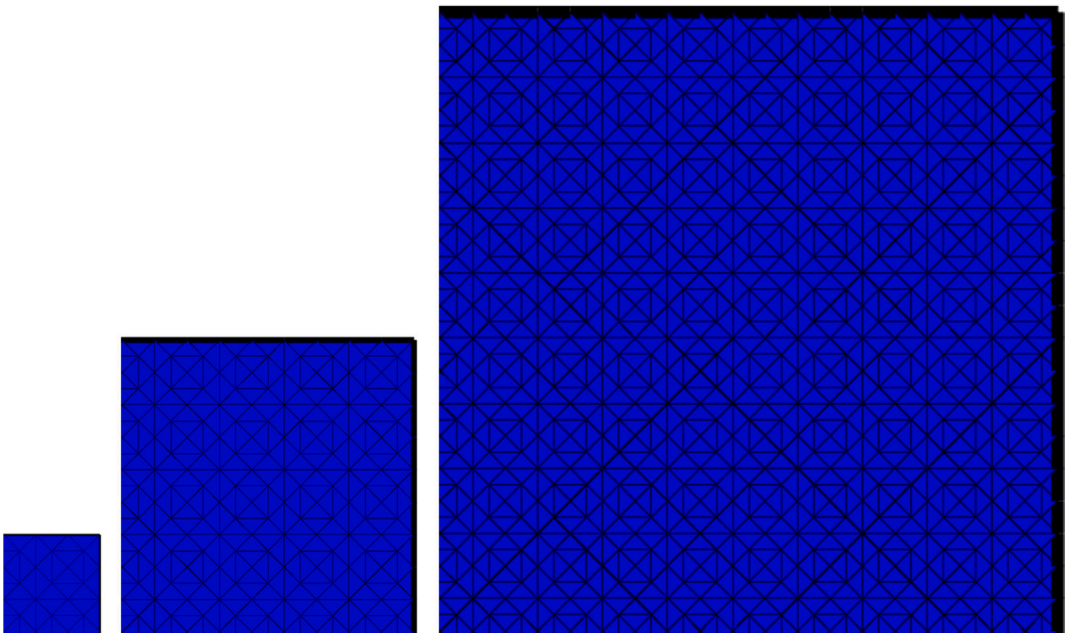

Fig. 8. One fourth of the geometry of the small (left), medium (center) and large core (right) with the mesh using 16 radial elements per pin cell. The black line represents the vacuum boundary condition.

Table 7
Deviations (pcm) between the k_∞ of Serpent or ERANOS and the one calculated with the FENNECS or SPNDYN diffusion and SP_3 solvers, where D_0 is obtained based on Eq. (1) (SP_3) or Eq. (2) (SP_3 TR). The results were obtained using Serpent as well as ERANOS cross sections.

Cross sections	Serpent		ERANOS			
Reference	Serpent		ERANOS		Serpent	
Program	FENNECS	SPNDYN	FENNECS	SPNDYN	FENNECS	SPNDYN
Diffusion	4	4	16	16	−289	−289
SP_3	4	4	16	15	−289	−290
SP_3 TR	4	4	16	15	−289	−290

Table 8
For the large geometry, discrepancy between the k_{eff} and $\rho_{leakage}$ of Serpent and the ones calculated using Serpent cross sections together with the FENNECS or SPNDYN diffusion and SP_3 solvers, where D_0 is obtained based on Eq. (1) (SP_3) or Eq. (2) (SP_3 TR). Gray cells indicate the results with the best agreement with the reference. FENNECS calculations were performed with two meshes: 4 (F - 4) and 16 (F - 16) radial elements per pin cell.

	Discrepancy in k_{eff} [pcm]			Discrepancy in $\rho_{leakage}$ [pcm]		
Program	F - 4	F - 16	SPNDYN	F - 4	F - 16	SPNDYN
Diffusion	−25	−24	−24	−28	−28	−27
SP_3	147	148	146	144	145	142
SP_3 TR	−24	−23	−22	−28	−27	−26

are overestimated, hence $\rho_{leakage}$ is underestimated. These findings hold for FENNECS as well as SPNDYN. According to the Serpent calculations, this reactivity is -631 ± 4 pcm.

The deviations in the effective multiplication factors significantly increase if ERANOS cross sections are used, as shown in Table 9. This was the case also for the infinite geometry. Also in this case, the FENNECS and SPNDYN results differ by maximum 2 pcm. Furthermore, the mesh refinement affects the effective multiplication factor by maximum 2 pcm. Here, the best results are obtained by the SP_3 solver, which does not use the Serpent transport cross section. This shows a strong dependency of the results on the method used to generate the macroscopic cross sections. Consequently, if the diffusion constant is calculated using the first order scattering cross section and if the higher order scattering cross sections are weighted with the higher order fluxes, as in ERANOS, better results, concerning the k_{eff}, compared to the diffusion solver, can be obtained. However, if the $\rho_{leakage}$ is evaluated, which is -631 ± 4 pcm, errors within the Serpent calculation uncertainties are obtained with the diffusion and the SP_3 solver using the transport cross section and the errors of the SP_3 solver are within twice of the uncertainty.

Secondly, the medium core is analysed. Here, the Serpent reference k_{eff} and the reactivity decrease due to the smaller size of the core are 1.26735 ± 0.00002 and -2702 pcm, respectively. Also here, the results of SPNDYN and FENNECS are very similar. As it can be observed in Table 10, if the Serpent cross sections are used, the error in the effective multiplication factor and the reactivity due to the size are the lowest for the SP_3 solver using the transport cross section provided by Serpent: with FENNECS using the mesh with 36 radial subdivisions per assembly, the error in the k_{eff} and in $\rho_{leakage}$ are -125 pcm and -129 pcm, respectively. Since, for the diffusion solver as well as for the SP_3 solver using the transport cross section provided by Serpent, the discrepancies are negative, the leakage is overestimated.

Using ERANOS cross sections, as it was the case for the large geometry, the lowest error in the effective multiplication factor and in the reactivity is obtained with the SP_3 solver, which does not use the transport cross section, as shown in Table 11. Even though, with

Table 9
For the large geometry, discrepancy between the k_{eff} and $\rho_{leakage}$ of Serpent and the ones calculated using ERANOS cross sections together with the FENNECS or SPNDYN diffusion and SP_3 solvers, where D_0 is obtained based on Eq. (1) (SP_3) or Eq. (2) (SP_3 TR). Gray cells indicate the results with the best agreement with the reference. FENNECS calculations were performed with two meshes: 4 (F - 4) and 16 (F - 16) radial elements per pin cell.

	Discrepancy in k_{eff} [pcm]			Discrepancy in $\rho_{leakage}$ [pcm]		
Program	F - 4	F - 16	SPNDYN	F - 4	F - 16	SPNDYN
Diffusion	−292	−291	−291	−3	−1	−1
SP_3	−284	−283	−285	5	6	5
SP_3 TR	−292	−290	−290	−2	−1	0

Table 10
For the medium geometry, discrepancy between the k_{eff} and $\rho_{leakage}$ of Serpent and the ones calculated using Serpent cross sections together with the FENNECS or SPNDYN diffusion and SP_3 solvers, where D_0 is obtained based on Eq. (1) (SP_3) or Eq. (2) (SP_3 TR). Gray cells indicate the results with the best agreement with the reference. FENNECS calculations were performed with three meshes: 4 (F - 4), 16 (F - 16), 36 (F - 36) radial elements per pin cell.

	Discrepancy in k_{eff} [pcm]				Discrepancy in $\rho_{leakage}$ [pcm]			
Program	F - 4	F - 16	F - 36	SPNDYN	F - 4	F - 16	F - 36	SPNDYN
Diffusion	−160	−143	−138	−136	−164	−147	−141	−140
SP_3	574	588	593	582	571	585	589	578
SP_3 TR	−152	−132	−125	−122	−155	−136	−129	−126

Table 11
For the medium geometry, discrepancy between the k_{eff} and $\rho_{leakage}$ of Serpent and the ones calculated using ERANOS cross sections together with the FENNECS or SPNDYN diffusion and SP_3 solvers, where D_0 is obtained based on Eq. (1) (SP_3) or Eq. (2) (SP_3 TR). Gray cells indicate the results with the best agreement with the reference. FENNECS calculations were performed with three meshes: 4 (F - 4), 16 (F - 16), and 36 (F - 36) radial elements per pin cell.

	Discrepancy in k_{eff} [pcm]				Discrepancy in $\rho_{leakage}$ [pcm]			
Program	F - 4	F - 16	F - 36	SPNDYN	F - 4	F - 16	F - 36	SPNDYN
Diffusion	−345	−328	−323	−321	−55	−38	−34	−32
SP_3	−305	−287	−281	−289	−15	3	9	0
SP_3 TR	−335	−316	−310	−308	−45	−26	−20	−18

Table 12
For the small geometry, discrepancy between the k_{eff} and $\rho_{leakage}$ of Serpent and the ones calculated using Serpent cross sections together with the FENNECS or SPNDYN diffusion and SP_3 solvers, where D_0 is obtained based on Eq. (1) (SP_3) or Eq. (2) (SP_3 TR). Gray cells indicate the results with the best agreement with the reference. FENNECS calculations were performed with three meshes: 4 (F - 4), 16 (F - 36), and 36 (F - 36) radial elements per pin cell.

	Discrepancy in k_{eff} [pcm]				Discrepancy in $\rho_{leakage}$ [pcm]			
Program	F - 4	F - 16	F - 36	SPNDYN	F - 4	F - 16	F - 36	SPNDYN
Diffusion	−1974	−753	−687	−663	−1978	−757	−691	−668
SP_3	3836	4868	4935	4840	3832	4864	4930	4836
SP_3 TR	−1608	−341	−249	−217	−1612	−346	−254	−221

36 radial elements per pin cell, the error in the effective multiplication factor is −281 pcm, but the deviation in $\rho_{leakage}$ is only 9 pcm. This error is even lower and below the Serpent uncertainty if the mesh with 16 radial elements per pin cell is considered.

Thirdly, the small core is analysed. For the FENNECS results, a very strong dependency on the mesh could be observed. Here, similar effective multiplication factors to the ones of SPNDYN could be only obtained with FENNECS using the mesh, which divides radially each assembly in 36. As shown in Table 12, if Serpent cross sections are used, the best results are obtained with the SP_3 solver using the transport cross section of Serpent. In this case, both errors for SPNDYN as well as FENNECS with 36 radial subdivisions are at the maximum −254 pcm. This holds for the effective multiplication factor as well as the reactivity due to the leakage. This highly negative discrepancy shows a strong overestimation of the leakage. This overestimation is considerably larger for the diffusion solver.

As shown in Table 13, if ERANOS cross sections are used, the scenario is more complex than in the previous cases. For the FENNECS diffusion solver, the errors decrease with increasing mesh refinement, such that with 36 radial element per assembly, the error in the reactivity due to the size reduction is only 7 pcm, which is quite surprising, due to the small size of the core and the known limitations of diffusion theory in modelling heterogeneous media. For the FENNECS SP_3, for both types of diffusion constants used, it can be observed that both types of errors are strongly negative for the coarsest mesh. Refining the mesh, the error approaches zero and it is positive for the mesh with 36 radial elements per pin cell. Therefore, the best solver for this geometry cannot be identified uniquely, like it was the case for the previous geometries, because here the mesh shows a very strong impact on the results. Furthermore, a correlation between the method used to generate the cross sections and the most suited SP_3 approach, with regards to the diffusion constant, cannot be established. If the error in the effective multiplication factor is considered, the best agreement is obtained with the SP_3 solver, which does not use the transport cross section, and with the mesh with 36 radial elements per assembly. If the error in the reactivity due to size reduction is considered, as said before, the best agreement is obtained with the diffusion solvers: the one of FENNECS, which uses 36 elements per assembly, and the one of SPNDYN show errors of only 7 pcm and 93 pcm, respectively.

For the calculations using the Serpent cross sections, it should be remarked that a considerable difference could be observed between the results obtained with the SP_3 and the SP_3 TR: using this last method, the discrepancy in the k_{eff} is always at least halved, compared to the one obtained using the first order scattering cross section, for the

Table 13
For the small geometry, discrepancy between the k_{eff} and $\rho_{leakage}$ of Serpent and the ones calculated using ERANOS cross sections together with the FENNECS or SPNDYN diffusion and SP_3 solvers, where D_0 is obtained based on Eq. (1) (SP_3) or Eq. (2) (SP_3 TR). Gray cells indicate the results with the best agreement with the reference. FENNECS calculations were performed with three meshes: 4 (F - 4), 16 (F - 36), and 36 (F - 36) radial elements per pin cell.

	Discrepancy in k_{eff} [pcm]				Discrepancy in $\rho_{leakage}$ [pcm]			
Program	F - 4	F - 16	F - 36	SPNDYN	F - 4	F - 16	F - 36	SPNDYN
Diffusion	−1473	−558	−282	−196	−1184	−269	7	93
SP_3	−837	87	374	379	−548	376	663	668
SP_3 TR	−1050	−119	169	277	−761	170	458	566

Table 14
Deviations (pcm), with respect to Serpent, of the effective multiplications factor for the highly enriched uranium fuel assembly obtained with the FENNECS SP_3 and diffusion solver, with different axial (3 and 59 axial layers) and radial (4 and 16 radial subdivisions per assembly) spatial discretizations.

Solver		SP_3		Diffusion	
Number of radial elements per assembly		4	16	4	16
Number of axial elements per assembly	3	5724	523	27393	20 235
	59	5574	371	27179	20 022

Table 15
Deviation (pcm), with respect to HELIOS, of the effective multiplications factor for the UO_2 assembly obtained with the FENNECS SP_3 and diffusion solver, with different meshes (4 and 16 radial subdivisions per pin cell).

Number of radial elements per pin cell	4	16
Diffusion	66	53
SP_3	42	27

calculation of the diffusion coefficient. Where ERANOS cross sections are used, the results obtained with the two SP_3 approaches are closer to each other. At this point, it remains difficult and premature to affirm, which is the best approach to use, depending on the cross sections used, also due to the good results, shown in the next sections, obtained with the SP_3 method, calculating the diffusion coefficient with the first order scattering cross section and using Serpent cross sections. Furthermore, the best approach to use, from the point of view of the diffusion coefficient, as well cross sections generation, could be strongly influenced by the type of system analysed, whether fast or thermal, as well as on the size of it. For this reason, also for these test cases, further studies should be performed, in order to obtain more insights about the effects of the cross section generation methodology on the results. These could comprehend the comparison of the power distributions or the 2 energy groups neutron flux distributions, which were not provided for these three cores.

2.2.2. Highly enriched uranium fuel assembly

This test case consists of a very simplified squared fuel assembly with uranium fuel having an enrichment of $96wt-\%$. The enrichment was chosen in order to obtain a system close to criticality. The fuel assembly was modelled in a very simplified way, as a fuel parallepiped having a width and a height of 21.42 cm, and 100 cm, respectively. On all the surfaces of the geometry, the vacuum boundary conditions are applied. The two energy groups assembly-wise homogenized macroscopic cross sections, as well as the reference effective multiplication factor, were obtained with Serpent. Since this is the only example where vacuum boundary conditions are applied on all surfaces of the geometry, here the performance of the SP_3 solver, compared to the one of the diffusion solver, is also analysed with respect to the axial spatial discretization. As reference, $k_{eff} = 0.86590 \pm 0.00008$ was used, which was calculated by Serpent.

Table 14 shows the deviations, with respect to Serpent, in the effective multiplication factors obtained with the SP_3 and diffusion solver of FENNECS for the different axial and radial spatial discretizations. Firstly, for both solvers, high deviations with respect to Serpent are observed. This can be explained by the very small size of the geometry and its high heterogeneity due to the vacuum boundary conditions. Secondly, the results show a higher dependency on the radial discretization, compared to the axial one: with the SP_3 solver, refining the mesh radially, improves the results by one order of magnitude. Thirdly, for the diffusion solver, the deviations in the effective multiplication factor are orders of magnitude larger, compared to the ones of the SP_3 solver, independently of the mesh. The errors of the diffusion solver are above 20000 pcm, and therefore unacceptable. Here, mesh refinement only weakly improves the results. Fourthly, from results of the SP_3 solver, it can be concluded, that for such small geometries in radial direction, the mesh with only 4 radial subdivisions per assembly is too coarse and the one with 16 radial subdivisions must be used. For such radial discretization and with 59 axial layers, an error of 371 ± 8 pcm can be achieved, which is an acceptable result for such very small geometry.

2.2.3. C5G7

This example is based on the UO_2 and MOX fuel assemblies description of the C5G7 benchmark, taken from Smith et al. (2003). In this work, these are modelled individually with reflective boundary conditions. As described in lo Muzio et al. (2022), the pin cell-wise homogenized cross section libraries are generated with the HELIOS-1.12 solver based on the collision probabilities. The pin cell-wise homogenized cross section libraries were validated with the multigroup transport code TORT-TD, based on the discrete ordinates approach, developed at GRS (Seubert et al., 2008). For the calculation of the pin power distribution, HELIOS-1.12 was used. In particular, for these two fuel assemblies, hence for these two distinct geometries, on which two kinds of meshes were applied, the effective multiplication factors as well as pin power distributions were analysed.

For the UO_2 fuel assembly, depicted in Fig. 9, HELIOS calculated an effective multiplication factor of 1.32705. As it can be seen from Tables 15 and 16, for the UO_2 fuel assembly, deviations in the same order of magnitude for both solvers are obtained, but the results of the SP_3 solver show a better agreement with the reference. In particular, for this solver, the mesh refinement halves the deviation in the effective multiplication factor as well as the one in the normalized pin power distribution, as stated by the root mean squared (RMS) and maximum errors. It should be remarked that for the finest mesh, hence the one with 16 radial elements per fuel pin, the deviation in the effective multiplication factor is only 27 pcm and the RMS and maximum error of the normalized power distribution only 0.23% and 0.55%, respectively. With FENNECS v0.2.17, the calculations with the finest mesh using the diffusion and SP_3 solver took 3.8 s, and 14.0 s, respectively. These were performed with 8 shared memory (OpenMP) threads.

The Tables 17 and 18 show that a good agreement between the results of the SP_3 solver and HELIOS are obtained also for the MOX fuel assembly. As it can be observed in Fig. 10, the geometry of this fuel assembly is more heterogeneous. The limitation of the diffusion approximation in modelling such more heterogeneous (compared to the UO_2 assembly) geometries is reflected in the errors in the effective multiplication factors as well as in the RMS and maximum error in the normalized power distribution, which are higher compared to the

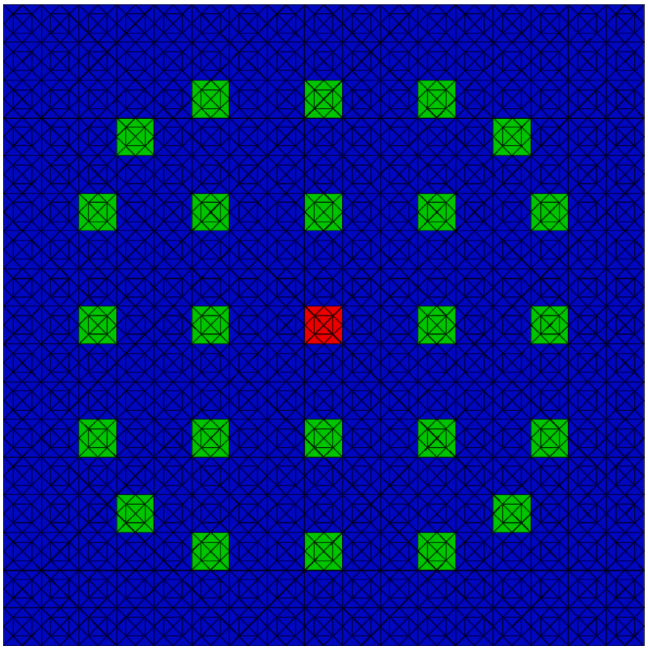

Fig. 9. Representation of UO_2 fuel assembly with the mesh using 16 radial elements per pin cell performed by PEMTY. The blue region contains UO_2 fuel pins. The green and red cells contain guide tubes and the fission chamber, respectively.

Table 16
For the UO_2 assembly, RMS and maximum error (%), with respect to HELIOS, of the normalized power distributions obtained with the FENNECS SP_3 and diffusion solver, with different meshes (4 and 16 radial subdivisions per pin cell).

	RMS error		Max error	
Number of radial elements per pin cell	4	16	4	16
Diffusion	0.54	0.25	1.43	0.68
SP_3	0.52	0.23	1.48	0.55

Table 17
Deviation (*pcm*), with respect to HELIOS, of the effective multiplications factor for the MOX assembly obtained with the FENNECS SP_3 and diffusion solver, with different meshes (4 and 16 radial subdivisions per pin cell).

Number of radial elements per pin cell	4	16
Diffusion	−85	93
SP_3	−51	−51

UO_2 assembly. Also the difference between the deviations arising from the diffusion and SP_3 solver is higher compared to the previous case. For the MOX assembly, the mesh refinement causes an improvement of the results only from the point of view of the normalized pin power distribution. In particular, here the RMS error in the normalized power distribution is above 1.11% for the calculation with the diffusion solver and the coarsest mesh. With the finest mesh, the SP_3 solver delivers a deviation in the effective multiplication factor and an RMS error in the power distribution of −51 pcm and 0.46%, respectively.

2.2.4. European Sodium Fast Reactor (ESFR)

In this subsection, the ESFR, a large sodium cooled fast reactor, described within the project "European Sodium Fast Reactor Safety Measures Assessment and Research Tools" (ESFR-SMART) (Rineiski et al., 2018), is modelled. The calculation results presented in this subsection aim firstly to prove the ability of the new FENNECS solver in modelling also large cores.

For this test case, the mascroscopic cross sections in 10 energy groups were obtained using Serpent. For this purpose, three-dimensional models of the assemblies were prepared. In particular, the Control

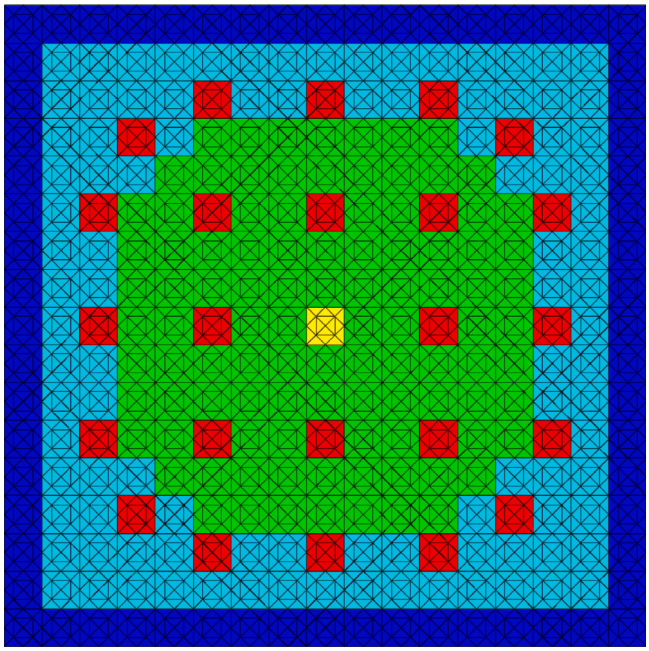

Fig. 10. Representation of MOX fuel assembly with the mesh using 16 radial elements per pin cell performed by PEMTY. The blue, light blue, and green regions contain fuel pins made of 4.3%, 7.0%, and 8.7% MOX, respectively. The red and yellow cells contain guide tubes and the fission chamber, respectively.

Table 18
For the MOX assembly, RMS and maximum error (%), with respect to HELIOS, of the normalized power distributions obtained with the FENNECS SP_3 and diffusion solver, with different meshes (4 and 16 radial subdivisions per pin cell).

	RMS error		Max error	
Number of radial elements per pin cell	4	16	4	16
Diffusion	1.11	0.64	1.95	1.54
SP_3	0.88	0.46	1.44	1.00

Shutdown Device (CSD) and the Diverse Shutdown Device (DSD) rods were modelled as surrounded by 6 half of fuel assemblies. These libraries were used to model with the FENNECS diffusion and SP_3 solver the ESFR core in nominal condition, hence all rods out (ARO), plus in further 11 core scenarios with different positions of the CSD and the DSD rods, where the last position is all rods in (ARI). In the ARO scenario, using the version v0.21.7 of FENNECS and with 8 shared memory (OpenMP) threads, the calculation duration was 1560.4 s and 991.8 s with the SP_3 and diffusion solver, respectively. As in all exercises, except in Section 2.2.1, in all SP_3 calculations, the definition of the zeroth order diffusion coefficient given in Eq. (1) was used. For the 12 configurations, reference solutions were obtained with Serpent. Additionally, for this exercise, the Superhomogeneisation (SPH) method was applied to the cross section libraries of the absorber materials, hence to the natural and enriched boron contained in the CSD and DSD rods. For this purpose, three-dimensional Serpent models of the absorber materials were developed, where the boron is surrounded by 6 half of fuel assemblies. Using the cross section libraries obtained by such models, the calculation of the SPH corrected cross sections was performed by the external tool PEMTY, which uses the FENNECS diffusion solver for the calculation of the fluxes. The SPH correction implemented in PEMTY relays on the approach originally described by Hébert in Hébert and Benoist (1991), as well explained in Bousquet (2021). The implementation of the SPH correction in PEMTY was also demostrated in Henry et al. (2021). Using for the absorber materials the SPH corrected cross section libraries, for the 12 scenarios, FENNECS diffusion calculations were performed. The SPH

Table 19
For the ESFR core, error in the effective multiplication factor (*pcm*) and control rod (CR) worth (*pcm*) as well as RMS and maximum error (%) in the normalized power distributions, with respect to Serpent, obtained with the diffusion (D) and SP_3 solver of FENNECS as well as with its diffusion solver, where the SPH correction was applied to the cross section libraries.

	Error in keff (*pcm*)			Error in CR worth (*pcm*)			RMS error power (%)			Max error power (%)		
	D	SP_3	SPH	D	SP_3	SPH	D	SP_3	SPH	D	SP_3	SPH
0	−88	73	120				1.33	1.22	1.18	3.23	2.52	4.11
1	−90	74	130	2	−1	14	1.50	1.38	1.24	3.42	2.86	4.49
2	−91	80	153	3	−7	56	1.45	1.33	1.22	2.77	2.54	3.83
3	−126	56	161	38	17	71	1.70	1.51	1.36	4.00	3.60	4.18
4	−185	14	158	97	58	64	2.46	2.16	1.42	5.70	4.92	4.28
5	−262	−43	143	174	116	36	3.76	3.25	1.32	8.87	7.54	3.77
6	−345	−105	120	257	178	1	5.61	4.84	1.24	13.41	11.40	4.32
7	−417	−160	98	329	233	−27	7.74	6.68	1.57	18.47	15.85	4.13
8	−495	−222	65	407	295	−60	9.85	8.50	1.85	23.67	20.37	4.74
9	−558	−270	42	470	343	−77	11.98	10.35	2.43	28.57	24.66	6.43
10	−615	−315	23	526	388	−91	13.98	12.15	3.38	33.08	28.79	8.86
11	−664	−355	7	576	428	−101	15.71	13.77	4.66	35.85	31.43	11.14

corrected cross sections were used only to run diffusion calculations. No SP_3 simulations were performed with the SPH corrected cross sections, since the SPH method in PEMTY relays on the diffusion solver.

This study is based on the evaluation, with respect to the reference, of the effective multiplication factor as well as the root mean squared (RMS) and maximum error in the normalized assembly-wise power distribution. Secondly, simulations with different control rod positions will analyse the ability of the FENNECS SP_3 solver in modelling controlled states, with respect to the diffusion solver, for which these scenarios are challenging. Thirdly, the FENNECS SP_3 solver results will be evaluated also with respect to the results of the diffusion solver, where the SPH method was applied to the cross sections.

In all Serpent calculations the statistical uncertainty of the effective multiplication factor was never above 4.90 pcm. As discussed in lo Muzio and Seubert (2023), in Table 19, it can be observed that for all parameters analysed, the results of the FENNECS SP_3 solver are always closer to the reference compared to the ones of the diffusion solver. From this first observation, it can be already stated that improvements by the SP_3 method can be achieved from the point of view of the effective multiplication factor as well as power distribution for states going from the uncontrolled ones to the strongly controlled ones using the FENNECS SP_3 solver, with respect to the diffusion solver. The fact that, also for large cores, the SP_3 approximation is able to deliver more accurate results is not surprising, since it accounts, to a certain extent, also for neutron flux anisotropies and anisotropic scattering.

Based on the obtained results, it can be distinguished between the weakly controlled states and the more controlled ones. For the first ones, hence the ARO configuration as well as the first two insertion steps, the magnitude of the errors found is very similar for the SP_3 and diffusion solver. Hence, in these cases, using the SP_3 solver only weakly improves the results. This holds particularly for the effective multiplication factor and control rod (CR) worth. It should be remarked that for these two quantities, the error obtained by the SP_3 has an opposite sign, compared to the one of the diffusion solver: the value is positive. Hence, the k_{eff} is overestimated, leading to a more conservative approach. On the contrary, the diffusion solver underestimates it, leading to issues from the point of view of the safety. A visible improvement of the effective multiplication factor and RMS error of the power distribution could be obtained only by performing the SPH correction on the cross section libraries before using the diffusion solver. However, from the maximum and RMS error, it can be concluded that the error distributions are more flat for the results of the SP_3 solver.

For the medium controlled states, good results could be achieved with the SP_3 solver. For instance, in step 5 the error in the effective multiplication factor is only −43 pcm. On the contrary, for the diffusion solver it is above 200 pcm. In some cases, regarding the effective multiplication factor and CR worth, the results are even better than with the SPH corrected cross sections. For example, this is the case in step 4.

For the strongly controlled scenarios, large errors were obtained by the diffusion as well as SP_3 solver, even though, the last one delivered results closer to the reference. For example, in ARI, the error in the effective multiplication factor is −664 pcm and −355 pcm for the diffusion and SP_3 solver, respectively. This result proves again that the diffusion solver is not suited to model strongly controlled scenarios, if no correction is applied to the cross sections. In the meantime, it shows that also the SP_3 solver has difficulties in such cases. In particular, from the safety point of view, issues arise, since both solvers overestimate the CR absorption capability. For such configurations, reasonable results are obtained only for the calculations with SPH corrected cross sections and the diffusion solver. However, also here the maximum error in the power distribution is still too high: for the ARI configuration, the error is above 10%. These results prove that to model such controlled states, for the SP_3 solver, further development is necessary. An option could be the implementation of the SPH correction for this solver. Alternatively, a more suited energy groups structure could be studied.

3. Conclusion

In this paper, all works performed for the verification of the newly implemented SP_3 solver in the GRS neutronic code FENNECS were presented. To validate the code, test cases with already given cross section libraries as well as with cross section libraries generated by the authors were used. In the first case, using reference results, obtained from codes relying on more accurate methods, the FENNECS SP_3 solver results were compared to the ones obtained from other programs offering also an SP_3 solver, as well as to results of the diffusion solver. For test cases where the cross sections were generated by the authors, the results of the FENNECS SP_3 solver were compared to the ones of the FENNECS diffusion solver, where to generate the reference solution the same program used for the cross section generation was used. The calculation results analysed were the effective multiplication factor and in some cases the reactivity due to the finite size of the geometry, the normalized neutron flux or power distributions or the control rod worth.

Firstly, for all the cases discussed in this work, the FENNECS SP_3 solver showed results much closer to the reference compared to the ones of the diffusion solver. In some cases, the deviations arising from the diffusion solver were orders of magnitude higher compared to the ones of the SP_3 solver. This shows the necessity of using this newly implemented solver to model accurately heterogeneous and small geometries with a very high leakage.

Secondly, in all the test cases analysed, a good agreement between the reference effective multiplication factor, normalized power and neutron flux distributions was achieved. This shows that the SP_3 approximation was correctly implemented in the GRS neutronic code FENNECS. The good agreement could be achieved even for very small geometries.

Thirdly, in this work, also controlled states were modelled. Here, the FENNECS SP_3 solver calculated power distributions, effective multiplication factors and control rod worths near to the reference solutions for weakly controlled states. For strongly controlled states, the limitations of this methodology were visible. Here, better results, compared to the diffusion solver were obtained. However, the usage of SPH corrected cross sections in the diffusion solver delivered results closer to the reference, compared to the SP_3 approach. This point shows the necessity of further improving the solver in order to be able to model also strongly controlled states.

Fourthly, in this work, the effect on the effective multiplication factor of using different approaches for the macroscopic cross section libraries was shown and depending of the approach used to generate the libraries different definitions of the zeroth order diffusion coefficient should be used. With this regard, further investigations are necessary.

In the future, the steady state FENNECS SP_3 solver will be tested on more realistic (v)SMRs and MMRs configurations, in order to prove its ability to perform their safety assessment. Furthermore, the solver will be extended to be able to perform transient calculations.

CRediT authorship contribution statement

Silvia lo Muzio: Methodology, Software, Validation, Formal analysis, Investigation, Data curation, Writing – original draft, Writing – review & editing, Visualization. **Armin Seubert:** Conceptualization, Funding acquisition, Project administration, Supervision, Validation, Resources, Writing – review & editing.

Declaration of competing interest

The authors declare that they have no known competing financial interests or personal relationships that could have appeared to influence the work reported in this paper.

Data availability

Data will be made available on request, if not proprietary or otherwise protected.

Acknowledgements

This work was supported by the German Federal Ministry for the Environment, Nature Conservation, Nuclear Safety and Consumer Protection.

References

Babcsány, B., Böröczki, Z., Maróti, J., Szieberth, M., 2022. On the effect of scalar flux weighting of linearly anisotropic scattering matrices in few-group transport calculations. In: PHYSOR Proceedings.

Bousquet, J., 2021. Development of advanced methods for safety assessment of sodium cooled fast reactors (Ph.D. thesis). Fakultät für Maschinenwesen Institut für Energietechnik, Professur für Wasserstoff- und Kernenergietechnik, Technische Universität Dresden, Dresden.

Bousquet, J., Seubert, A., Henry, R., 2020. New finite element neutron kinetics coupled code system FENNECS/ATHLET for safety assessment of (very) Small and Micro Reactors. J. Phys. Conf. Ser. http://dx.doi.org/10.1088/1742-6596/1689/1/012008.

Cai, L., 2014. Condensation and homogenization of cross sections for the deterministic transport codes with Monte Carlo method: Application to the GEN IV fast neutron reactors (Ph.D. thesis). Université Paris Sud, Paris.

Douglas O'Dell, R., Brinkley, F.W., Marr, D.R., 1982. User's manual for ONEDANT: A code package for one-dimensional, diffusion-accelerated, neutral-particle transport. Los Alamos National Laboratory.

Dürigen, S., 2013. Neutron Transport in Hexagonal Reactor Cores Modeled by Trigonal-Geometry Diffusion and Simplified P3 Nodal Methods (Ph.D. thesis). Karlsruhe Institute of Technology, Karlsruhe, URL https://inis.iaea.org/collection/NCLCollectionStore/_Public/48/022/48022303.pdf.

Hébert, A., 2010. Mixed-dual implementations of the simplified method. Ann. Nucl. Energy 37 (4), 498–511. http://dx.doi.org/10.1016/j.anucene.2010.01.006.

Hébert, A., Benoist, P., 1991. A consistent technique for the global homogenization of a pressurized water reactor assembly. Nucl. Sci. Eng. 109 (4), 360–372. http://dx.doi.org/10.13182/NSE109-360.

Henry, R., Seubert, A., Bousquet, J., 2021. Analysis of the X2 VVER-1000 benchmark with FENNECS. In: Proceedings of NENE 2021 conference. Nuclear Society of Slovenia.

Lin, C.-S., Yang, W.S., 2020. An assessment of the applicability of multigroup cross sections generated with Monte Carlo method for fast reactor analysis. Nucl. Eng. Technol. 52 (12), 2733–2742. http://dx.doi.org/10.1016/j.net.2020.05.029.

lo Muzio, S., Seubert, A., 2022a. Implementation and validation of the steady state SP3 approximation in the GRS FENNECS code. In: Proceedings of NENE 2022. Nuclear Society of Slovenia.

lo Muzio, S., Seubert, A., 2022b. Verification of the SP3 solver in FENNECS with C5G7 test cases using HELIOS cross sections. In: ETSON Conference 2022 in Munich. ETSON.

lo Muzio, S., Seubert, A., 2023. Validation of the FENNECS SP3 solver with control Rod Insertion Simulations of the ESFR using Serpent cross sections. In: Proceedings M&C 2023 - the International Conference on Mathematics and Computational Methods Applied to Nuclear Science and Engineering.

lo Muzio, S., Seubert, 2024. Implementation of the steady state simplified P3 (SP3) transport solver in the finite element neutronic code FENNECS, Part 1: Theory. Ann. Nucl. Energy 200, http://dx.doi.org/10.1016/j.anucene.2023.110303.

lo Muzio, S., Seubert, A., Liancheng, G., 2022. Simulation of CEFR neutronic start-up tests with FENNECS and coupled pin-by-pin model of a CEFR subassembly. In: KernD (Ed.), Proceedings of Young Scientist Workshop At Kerntechnik 2022.

Ragab Fayez, M., 2016. Approximation of the Neutron Diffusion Equation on Hexagonal Geometries Using a h-p finite element method (Ph.D. thesis). Universitat Politècnica de València, Valencia, http://dx.doi.org/10.4995/Thesis/10251/65353.

Rineiski, A., Meriot, C., Coquelet, C., Krepel, J., Fridman, E., Mikityuk, K., 2018. In: European Commission (Ed.), Specification of the New Core Safety Measures. European Commission.

Schaffrath, A., Wielenberg, A., Kilger, R., Seubert, A., 2021. SMRs — overview, international developments, safety features and the GRS simulation chain. Front. Energy 15 (4), 793–809. http://dx.doi.org/10.1007/s11708-021-0751-2.

Seubert, A., Bousquet, J., Henry, R., 2021. Recent advances of the fennecs neutronics code for safety assessment of (V)SMR, generation IV and other innovative concepts. In: The International Conference on Mathematics and Computational Methods Applied to Nuclear Science and Engineering.

Seubert, A., Velkov, K., Langenbuch, S., 2008. The time-dependent 3D discrete ordinates code TORT-TD with thermal-hydraulic feedback by ATHLET models. In: International Conference on the Physics of Reactors Nuclear Power: A Sustainable Resource. Casino-Kursaal Conference Center, Interlaken, Switzerland, September 14-19, 2008.

Smith, M.A., Lewis, E.E., Na, B.-C., 2003. Benchmark on Deterministic Transport Calculations Without Spatial Homogenisation. A 2-D/3-D MOX Fuel Assembly Benchmark, OECD Nuclear Energy Agency, ISBN: 92-64-02139-6.

4.2 The 2D Cartesian planar benchmark and the Hébert benchmark

In [38], for some quantities, a slightly different notation was used compared to [41] and the rest of this work. The matrices B^e, C^e, and H^e are indicated in [38] with d, c, and p, respectively. The index h, indicating the face of the element, is addressed in [41] with η.

31st International Conference Nuclear Energy for New Europe
NENE 2022 September 12-15 PORTOROŽ SLOVENIA

Implementation and Validation of the Steady State SP_3 Approximation in the GRS Code FENNECS

Silvia lo Muzio
Gesellschaft für Anlagen- und Reaktorsicherheit (GRS) gGmbH
Boltzmannstr. 14
85748 Garching near Munich, Germany
silvia.lomuzio@grs.de

Armin Seubert
Gesellschaft für Anlagen- und Reaktorsicherheit (GRS) gGmbH
Boltzmannstr. 14
85748 Garching near Munich, Germany
armin.seubert@grs.de

ABSTRACT

From the worldwide growing interest in Small Modular Reactors (SMRs) and Micro Modular Reactors (MMRs), it arises the necessity to employ a proper neutronic calculation tool for their safety assessment. Most of the deterministic neutronic solvers rely on the diffusion approximation that is derived assuming isotropic scattering, low probability of neutron absorption compared to scattering, as well as a weakly varying neutron flux in space. This last assumption may not hold for small cores, like the ones of SMRs and MMRs: here, due to their reduced size and often their heterogeneity, high neutron flux gradients are present. An alternative to the use of the diffusion equation is the application of the third order Simplified Spherical Harmonics (SP_3) approximation of the neutron transport equation, which is expected to perform better for SMRs and MMRs.

For this reason, the Finite ElemeNt NeutroniCS (FENNECS) code, currently under development at GRS, which already provides a diffusion solver, was expanded by a steady state SP_3 solver. FENNECS offers a high geometrical flexibility, which is essential to model complex systems like SMRs and MMRs.

In this paper, starting from the transport equation, the steady state SP_3 approximation of the neutron transport equation is derived. Then, in order to implement the SP_3 equations in the FENNECS code, which is based on the Finite Element Method, these are cast into the Galerkin (weak) form. Finally, based on benchmark exercises, the correct functionality of the SP_3 solver implemented in FENNECS is shown.

1 INTRODUCTION

The neutron transport equation describes the neutron population in a medium. Here, taking into account the spatial as well as the angular dependency, the neutrons sinks and sources are described. On one hand, thanks to its exact description of the phenomena, very accurate results can be obtained. On the other hand, to solve the transport equation using deterministic or with Monte Carlo codes is computationally expensive in both cases. This problem can be solved, by applying approximations [1–4].

The most commonly used approximation of the transport equation is diffusion theory. This is based on three assumptions, which are isotropic scattering, a very small probability of absorption compared to scattering ($\Sigma_a \ll \Sigma_s$), and a weak variation of the neutron flux in space (in particular, the neutron current is proportional to the flux gradient according to Fick's law). The first criterion is fulfilled only by heavy nuclei. The second one is not true for fuel and control materials. Finally, the last assumption is satisfied for homogeneous and large media (with respect to the mean free path length $\bar{\lambda}_n$) at a distance of a few $\bar{\lambda}_n$ away from the boundary. Consequently, this approximation may not be applicable near material interfaces and for small cores, like (v)SMR and MMR [5–7].

For the safety assessment of these systems, an appropriate approximation to the neutron transport equation is essential. One suited candidate is the Simplified Spherical Harmonics approximation of third order, or SP_3. This can be derived expanding the angular terms of the transport equation with Legendre's polynomials, even in 3D, without performing the transition to spherical harmonics [4,8,9].

In order to model (v)SMR and MMR, the Finite ElemeNt NeutroniCS (FENNECS) code, outlined in section 2, must be extended by an SP_3 solver. For this reason, in section 3, the steady state SP_3 approximation in the Galerkin (weak) form, as it is already used for the FENNECS diffusion solver, is derived. Finally, in section 4, validation with benchmark exercises is performed.

2 FENNECS

FENNECS was recently developed at Gesellschaft für Anlagen- und Reaktorsicherheit gGmbH (GRS). Originally, it was a 3D few group finite element based diffusion code, capable to model steady state as well as transient core configurations. FENNECS is based on the Galerkin weighted residual approach, where upright triangular prisms with linear basis functions are used as spatial elements. Due to its geometrical flexibility, it is capable to model complex and irregular geometries, like most often occurring in various (v)SMR and MMR concepts. The spatial meshing is performed by the Python Enhanced Meshing Tool with YAML input, PEMTY. To run the calculations, cross section libraries in NEMTAB format are applied [10,11].

3 DERIVATION OF THE STEADY STATE SP_3 APPROXIMATION IN THE GALERKIN FORMALISM

The SP_3 approximation is derived from the one dimensional transport equation, which can be found in [6] and [12], having G discretized energy groups, as in [13], where $g \epsilon (1, \dots, G)$ and $g = 1$ is the lowest energy group. Firstly, to obtain the Spherical Harmonics approximation of third order (P_3), the variables showing an angular dependency are expanded with Legendre polynomials up to the third order, as in [12]. Similarly to [13], also here it is assumed that higher order scattering between energy groups is neglected. Hence, between different energy groups only the zeroth order scattering is considered. By doing a first step towards the spatial finite elements discretization, it is assumed that all nuclear data are constant within a finite element e. From the one-dimensional P_3 equations, the three-dimensional SP_3 approximation can be obtained by keeping the Legendre expansions, by simply replacing the double derivative with the Laplacian and the x -dependency with $\vec{r}$. For the even order neutron fluxes, hence ϕ_0, which is the scalar flux, and ϕ_2, the following notations are used:

$$F_{0,g}(\vec{r}) = \phi_{0,g}(\vec{r}) + 2\phi_{2,g}(\vec{r}) \tag{1}$$

$$F_{1,g}(\vec{r}) = \phi_{2,g}(\vec{r}). \tag{2}$$

Finally, the following formulation of the SP_3 system of equations is obtained:

$$-\Delta F_{0,g}(\vec{r})D^e_{0,g} + F_{0,g}(\vec{r})\left(\Sigma^e_{t,g} - \Sigma^e_{s,0,gg}\right) - 2F_{1,g}(\vec{r})\left(\Sigma^e_{t,g} - \Sigma^e_{s,0,gg}\right) = S_{0,g}(\vec{r}), \quad \forall\, \vec{r} \in e \tag{3}$$

$$-\frac{2}{3}F_{0,g}(\vec{r})\left(\Sigma^e_{t,g} - \Sigma^e_{s,0,gg}\right) - \Delta F_{1,g}(\vec{r})D^e_{1,g} + F_{1,g}(\vec{r})\left(\frac{4}{3}\left(\Sigma^e_{t,g} - \Sigma^e_{s,0,gg}\right) + \frac{5}{3}\left(\Sigma^e_{t,g} - \Sigma^e_{s,2,gg}\right)\right) = -\frac{2}{3}S_{0,g}(\vec{r}), \forall\, \vec{r} \in e \tag{4}$$

where

$$S_{0,g}(\vec{r}) = \frac{\chi_g}{k_{eff}}\sum_{g'=1}^{G}\vartheta\Sigma^e_{f,g'}\left(F_{0,g'}(\vec{r}) - 2F_{1,g'}(\vec{r})\right) + \sum_{g'=1,g'\neq g}^{G}\Sigma^e_{s,0,g'g}\left(F_{0,g'}(\vec{r}) - 2F_{1,g'}(\vec{r})\right), \forall\, \vec{r} \in e. \tag{5}$$

Here, the variables with the apostrophe describe the neutron state after the scattering event. ϑ is the fission yield and Σ_t, Σ_s and Σ_f are the total, scattering and fission macroscopic cross sections, respectively. In Eq. (5), χ_g and k_{eff} are the group fission spectrum and the effective multiplication factor, respectively. Furthermore, in Eq. (3) and (4), $D_{0,g}$ and $D_{1,g}$ are the zeroth and first order diffusion coefficients, defined as

$$D_{0,g} = \frac{1}{3\left(\Sigma_{t,g} - \Sigma_{s,1,gg}\right)} \tag{6}$$

$$D_{1,g} = \frac{3}{7\left(\Sigma_{t,g} - \Sigma_{s,3,gg}\right)}. \tag{7}$$

The Galerkin (weak) form can be obtained following the approach described in [14]. Therefore, firstly, considering that in FENNECS the discretization is performed with upright triangular prisms as finite elements, Eq. (3) and (4) must be multiplied by the test functions $\varphi^T(\vec{r}) = (\varphi_1(\vec{r}), \quad \dots, \quad \varphi_6(\vec{r}))^T$. Secondly, integration over the volume Γ^e of the triangular prismatic finite element e is performed. Thirdly, the Gauss theorem is applied to transform second order to first order spatial derivatives. Then, $F_{0,g}$ and $F_{1,g}$ must be expanded in terms of the basis functions as

$$F_{k,g}(\vec{r}) = \sum_{j=1}^{6}\varphi_j(\vec{r})f^e_{k,g,j} = \begin{pmatrix}\varphi_1(\vec{r})\\ \vdots \\ \varphi_6(\vec{r})\end{pmatrix}\cdot\begin{pmatrix}f^e_{k,g,1}\\ \vdots \\ f^e_{k,g,6}\end{pmatrix} = \vec{\varphi}(\vec{r})\overrightarrow{f^e_{k,g}}, \forall\, \vec{r} \in e, k = 0,1 \tag{8}$$

Consequently, the Galerkin formulation of the SP_3 approximation takes the following form:

$$\left[D_{0,g}^{e}\mathrm{d}+\left(\Sigma_{t,g}^{e}-\Sigma_{s,0,gg}^{e}\right)c-\sum_{h=1}^{5}\left(-\frac{\beta_{0,h}^{e}}{\gamma_{h}^{e}}\right)p\right]\overrightarrow{f_{0,g}^{e}}=$$
$$c\left[\frac{\chi_g}{k_{eff}}\sum_{g'=1}^{G}\vartheta\Sigma_{f,g'}^{e}\left(\overrightarrow{f_{0,g'}^{e}}-2\overrightarrow{f_{1,g'}^{e}}\right)+\sum_{g'=1,g'\neq g}^{G}\Sigma_{s,0,g'g}^{e}\left(\overrightarrow{f_{0,g'}^{e}}-2\overrightarrow{f_{1,g'}^{e}}\right)\right]+ \quad (9)$$
$$\left[2\left(\Sigma_{t,g}^{e}-\Sigma_{s,0,gg}^{e}\right)c+\sum_{h=1}^{5}\left(-\frac{\alpha_{0,h}^{e}}{\gamma_{h}^{e}}\right)p\right]\overrightarrow{f_{1,g}^{e}}$$

$$\left\{D_{1,g}^{e}\mathrm{d}+\left[\frac{4}{3}\left(\Sigma_{t,g}^{e}-\Sigma_{s,0,gg}^{e}\right)+\frac{5}{3}\left(\Sigma_{t,g}^{e}-\Sigma_{s,2,gg}^{e}\right)\right]c-\sum_{h=1}^{5}\left(-\frac{\alpha_{1,h}^{e}}{\gamma_{h}^{e}}\right)p\right\}\overrightarrow{f_{1,g}^{e}}=$$
$$-\frac{2}{3}c\left[\frac{\chi_g}{k_{eff}}\sum_{g'=1}^{G}\vartheta\Sigma_{f,g'}^{e}\left(\overrightarrow{f_{0,g'}^{e}}-2\overrightarrow{f_{1,g'}^{e}}\right)+\sum_{g'=1,g'\neq g}^{G}\Sigma_{s,0,g'g}^{e}\left(\overrightarrow{f_{0,g'}^{e}}-2\overrightarrow{f_{1,g'}^{e}}\right)\right]+ \quad (10)$$
$$\left[\frac{2}{3}\left(\Sigma_{t,g}^{e}-\Sigma_{s,0,gg}^{e}\right)c+\sum_{h=1}^{5}\left(-\frac{\beta_{1,h}^{e}}{\gamma_{h}^{e}}\right)p\right]\overrightarrow{f_{0,g}^{e}}$$

where

$$d=\int_{\Gamma^e}\nabla\varphi(\vec{r})\nabla\varphi^{T}(\vec{r})\,dV,\ \forall\,\vec{r}\in e \quad (11)$$

$$c=\int_{\Gamma^e}\varphi_i(\vec{r})\varphi_j(\vec{r})\,dV,\ \forall\,\vec{r}\in e \quad (12)$$

$$p=\int_{\partial\Gamma^e}\nabla\varphi(\vec{r})\varphi^{T}(\vec{r})dA,\ \forall\,\vec{r}\in e. \quad (13)$$

The terms $\sum_{h=1}^{5}\left(-\frac{\beta_{0,h}^{e}}{\gamma_{h}^{e}}\right)$, $\sum_{h=1}^{5}\left(-\frac{\alpha_{0,h}^{e}}{\gamma_{h}^{e}}\right)$, $\sum_{h=1}^{5}\left(-\frac{\alpha_{1,h}^{e}}{\gamma_{h}^{e}}\right)$, and $\sum_{h=1}^{5}\left(-\frac{\beta_{1,h}^{e}}{\gamma_{h}^{e}}\right)$ describe the boundary condition at the five faces of the finite element and their values are listed in Table 1.

Table 1: Values for $1/\gamma_h^e$, $\beta_{0,h}^e$, $\beta_{1,h}^e$, $\alpha_{0,h}^e$ and $\alpha_{1,h}^e$ depending on the boundary condition.

	$1/\gamma_h^e$	$\beta_{0,h}^e$	$\beta_{1,h}^e$	$\alpha_{0,h}^e$	$\alpha_{1,h}^e$
Interface boundary condition: $\partial\Gamma_h^e\in\partial\Gamma^I$	0	0	0	0	0
Vacuum boundary condition: $\partial\Gamma_h^e\in\partial\Gamma^V$	1/8	4	−1	−3	7
Reflective boundary condition: $\partial\Gamma_h^e\in\partial\Gamma^R$	1	0	0	0	0
Zero flux boundary condition: $\partial\Gamma_h^e\in\partial\Gamma^{ZF}$	∞	4	−1	−3	7

4 VALIDATION WITH ACADEMIC EXERCISES

The first part of the solver validation process consists in testing it on simple models. For this reason, academic exercises are particularly suited. Two examples will be analysed here. The first one is constituted by quadratic fuel assemblies and the second one by hexagonal ones.

4.1 Cartesian benchmark

The geometry description and cross sections of the Cartesian benchmark are given in [15], where this is modelled with the SP_3 solver of TRIVAC, a modular neutronic code for design applications and fuel management [15,16]. This benchmark is a small two-dimensional core with vacuum boundary conditions, having assemblies with a pitch of 40 cm, made of fuel, reflector and a pure absorber that are disposed concentrically, as depicted in Figure 1. Due to its small size and the strong variation between the material properties, it is particularly suited to show the limitations of the diffusion theory and to demonstrate the performance of the SP_3.

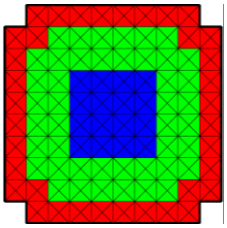

Figure 1: Mesh of the Cartesian benchmark with 4 radial elements per assembly. The blue, green, and red regions are composed by fuel, reflector, and pure absorber, respectively. The thick black lines represent the vacuum boundary condition.

The calculations were performed with the SP_3 and the diffusion solver of FENNECS with different meshes. The obtained multiplication factors are compared to the ones from the TRIVAC SP_3 solver based on the Raviart–Thomas zeroth order (RT0) solution with analytical integration (AI) and with Gauss-Legendre quadrature (GLQ). As in [15], the reference used is $k_{eff} = 0.992160$, which was calculated by the TRIVAC SP_5 solver based on the Raviart–Thomas second order (RT2) solution with GLQ and 16 radial elements per assembly.

As shown in Table 2, the discrepancies between the multiplication factors of TRIVAC and FENNECS and the reference value, were evaluated. In the case of the FENNECS diffusion solver, the disagreements are striking: for 4 as well as for 16 radial elements per assembly the difference is above 4300 pcm. This result clearly shows that the diffusion approximation is not well suited to model such very small cores. However, these high discrepancies should be further investigated. If the cross sections would have been generated with Serpent, and not already given, it would have been possible to apply the superhomogenization (SPH) method [17], from which an improvement of the results is expected.

Table 2: Multiplication factors for the Cartesian benchmark from FENNECS and TRIVAC with their deviations from TRIVAC SP_5 RT2 GLQ with 16 radial elements per assembly.

Program	Solver	Radial elements per assembly	k_{eff}	Difference with the reference (pcm)
FENNECS	Diffusion	4	0.94575	-4946
		16	0.95129	-4330
	SP_3	4	0.98079	-1168
		16	0.98793	-432
		36	0.98960	-261
		64	0.99024	-195
		144	0.99073	-145
		400	0.99099	-119
		2116	0.99112	-106
TRIVAC RT0 AI	SP_3	4	0.995780	366
		16	0.992535	38
		36	0.991794	-37
TRIVAC RT0 GLQ	SP_3	4	0.989783	-242
		16	0.990796	-139
		36	0.990989	-119

The results from the FENNECS SP_3 solver show smaller discrepancies and the agreement with the reference drastically increases by reducing the mesh size: with 2116 radial elements per assembly the discrepancy is only 106 pcm. At this point, mesh refinement does not affect the k_{eff}. On the contrary, increasing the number of elements from 4 to 16, leads to significant improvements: the discrepancy is halved. Regarding the better agreement of TRIVAC with the reference, this can be explained by the use of AI or GLQ, hence more accurate methods.

4.2 Hébert benchmark

The Hébert benchmark, depicted in Figure 2, is very similar to the exercise above. The main difference are the hexagonal assemblies, having a pitch of 32.9 cm. Here, the comparison is performed between results calculated by FENNECS and the ones from the SP_3 solvers of DYN3D and of TRIVAC, which were taken from [13], together with the cross sections.

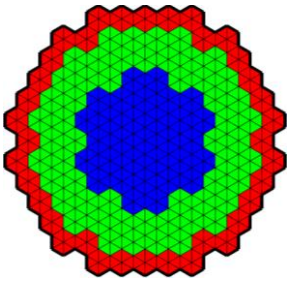

Figure 2: Mesh of the Hébert benchmark with 6 radial elements per assembly. The blue, green, and red regions are composed by fuel, reflector, and pure absorber, respectively. The thick black lines represent the vacuum boundary condition.

Table 3 shows the multiplication factors and their deviations from the reference, which is the TRIVAC SP_3 solver, where k_{eff} = 1.000332. Here, it can be observed that the discrepancies between the k_{eff} from the FENNECS diffusion solver and the reference are again above 4300 pcm. Also here, if Serpent generated cross section would have been used, the SPH method could have been applied, from which a decrease of the discrepancy is expected.

Table 3: Multiplication factors for the Hébert benchmark from FENNECS and DYN3D and their deviation from TRIVAC SP_3 reference.

Program	Solver	Radial elements per assembly	k_{eff}	Difference with the reference (pcm)
FENNECS	Diffusion	6	0.95641	4590.9
		24	0.95845	4368.3
	SP_3	6	0.99533	502.4
		24	0.99861	172.4
		96	0.99975	58.2
		384	1.00009	24.2
		1536	1.00019	14.2
		2166	1.00021	12.2
DYN3D	SP_3	6	1.001100	-76.7
		24	1.000085	24.7
		96	0.999939	39.3
		384	1.000039	29.3
		1536	1.000156	17.6
		6144	1.000238	9.4

For both SP_3 solvers, the discrepancies are drastically smaller: the difference between the reference and the k_{eff} from the FENNECS SP_3 solver with 6 radial elements per assembly is only 502.4 pcm, whereas for the SP_3 solver of DYN3D it is -76.7 pcm, hence it is lower. However, refining the mesh, the k_{eff} of FENNECS and DYN3D approach closer the reference. In particular, with the SP_3 solver of FENNECS, a larger improvement can be observed compared to DYN3D, such that starting from 384 radial elements per assembly, the k_{eff} from FENNECS SP_3 is closer to the reference, compared to DYN3D. Therefore, the methodology of FENNECS SP_3 shows a stronger dependency on the mesh, compared to the one of DYN3D.

For this benchmark, also the normalized flux distributions from the SP_3 solvers of FENNECS and DYN3D are evaluated and compared to the TRIVAC SP_3 reference. In Table 4, the root mean squared (RMS) and the maximum and minimum deviation for the distributions of the deviations from the reference of the normalized neutron flux can be found. Here, it can be observed that with a small number of radial subdivisions the normalized flux distributions from DYN3D are closer to the reference, compared to FENNECS, as seen from the RMS and the maximum deviations and as it can observed in Figure 3. For both solvers, the RMS and the maximum errors decrease with the mesh refinement. However, as it was the case for the k_{eff}, this decrease is stronger for FENNECS: starting from 96 radial elements per assembly, the SP_3 solver of FENNECS yields a normalized flux distribution closer to TRIVAC, compared to DYN3D, as stated by the RMS and the maximum deviation and as it can be seen in Figure 4.

Table 4: RMS (%), maximum and minimum deviations of the normalized neutron flux distributions, depending on mesh, with respect to the reference.

Radial elements per assembly	RMS (%)		Maximum (%)		Minimum (%)	
	FENNECS SP_3	DYN3D SP_3	FENNECS SP_3	DYN3D SP_3	FENNECS SP_3	DYN3D SP_3
6	4.1	1.7	8.3	-2.5	0.2	0.0
24	1.5	1.1	3.2	-1.9	0.0	0.0
96	0.5	0.6	1.0	-1.4	0.0	0.1
1536	0.1	0.2	-0.3	-0.5	0.0	0.0

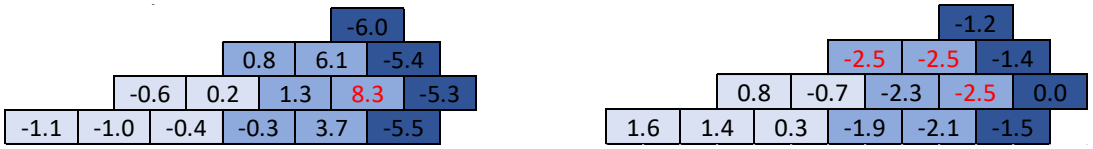

Figure 3: Deviations (%) from the reference of the normalized neutron flux distributions for the SP_3 solvers of FENNECS (left) and DYN3D (right) with 6 radial elements per assembly. The red numbers are the maximum deviations.

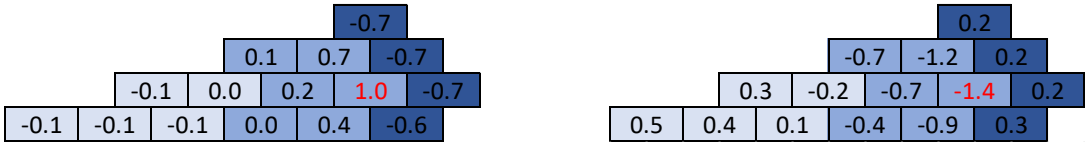

Figure 4: Deviations (%) from the reference of the normalized neutron flux distributions for the SP_3 solvers of FENNECS (left) and DYN3D (right) with 96 radial elements per assembly. The red numbers are the maximum deviations.

5 CONCLUSIONS

In this work, starting from neutron transport theory, the equations of the SP_3 approximation in the Galerkin formalism were derived. The equations obtained were used to implement an SP_3 solver in the deterministic finite element neutronic code FENNECS.

The functionality of the solver was demonstrated with the Cartesian and with the Hébert benchmarks. In the first one, the k_{eff} was used to prove the superiority of the SP_3 approximation with respect to diffusion theory for a small heterogeneous core. In the second one, the k_{eff} as well as the normalized flux distributions of FENNECS and DYN3D were compared to TRIVAC SP_3. Here, it could be observed, that the SP_3 solver of DYN3D yields better results for coarse meshes. However, a mesh refinement leads to a significant improvement of the results from the FENNECS SP_3 solver, such that for a finer meshes these are closer to the

reference compared to the ones of DYN3D. In the near future, the verification and validation work will be continued on more realistic test cases, e.g. PWR fuel assemblies and SFR cores.

ACKNOWLEDGMENTS

This work was supported by the German Federal Ministry for the Environment, Nature Conservation, Nuclear Safety and Consumer Protection.

6 REFERENCES

[1] E. Science, Deterministic Numerical Methods for Unstructured-Mesh Neutron Transport Calculation, Elsevier Science & Technology, San Diego, 2021.
[2] A.M.G. Cox, S.C. Harris, E.L. Horton, A.E. Kyprianou, Multi-species Neutron Transport Equation, Journal of Statistical Physics 176 (2019) 425–455.
[3] P.S. Brantley, E.W. Larsen, The Simplified P3 Approximation, Nuclear Science and Engineering 134 (2000) 1–21.
[4] A.V. Avvakumov, V.F. Strizhov, P.N. Vabishchevich, A.O. Vasilev, Numerical modeling of neutron transport in SP3 approximation by finite element method, http://arxiv.org/pdf/1903.11502v1.
[5] Ö. Ege, V. Öztürk, A. Bülbül, Diffusion Approximation to Neutron Transport Equation with First Kind of Chebyshev Polynomials, SDU Journal of Science 2015 (2015) 92–96.
[6] W.M. Stacey, Nuclear reactor physics, 2. ed., completely rev. and enlarged., WILEY-VCH, Weinheim, 2007.
[7] S. Marguet, The Physics of Nuclear Reactors, Springer International Publishing, 2018.
[8] Y. Wu, Neutronics of Advanced Nuclear Systems, Springer, Singapore, 2019.
[9] Q.-Q. Pan, T.-F. Zhang, X.-J. Liu, H. He, K. Wang, SP3-coupled global variance reduction method based on RMC code, NUCL SCI TECH 32 (2021).
[10] J. Bousquet, A. Seubert, R. Henry, New finite element neutron kinetics coupled code system FENNECS/ATHLET for safety assessment of (very) Small and Micro Reactors, J. Phys.: Conf. Ser. (2020).
[11] A. Seubert, J. Bousquet, R. Henry, RECENT ADVANCES OF THE FENNECS NEUTRONICS CODE FOR SAFETY ASSESSMENT OF (V)SMR, GENERATION IV AND OTHER INNOVATIVE CONCEPTS, in: The International Conference on Mathematics and Computational Methods Applied to Nuclear Science and Engineering: Proceedings, Raleigh, North Carolina, 2021.
[12] E.E. Lewis, W.F. Miller, Computational methods of neutron transport, Wiley, New York, 1984.
[13] S. Dürigen, Neutron Transport in Hexagonal Reactor Cores Modeled by Trigonal-Geometry Diffusion and Simplified P3 Nodal Methods (2013).
[14] A. Seubert, A 3-D FINITE ELEMENT FEW-GROUP DIFFUSION CODE AND ITS AP-PLICATION TO GENERATION IV REACTOR CONCEPTS, in: Proceedings of PHYSOR 2020, Cambridge, United Kingdom, 2020.
[15] A. Hébert, Mixed-dual implementations of the simplified method, Annals of Nuclear Energy 37 (2010) 498–511.
[16] A. Hebert, Trivac: A Modular Diffusion Code for Fuel Management and Design Applications, Nuclear journal of Canada (1987) 325–331.
[17] A. Hebert, A Reformulation of the Transport-Transport SPH Equivalence Technique, Proceedings 7th International Conference on Modelling and Simulation in Nuclear Science and Engineering (7ICMSNSE), Ottawa, Ontario, Canada (2015).

4.3 C5G7 test cases

Verification of the SP3 Solver in FENNECS with C5G7 Test Cases using HELIOS Cross Sections

Silvia Io Muzio, Armin Seubert**

*Gesellschaft für Anlagen- und Reaktorsicherheit (GRS) gGmbH,
Boltzmannstr. 14, 85748 Garching near Munich, Germany

Abstract:

Due to the worldwide growing interest in Small Modular Reactors (SMRs) and Micro Modular Reactors (MMRs), the development of tools for their safety assessment is of particular interest. These reactors have compact and complex geometries with strong neutron flux gradients. One possibility could be to use Monte Carlo methods, which require an enormous resources demand especially for transients, on the contrary to most deterministic codes. For this reason, the Finite ElemeNt NeutroniCS (FENNECS) deterministic code is particularly suited due to its geometric flexibility. FENNECS provides a solver based on the diffusion approximation of the transport equation. However, this approximation may not hold for small and heterogeneous configurations. To overcome the limitations of diffusion theory, an option are deterministic transport codes, but they also may be computationally expensive. An adequate possible solution is the third order Simplified Spherical Harmonics (SP_3) approximation of the transport equation.

A short summary of the theoretical derivation of the SP_3 in the finite elements formalism and its implementation into FENNECS will be given. To carry out validation and verification, the C5G7 benchmark is taken as example. Macroscopic pin cell homogenized cross sections and pin power distributions were generated with HELIOS-1.12 for the UO_2 and MOX assemblies. These cross sections were verified with the transport code TORT-TD and used to simulate the same geometries with the diffusion as well as with the SP_3 solver of FENNECS. Pin power distributions and multiplication factors obtained by the SP_3 solver satisfactorily agree with the respective HELIOS results.

1 INTRODUCTION

The increasing interest in small modular reactors (SMRs) and micro modular reactors (MMRs) requires adequate tools for their safety assessment, either Monte Carlo or deterministic. The first category offers a high geometrical flexibility, which is necessary to model the complex geometries of SMRs and MMRs. However, their biggest disadvantages are not sufficient maturity for transient applications and a large requirement of computational resources, especially for transients, making them not suited for routine applications. On the contrary, deterministic codes do not suffer from this limitation, allowing them to perform transient calculations more efficiently [1–3].

Neutronic codes can be also categorized depending on the physical and mathematical model behind them. Here, one possibility is to use codes relying on transport theory: the transport equation accurately describes the angular neutron flux in a medium, taking into account neutron sinks and sources. However, this is formulated with seven independent variables (five for the space-angular dependency, one for energy and one for time). Therefore, to solve it, a considerable amount of resources is required. A solution to this problem is to apply approximations to the transport equation [4–7].

The most common approximation of the transport equation is diffusion theory, which consists in assuming isotropic scattering, only low neutron absorption compared to scattering, and low variation of the neutron flux in space. The first assumption holds only for heavy nuclei.

The second one is not fulfilled by fuel and control materials. Finally, the last consideration can be applied only to large (with respect to the mean free path) and homogenous media. Even in this case, this assumption holds only a few mean free paths away from the medium boundary. Thus, diffusion theory may not be suited to model the compact and inhomogeneous cores of SMRs and MMRs [8–10].

Therefore, an adequate approximation of the transport equation must be found to perform the safety assessment of these systems. A possible candidate for this task is the third order Simplified Spherical Harmonics approximation, or SP_3, which is more accurate than diffusion theory. This approximation consists in expanding the angular dependency of the transport equation with Legendre polynomials, even for three-dimensional models, without the necessity to replace them with spherical harmonics [4,11,12].

For this reason, the Finite ElemeNt NEutroniCS (FENNECS) code, described in section 2, was extended by a steady state SP_3 solver and the mathematical model behind it is briefly described in section 3. Within the validation process, the UO_2 and MOX fuel assemblies specified by the C5G7 benchmark were used. As explained in section 4, the single fuel assemblies were modelled with HELIOS-1.12 to generate reference eigenvalues and pin power distributions and the pin cell-homogenized cross sections libraries, which were validated with the transport code TORT-TD [13]. Finally, with the obtained libraries, the UO_2 and MOX fuel assemblies were modelled with FENNECS.

2 FENNECS

The code FENNECS was recently developed at Gesellschaft für Anlagen- und Reaktorsicherheit (GRS) gGmbH. Initially, it was a three dimensional few-group diffusion code capable to model steady state as well as transient core configurations. FENNECS relies on the continuous Galerkin weighted residual approach using upright triangular finite elements with linear basis functions as spatial elements. To run the calculations, cross-section libraries in NEMTAB format must be provided. Furthermore, the main advantage of the FENNECS code is its high geometrical flexibility, which is an essential requirement to model complex and irregular system, like most of the SMRs and MMRs [14,15].

3 MATHEMATICAL MODEL BEHIND THE SP_3 SOLVER OF FENNECS

The steady state SP_3 approximation is derived from the Spherical Harmonics approximation of third order (P_3), which consists in expanding the angular terms of the steady state one dimensional transport equation with Legendre polynomials up to the third order. The transition to the SP_3 approximation is performed by moving to 3D solely by replacing the double derivative with the Laplacian operator and without the necessity to replace the Legendre polynomials with spherical harmonics [10,16–18].

As mentioned in section 2, FENNECS relies on the Galerkin finite element approach. Therefore, the steady state SP_3 equations must be casted into the Galerkin formalism, as it is explained in [19].

4 C5G7 TEST CASES

The geometry specifications of the C5G7 fuel assemblies were taken from [20]. The geometry of the C5G7 benchmark consists of a minicore made of four fuel assemblies in total, where two of them are made of UO_2 and the remaining two of MOX.

In this work, single-assembly models of the two types of fuel assemblies were considered using reflective boundary conditions. The calculations were performed firstly with HELIOS-1.12, using the collision probabilities solver, from which the reference values for the effective multiplication factors and for the pin power distribution, together with the pin cell-wise homogenized macroscopic cross-section libraries were obtained. The libraries were validated with the deterministic transport code TORT-TD. Then, using the validated cross sections,

calculations with the diffusion as well as with the SP_3 solver of FENNECS using various mesh refinements (4 and 16 radial elements per pin cell) were performed. Finally, the multiplication factors as well as the normalized power distributions calculated by FENNECS were compared with the HELIOS reference calculations results. In particular, in the case of the multiplication factors, the analysis was performed calculating the reactivity deviation from the refence, and for the normalized power distributions the root mean square (RMS) as well as the maximum and minimum value of the deviation for each pin was considered.

4.1 UO_2 fuel assembly

The multiplication factor calculated by HELIOS for the UO_2 fuel assembly, illustrated in Figure 1, is 1.32705 and this value is used as refence. As it can be observed in Table 1 and Table 2, for both FENNECS solvers, the discrepancies in the effective multiplication factors, as well as in the RMS and the maximum error of the power distribution, decrease with increasing number of radial elements per pin cell.

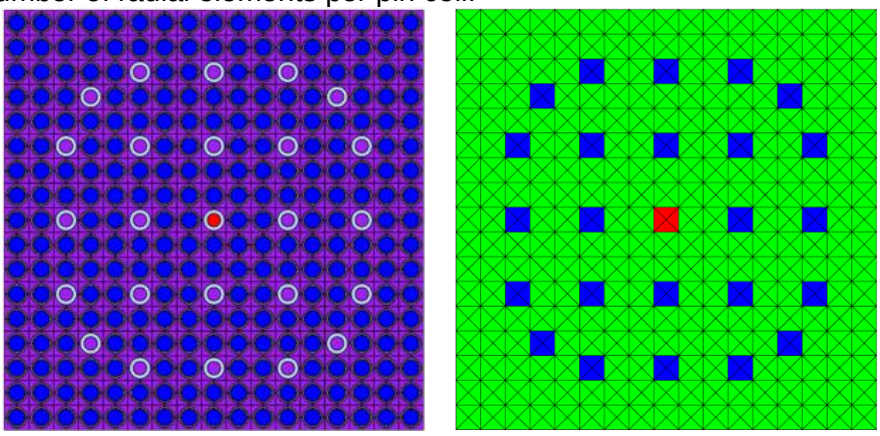

Figure 1: UO_2 fuel assembly (left) and its FENNECS model (right) of the C5G7 minicore with a mesh using 4 radial elements per pin cell. In the FENNECS model, the green cells contain UO_2 fuel pins. The blue cells contain the guide tubes and the central red cell is the fission chamber.

Table 1: Multiplication factors calculated with the diffusion and SP_3 solvers of FENNECS with 4 and 16 radial elements per pin cell and the respective deviations from the HELIOS reference for the UO_2 fuel assembly.

Radial elements per pin cell	**Solver**	**k_{eff} from FENNECS**	**Deviation from HELIOS (pcm)**
4	Diffusion	1.32821	66
	SP3	1.32798	53
16	Diffusion	1.32779	42
	SP3	1.32752	27

Table 2: RMS (%), maximum and minimum value of the deviation of the normalized power distribution with respect to the HELIOS reference for the UO_2 fuel assembly.

Radial elements per pin cell	**Solver**	**RMS**	**Maximum error**	**Minimum error**
4	Diffusion	0.54%	1.43%	-0.06%
	SP_3	0.52%	1.48%	-0.17%
16	Diffusion	0.25%	0.68%	0.08%
	SP_3	0.23%	0.55%	0.00%

With both meshes, the FENNECS SP_3 solver delivers an effective multiplication factor closer to HELIOS and a smaller RMS of the power distribution, compared to the diffusion calculation: with 16 radial elements per pin, for the SP_3 solver the discrepancy in the multiplication factor is only 27 pcm and the RMS 0.23%, proving also the correct implementation of the methodology. However, it should be noted that the difference between the results of the two solvers is very small: for the k_{eff}, with 4 and 16 radial elements per pin, this is only 13 pcm and 15 pcm, respectively, and 0.02% for the RMS with mesh sizes. This can be explained by the very homogeneous composition of the UO_2 of fuel assembly.

4.2 MOX fuel assembly

For the MOX fuel assembly, depicted in Figure 2, the reference k_{eff} obtained with HELIOS is 1.17632. Here, an increase in the discrepancy between the multiplication factor calculated by the FENNECS diffusion solver and the reference can be observed after the mesh refinement, as shown in Table 3. In the case of the SP_3 solver, the increase in the number of radial elements per pin cell does not signifyingly affect the k_{eff}, whose discrepancy from the HELIOS reference is only 51 pcm for both meshes. On the contrary, for the normalized power distribution, a strong decrease of the pin power RMS, minimum and maximum error can be observed when decreasing the mesh size: with 16 radial elements per pin cell, the RMS and maximum error obtained with the SP_3 solver are only 0.46 % and 1.00 %, respectively, as it can be seen in Table 4. Therefore, for both assemblies, the very small errors observed FENNECS SP_3 results prove, besides its correct implementation, also that the accuracy of this methodology is very close to transport codes.

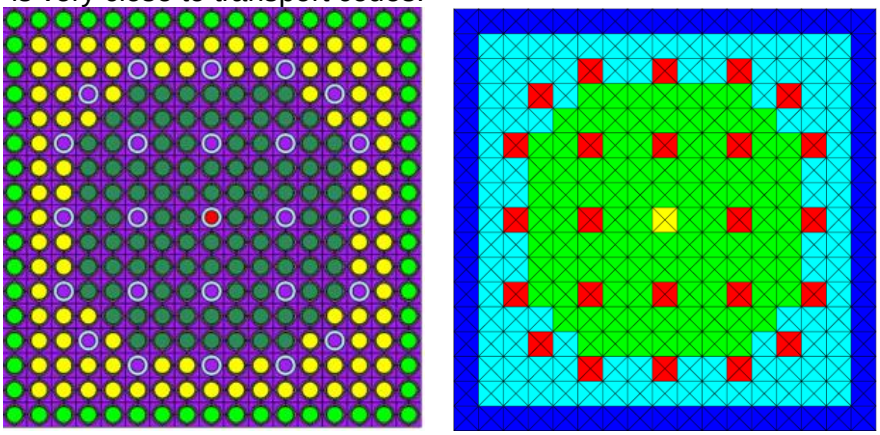

Figure 2: MOX fuel assembly (left) and its FENNECS model (right) of the C5G7 minicore with a mesh using 4 radial elements per pin cell. In the FENNECS model, the blue, light blue, and green cells contain fuel pins made of 4.3%, 7.0%, and 8.7% MOX, respectively. The red cells contain the guide tubes and the central yellow cell is the fission chamber.

Table 3: Multiplication factors calculated with the diffusion and SP_3 solvers of FENNECS with 4 and 16 radial elements per pin cell and the respective deviations from the HELIOS reference for the MOX fuel assembly.

Radial elements per pin cell	**Solver**	**k_{eff} from FENNECS**	**Deviation from HELIOS (pcm)**
4	Diffusion	1.17514	-85
	SP_3	1.17562	-51
16	Diffusion	1.17503	-93
	SP_3	1.17561	-51

Table 4: RMS (%) of the deviation of the normalized power distribution with respect to the HELIOS reference for the MOX fuel assembly.

Radial elements per pin cell	Solver	RMS	Maximum error	Minimum error
4	Diffusion	1.11%	1.95%	0.05%
	SP_3	0.88%	1.54%	0.05%
16	Diffusion	0.64%	1.44%	0.00%
	SP_3	0.46%	1.00%	-0.03%

Comparing the discrepancies in the multiplication factors as well as in the RMS of the normalized power distributions errors, it can be observed that the results from the SP_3 solver are closer to the HELIOS reference, compared to the ones calculated by diffusion theory. Compared to the UO_2 assembly, here the results from the FENNECS diffusion solver are more far away from the ones of the SP_3 solver as well as of HELIOS: for the multiplication factor and the RMS, the difference between the two FENNECS solvers ranges between 34 pcm and 42 pcm and between 0.18% and 0.23%, respectively, depending on the mesh. Furthermore, higher values for the deviation of the multiplication factor and the RMS are obtained, compared to the UO_2 fuel assembly: in particular, with the FENNECS diffusion solver and with 4 radial elements per pin, the RMS of the power distribution error is above 1%. These last two observations can be explained by the more heterogeneous composition of the MOX fuel assembly compared to the UO_2 assembly. Therefore, the limitations of the diffusion solver are emphasized and the higher accuracy of the SP_3 approximation, compared to diffusion theory, which was mentioned in section 1, is proven.

5 CONCLUSIONS

In this work, motivations for the importance of the development of an SP_3 solver in the FENNECS code were given. Furthermore, the theoretical derivation of the SP3 equation in the Galerkin formalism was briefly sketched.

Finally using the geometry of the C5G7 benchmark, single-assembly models of its UO_2 and MOX fuel assemblies were performed with HELIOS, which delivered the reference solutions and the cross sections that were used for the FENNECS calculations with the diffusion and SP_3 solver. Here, the multiplication factors and the normalized power distribution were analysed. For both quantities and both assemblies, the results of the SP_3 solver showed improvements against the diffusion approximation and a good agreement with the reference. In particular, in the case of the UO_2 fuel assembly, only small differences were observed between the results calculated with the diffusion and SP_3 solver, due to the homogenous configuration of this assembly. On the contrary, for the MOX assembly, the differences between the calculation results of these two solvers were larger, showing the expected benefit of the SP_3 approximation against diffusion theory in modelling heterogenous systems.

Therefore, the newly developed FENNECS SP_3 solver offers the possibility to model systems that could not be accurately modelled by the diffusion approximation, like SMRs and MMRs, with a precision that is very close to the one of a transport code. In the future, this research will be extended by modelling the whole C5G7 minicore, hence an even more realistic case.

6 ACKNOWLEDGMENTS

This work was supported by the German Federal Ministry for the Environment, Nature Conservation, Nuclear Safety and Consumer Protection.

7 REFERENCES

[1] Levon Ghasabyan, Use of Serpent Monte-Carlo code for development of 3D full-core models of Gen-IV fast-spectrum reactors and preparation of group constants for transient analyses with TRACE-PARCS coupled system (2013).

[2] R.L. Harrison, Introduction To Monte Carlo Simulation, AIP conference proceedings 1204 (2010) 17–21.

[3] J. Willert, C.T. Kelley, D.A. Knoll, H. Park, Hybrid Deterministic/Monte Carlo Neutronics, SIAM J. Sci. Comput. 35 (2013) S62-S83.

[4] A.V. Avvakumov, V.F. Strizhov, P.N. Vabishchevich, A.O. Vasilev, Numerical modeling of neutron transport in SP3 approximation by finite element method, http://arxiv.org/pdf/1903.11502v1.

[5] E. Science, Deterministic Numerical Methods for Unstructured-Mesh Neutron Transport Calculation, Elsevier Science & Technology, San Diego, 2021.

[6] A.M.G. Cox, S.C. Harris, E.L. Horton, A.E. Kyprianou, Multi-species Neutron Transport Equation, Journal of Statistical Physics 176 (2019) 425–455.

[7] E. Larsen, A New 2D-Transport, 1D-Diffusion Approximation of the Boltzmann Transport equation, 2013.

[8] Ö. Ege, V. Öztürk, A. Bülbül, Diffusion Approximation to Neutron Transport Equation with First Kind of Chebyshev Polynomials (2015).

[9] S. Marguet, The Physics of Nuclear Reactors, Springer International Publishing, 2018.

[10] W.M. Stacey, Nuclear reactor physics, 2. ed., completely rev. and enlarged., WILEY-VCH, Weinheim, 2007.

[11] Q.-Q. Pan, T.-F. Zhang, X.-J. Liu, H. He, K. Wang, SP3-coupled global variance reduction method based on RMC code, NUCL SCI TECH 32 (2021).

[12] Y. Wu, Neutronics of Advanced Nuclear Systems, Springer, Singapore, 2019.

[13] A. Seubert, K. Velkov, S. Langenbuch, The time-dependent 3D discrete ordinates code TORT-TD with thermal-hydraulic feedback by ATHLET models (2008).

[14] A. Seubert, J. Bousquet, R. Henry, RECENT ADVANCES OF THE FENNECS NEUTRONICS CODE FOR SAFETY ASSESSMENT OF (V)SMR, GENERATION IV AND OTHER INNOVATIVE CONCEPTS, in: The International Conference on Mathematics and Computational Methods Applied to Nuclear Science and Engineering: Proceedings, Raleigh, North Carolina, 2021.

[15] J. Bousquet, A. Seubert, R. Henry, New finite element neutron kinetics coupled code system FENNECS/ATHLET for safety assessment of (very) Small and Micro Reactors, J. Phys.: Conf. Ser. (2020).

[16] E.E. Lewis, W.F. Miller, Computational methods of neutron transport, Wiley, New York, 1984.

[17] S. Dürigen, E. Fridman, The simplified P3 approach on a trigonal geometry of the nodal reactor code DYN3D, Kerntechnik 77 (2012) 226–229.

[18] S. Dürigen, Neutron Transport in Hexagonal Reactor Cores Modeled by Trigonal-Geometry Diffusion and Simplified P3 Nodal Methods (2013).

[19] S. lo Muzio, A. Seubert, Implementation And Validation Of The Steady State SP3 Approximation In The GRS FENNECS Code, in: Proceedings of NENE 2022; paper submitted.

[20] V. Boyarinov, P. Fomichenko, J. Hou, K. Ivanov, A. Aures, W. Zwermann et al., Deterministic Time-Dependent Neutron Transport Benchmark without Spatial Homogenization (C5G7-TD) Volume I: Kinetics Phase (C5G7-TD): Volume I: Kinetics Phase, 2018.

4.4 The ESFR

M&C 2023 - The International Conference on Mathematics and Computational Methods Applied to Nuclear Science and Engineering · Niagara Falls, Ontario, Canada · August 13 – 17, 2023

Validation of the FENNECS SP_3 Solver with Control Rod Insertion Simulations of the ESFR Using Serpent Cross Sections

S. lo Muzio, A. Seubert

Gesellschaft für Anlagen und Reaktorsicherheit (GRS) gGmbH
Boltzmannstraße 14, 85748 Garching near Munich, Germany

silvia.lo-muzio@grs.de, armin.seubert@grs.de

ABSTRACT

Due to the irregular and complex geometries of (very) small modular reactors ((v)SMR) and micro modular reactors (MMR), adequate neutronics codes are required for their safety assessment. Monte Carlo codes as well as deterministic transport codes are too expensive. To reduce the calculation time, a solution is to use diffusion codes, like the one implemented in the 3D neutron kinetics code FENNECS. However, diffusion theory may not be suited for heterogeneous and high-leakage concepts like (v)SMR and MMR. The third order Simplified Spherical harmonics approximation of the transport equation (SP_3) could be a reasonable compromise. Therefore, the FENNECS code was extended by an SP_3 solver. Within the validation process of the newly implemented solver, this was applied on the European Sodium Fast reactor (ESFR) at nominal condition as well as at 11 different control rods insertion depths. The macroscopic cross section libraries as well as reference solutions were obtained with Serpent. The simulations of the ESFR 12 states were performed with the preexisting FENNECS diffusion solver as well as with the new SP_3 solver. Additionally, the diffusion calculations were repeated also with SPH corrected cross sections. For the nominal condition and the weak controlled states, a good agreement between the results obtained from the FENNECS SP_3 solver and the ones of the reference could be observed, showing the successful implementation of the solver in FENNECS. For the highly controlled states, a good agreement with the reference could be only obtained using the SPH method and the diffusion solver.

KEYWORDS: FENNECS, SP_3, Sodium-cooled Fast Reactor, SPH

1. INTRODUCTION

Due to the small size and inhomogeneous configuration of (very) small modular reactors ((v)SMR), and micro modular reactors (MMR), special tools for their safety assessment are required, especially regarding the simulation of the 3D neutron kinetics [1]. To model such geometries, Monte Carlo codes would be suited. However, due to the long calculation times, these cannot be applied for routine calculations. An alternative are deterministic codes, since they are cheaper, offering the possibility to simulate also transients [2]. However, deterministic codes relaying on the neutron transport equation are still too expensive [3,4]. Here, a solution is to apply approximations. The most popular one is diffusion theory, which is obtained from the neutron transport equation by assuming isotropic scattering, few absorption events, compared to scattering, and slow varying neutron flux in space [4–7]. It is obvious that these assumptions are not satisfied in heterogeneous and small geometries with strong neutron absorbers, like the ones of (v)SMR and MMR. Therefore, the diffusion approximation may not perform well for (v)SMR and MMR. Solvers based on the third order Simplified Spherical Harmonics Approximation of the transport equation (SP_3) are

expected to be a compromise between the efficient, but less accurate diffusion solvers, and the CPU-demanding, but more accurate transport codes. Therefore, to overcome the limitations of the diffusion equations in specific situations, for the safety assessment of (v)SMR and MMR, the Finite ElemeNt NeutroniCS Code (FENNECS), a deterministic code developed at Gesellschaft für Anlagen- und Reaktorsicherheit (GRS) gGmbH, was recently extended by a steady state SP_3 solver. Since the main goal of the FENNECS SP_3 solver is to model (v)SMR and MMR, this was already tested on small and heterogeneous geometries. For these systems, the results the FENNECS SP_3 solver showed a very good agreement with the reference [8,9].

In this work, the functionality and performance of the SP_3 solver will be shown on the ESFR, a large sodium-cooled fast reactor specified within the project "European Sodium Fast Reactor Safety Measures Assessment and Research Tools" (ESFR-SMART) [10]. The current work is firstly a contribution to the validation of the new FENNECS SP_3 solver. Secondly, it aims to prove the ability of the solver in modelling also large cores. Thirdly, since controlled states are challenging for diffusion solvers, the ability of the SP_3 in modelling them will be tested. In these scenarios, the position of the Control Shutdown Device (CSD) and the Diverse Shutdown Device (DSD) rods is changed. Fourthly, to improve the results of the diffusion solver, the Superhomogeneisation (SPH) method [11] will be applied on the cross section libraries.

2. FENNECS

The Finite ElemeNt NEutroniCS code FENNECS is a 3-d few-group neutron kinetics code based on the Finite element method, where upright triangular prisms are used as finite elements [12–14]. It provides a diffusion as well as an SP_3 solver , which can perform steady state calculations, but only the diffusion solver can calculate transient scenarios [12,13]. The code is based on the Galerkin weighted residual approach [14]. The meshing of the geometry is performed by the Python Enhanced Meshing Tool with Yaml input (PEMTY), which is also able to generate cross section libraries in NEMTAB format from Serpent output files [12]. Furthermore, as explained in [15], it can apply the SPH correction to the cross libraries.

Table I: Energy groups structure used for the macroscopic cross sections.

Group index	1	2	3	4	5
Lower energy boundary	6.065307 MeV	2.231302 MeV	820.85 keV	301.9738 keV	111.09 keV

Group index	6	7	8	9	10
Lower energy boundary	40.86771 keV	15.03439 keV	5.530844 keV	2.034684 keV	0 eV

Table II: Locations of the DSD and CSD rods, which correspond to the bottom of the control rod, with respect to the top of active core plane [16].

Step	0 (ARO)	1	2	3	4	5
DSD location [cm]	5.027	0.000	-9.552	-19.103	-28.655	-38.206
CSD location [cm]	5.027	0.000	-8.546	-17.092	-25.638	-34.184

Step	6	7	8	9	10	11 (ARI)
DSD location [cm]	-47.758	-57.310	-66.861	-76.413	-85.964	-95.516
CSD location [cm]	-42.731	-51.277	-59.823	-68.369	-76.915	-85.461

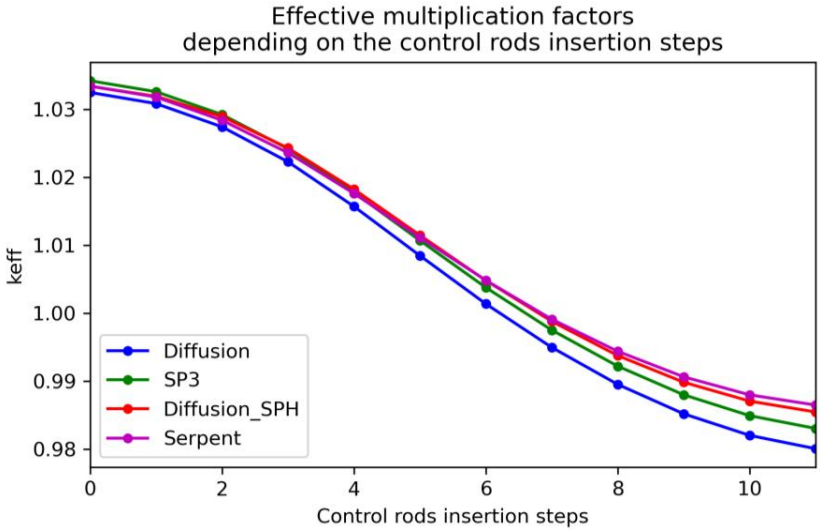

Figure 1. Effective multiplication factor versus the CR insertion steps for the FENECS diffusion (blue), SP_3 (green) and SPH corrected diffusion (red) solver as well as for Serpent (pink). The step 0 and 11 represents the ARO and ARI configuration, respectively.

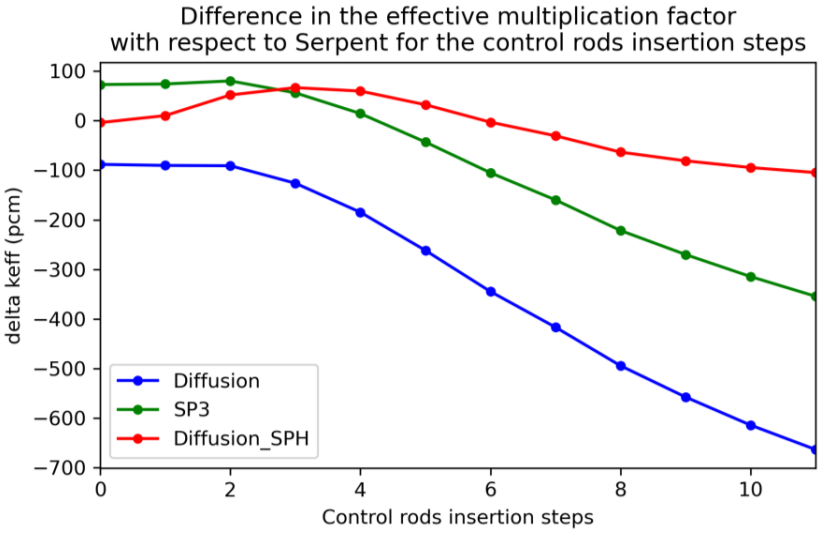

Figure 2. Error of the effective multiplication factor for FENECS diffusion (blue), SP_3 (green) and SPH corrected diffusion (red) solver, with respect to Serpent, versus the CR insertion steps. The step 0 and 11 represents the ARO and ARI configuration, respectively.

3. METHODOLOGY

The macroscopic cross sections were generated with the Monte Carlo code Serpent, based on the groups structure given in Table I. The cross sections were obtained by modelling the assemblies as three-dimensional, where the CSD and DSD rods are surrounded by 6 half of fuel assemblies. To obtain the SPH corrected cross sections, the same approach was used to model their absorber materials, hence natural and enriched boron. The corrected cross section libraries were obtained applying the iterative scheme of the SPH method, implemented in PEMTY.

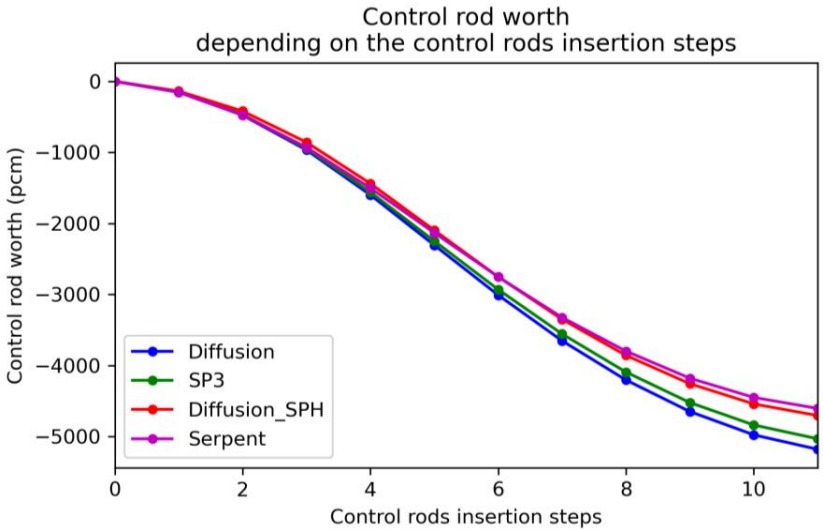

Figure 3. CR worth for FENECS diffusion (blue), SP_3 (green) and SPH corrected diffusion (red) solver, with respect to Serpent, versus the CR insertion steps. The step 0 and 11 represents the ARO and ARI configuration, respectively.

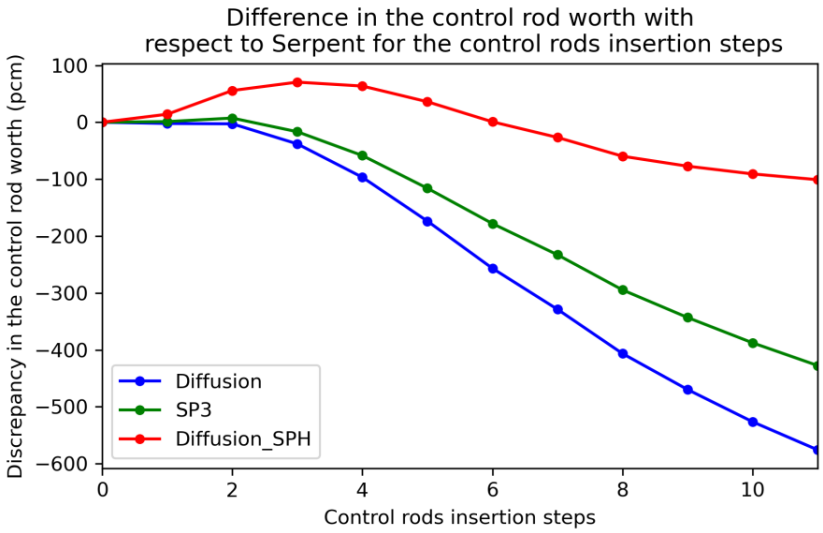

Figure 4. Error in the CR worth for FENECS diffusion (blue), SP_3 (green) and SPH corrected diffusion (red) solver, with respect to Serpent, versus the CR insertion steps. The step 0 and 11 represents the ARO and ARI configuration, respectively.

Serpent was also used to calculate the reference effective multiplication factors (k_{eff}) and normalized power distributions of the ESFR full core for the nominal condition, hence all rods out (ARO) configuration, and the further 11 scenarios with different control rods insertion depths, given in Table II, where the last configuration is all rods in (ARI). It should be remarked that in all calculations the uncertainty of the k_{eff} calculated by Serpent is never above 4.90pcm. In the next sections, the performance of the SP_3 solver will be analysed based on the discrepancy in the k_{eff} and in the control rod (CR) worth, as well as on the root mean squared (RMS) and maximum error of the normalized power distibutions, all with respect to Serpent.

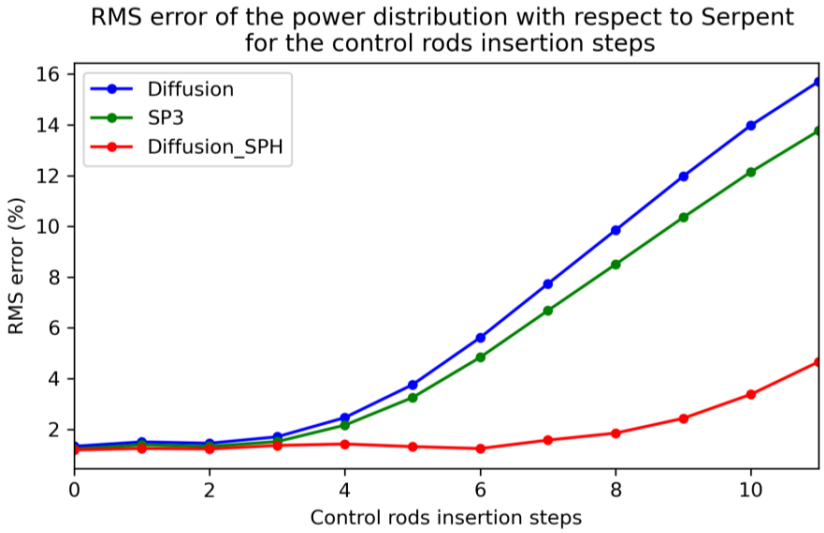

Figure 5. RMS error (%) for FENECS diffusion (blue), SP_3 (green) and SPH corrected diffusion (red) solver, with respect to Serpent, versus the CR insertion steps. The step 0 and 11 represents the ARO and ARI configuration, respectively.

Table III: Maximum error (%) of the power distribution with respect to Serpent.

Step	0	1	2	3	4	5	6	7	8	9	10	11
Diffusion	3.2	3.4	2.8	4.0	5.7	8.9	13.4	18.5	23.7	28.6	33.1	35.9
SP_3	2.5	2.9	2.5	3.6	4.9	7.5	11.4	15.8	20.4	24.7	28.8	31.4
Diffusion SPH	4.1	4.5	3.8	4.2	4.3	3.8	4.3	4.1	4.7	6.4	8.9	11.1

4. RESULTS

4.1.The effective multiplication factor

The discrepancy between the k_{eff} of the FENNECS SP_3 solver and the one of Serpent tends towards negative values as the CR are inserted, as shown in Fig. 1 and 2: from step 0 to 4, the error is positive and tends to 0 and from step 5 it becomes negative. Therefore, at the beginning, the k_{eff} is overestimated. For the diffusion solver, the error in the k_{eff} is always larger, compared to the one of the SP_3 calculation. However, for the first steps, their magnitudes are similar. Additionally, since the k_{eff} of the diffusion solver is always smaller, compared to the reference, it is not conservative. Furthermore, for the steps 3 and 4, even if the SPH correction is applied, the effective multiplication factor obtained from the SP_3 solver shows a smaller error.

4.2. The control rod worth

As shown in Fig. 3 and 4, for the calculations without SPH correction, the error in the CR worth, with respect to Serpent, goes towards large negative values as they are inserted deeper in the core. The CR worth of the SP_3 solver is always closer to the reference, compared to the one of the diffusion solver, except in step 2. It should be remarked, that in the first two steps, the magnitude of the errors in the CR worth of the two solvers are very similar. Hence, using the SP_3 approximation, does not lead to significant improvements

for (almost) uncontrolled cores. This is not the case as the CR are inserted deeper in the core. Furthermore, the diffusion theory always overestimates the CR worth. This was observed also in the previous subsection. For the SP_3 solver, this overestimation starts from step 3 and it is weaker.

From the comparison between the CR worth obtained from the SP_3 and the diffusion solver with SPH correction, it can be observed that better results are obtained starting from the ARO configuration until step 4. Starting from step 5, the diffusion solver with SPH correction gives a CR worth closer to the reference.

4.3. The normalized power distribution

Regarding the RMS error and magnitude of the maximum error of the normalized power distribution calculated by the SP_3 method, with respect to Serpent, it can be observed that they increase as the CR are inserted deeper in the core, as it can be observed in Fig. 5 and Table III. The RMS error obtained with the SP_3 solver is always smaller compared to the one of the respective diffusion solution. However, a considerable improvement can be observed if the SPH correction is applied before using the diffusion solver. In this case, a smaller RMS error is obtained, compared to the SP_3 method.

Also regarding the maximum error of the normalized power distribution, the SP_3 solver results are closer to the reference, compared to the diffusion solver. Additionally, the maximum error obtained from the SP_3 is closer to zero from step 0 to 3, if compared to the SPH calculations. This means that in these steps, the SP_3 solver calculates power distributions, where the RMS error is larger compared to the SPH diffusion solution, but smaller error peaks are obtained. Hence, for the SP_3 solver, the spatial distribution of the errors is flatter. This hypothesis will be confirmed in the next subsection. Starting from step 4, the maximum error of the SP_3 simulations is larger, than the one of the SPH diffusion calculations.

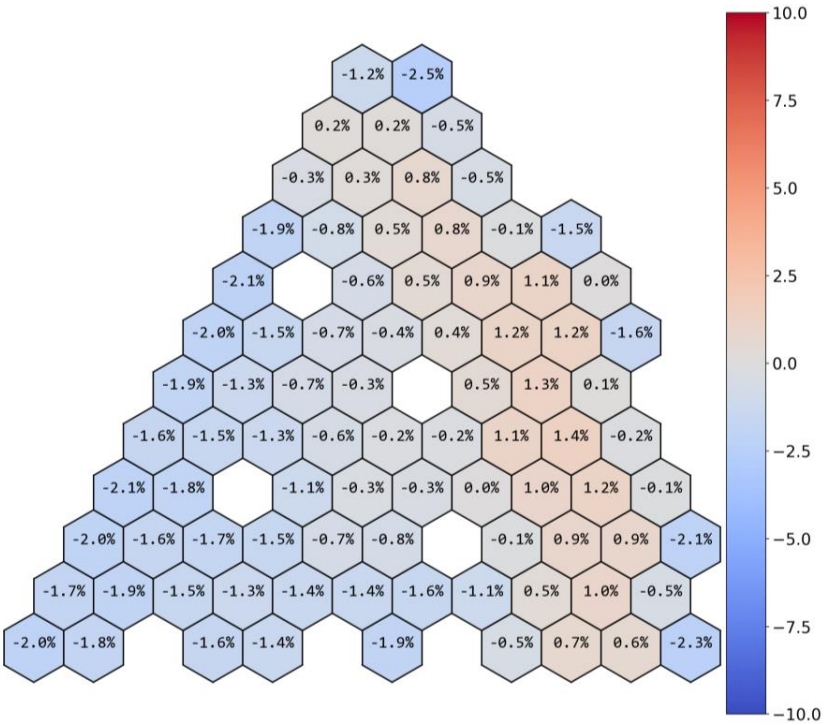

Figure 6. Errors in the power distribution obtained with the FENNECS SP_3 solver with respect to the reference (Serpent), for the step 0, hence ARO.

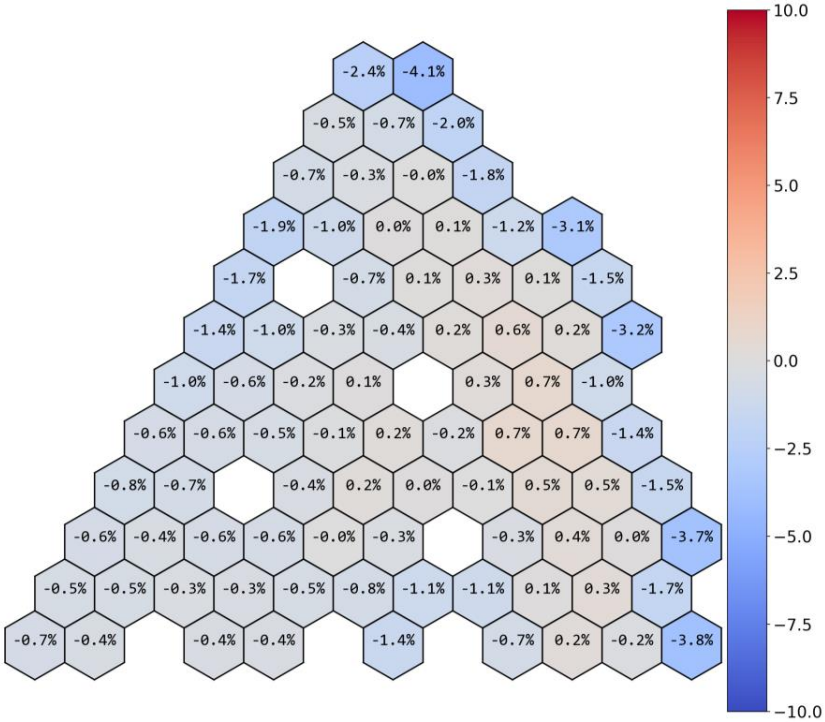

Figure 7. Errors in the power distribution obtained with the SPH corrected FENNECS diffusion solver, with respect to the reference (Serpent), for the step 0, hence ARO.

4.4. The nominal condition, step 1, 6, and 11

For the nominal condition, in all three calculations, a very good agreement with the Serpent reference, which is $k_{eff} = 1.03341 \pm 4.90 \cdot 10^{-5}$, is achieved. In particular, the magnitudes of the error obtained from the SP_3 and the diffusion solver are similar, even though the k_{eff} of the SP_3 solver shows a better agreement with the reference. For the first solver, the discrepancy is only 73pcm and for the diffusion solver -88pcm. A k_{eff} closer to the reference can be obtained using the diffusion solver with SPH correction: in this case the deviation is only -4pcm, which is less than the uncertainty of the Serpent calculation. Similar findings apply also to the RMS error of the normalized power distribution with respect to Serpent. However, with the SP_3 solver, the maximum error is closer to zero, compared to both diffusion calculations. This means, that the spatial error distribution is flatter for the SP_3 solver, as shown in Fig. 6, compared to the one of the SPH corrected diffusion calculations, shown in Fig. 7, which shows error peaks at the radial boundary.

Starting from step 1, the DSD and CSD are inserted in the core. From the point of view of the k_{eff}, the SPH corrected calculation is closer to the reference. This is not the case if the CR worth is considered: here, for the not-SPH corrected calculations, the errors are within the Serpent calculation uncertainty, which is 4.90pcm. In particular, the CR rod worth deviation for the SP_3 solver is only 1pcm. For the power distributions, the same considerations made for the ARO configuration can be applied here.

In step 6, the errors obtained from the non-SPH corrected calculations start to be more pronounced also for the FENNECS SP_3 solver. Although, the error for the effective multiplication factor is only -105pcm. In case of the diffusion solver, this value is more than three times larger. For the SP_3 solver, the deviation of the CR worth is -178pcm, whereas for the diffusion solver -257pcm. Consequently, for both solvers, an overestimation of the CR absorption can be observed. A strong improvement of the results can be obtained

using the SPH correction and the diffusion solver. In this case, the error in the k_{eff} is only -3pcm and the one in the CR worth only -1pcm, hence less than the Serpent calculation uncertainty, which is 1.6pcm. The overestimation of the CR absorption is mirrored also in the normalized power distribution: for the SP_3 solver, the RMS error is smaller compared to the diffusion solver, where it is above 5%, and in both cases, the maximum error is larger than -10%. On the contrary, for the SPH corrected diffusion calculation, the RMS error is below the one of the SP_3 calculation and the maximum one is -4.13%.

The most interesting step is the last one, hence ARI. For the k_{eff} as well as the CR worth, the diffusion and the SP_3 solver show errors, which are larger than -350pcm. However, with the SP_3 solver, a better agreement with the reference is achieved. Further improvements are obtained for the SPH corrected diffusion calculations: here, the deviations are in the order of -100pcm. These high deviations of the diffusion and SP_3 solver are also mirrored in the error of the normalized power distributions: for both, the RMS and the maximum error are larger than 13% and -30%, respectively. Whereas, for the SPH corrected calculation using the diffusion solver, the RMS error is still below 5%. However, the maximum error is above 10%. Now, it is important to investigate where such high deviations take place. As it can be seen in Fig. 8, the highest deviations are in the central region. As shown in Fig. 9, in these assemblies, the normalized power is not above 0.3, hence very low. The fact, that the high errors occur in low power region, makes them less safety relevant. In the hottest assembly, the error obtained from the SP_3 solver is only 5.8%.

5. CONCLUSIONS

In this work, the ESFR in nominal condition as well as in further 11 scenarios with different CR insertion depths was modelled with the FENNECS diffusion and SP_3 solver, using Serpent generated cross sections. Additionally, diffusion calculations using SPH-corrected cross sections were performed. Reference solutions for the 12 scenarios were obtained with Serpent.

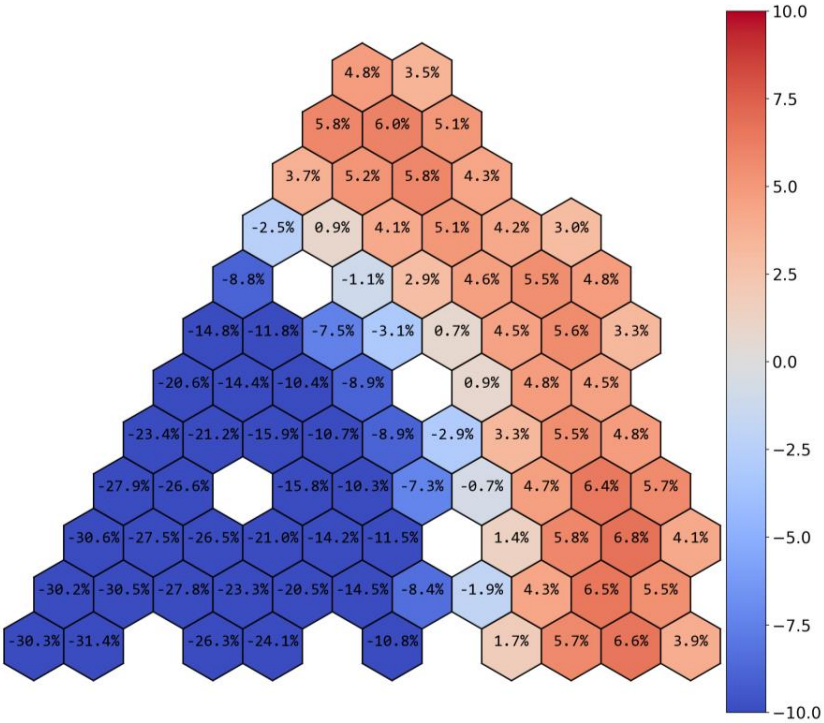

Figure 8. Errors in the power distribution obtained with the FENNECS SP_3 solver with respect to the reference (Serpent), for the step 11, hence ARI.

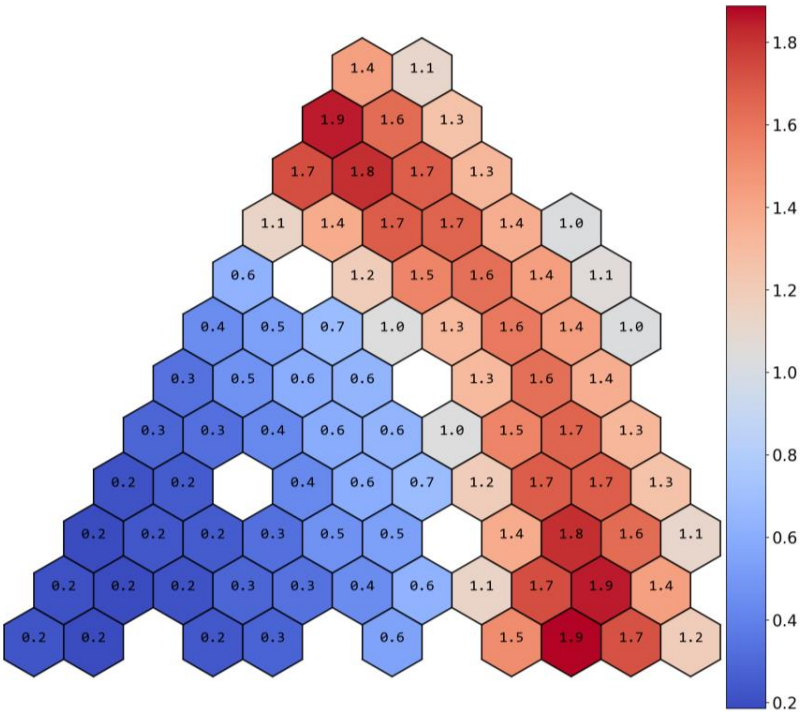

Figure 9. Normalized power distribution obtained by the FENNECS SP_3 solver for step 11.

With the diffusion solver, larger deviations from the reference are obtained, compared to the SP_3 solver. This holds for the k_{eff}, the CR worth and the RMS and maximum error of the normalized power distribution. Since the SP_3 approximation accounts, to a certain extent, for angular scattering and neutron flux anisotropy, its better performance, compared to the diffusion theory, also in modelling large cores, is not surprising.

In particular, for the ARO configuration, as well as the first two rodded states, both solvers calculated similar magnitudes of the errors, with respect to the reference. In these steps, the diffusion solver underestimates the k_{eff}, leading to issues from the safety point of view. On the contrary, the SP_3 overestimates it, not causing concerns from a safety point of view. In these states, only very small improvement could be achieved thanks to the use of the SP_3 solver, particularly for the k_{eff} and CR worth. An improvement can be achieved only in the k_{eff} and RMS error of the normalized power distribution using SPH corrected cross sections together with the diffusion solver. However, for the normalized power, the spatial error distributions are flatter for the SP_3, compared to the SPH corrected diffusion calculations.

For the strong controlled configurations, very high errors are obtained by the diffusion solver for the k_{eff}, the CR worth as well as the normalized power distribution. Surprisingly, in these configurations, with the SP_3 solver, errors in the same order of magnitude of the ones of the diffusion solver are obtained, even though the magnitude of the errors is considerably smaller, but they are still high. In particular, both solvers strongly overestimate the CR absorption power, leading to issues from the point of view of the safety. In these scenarios, very good results were obtained with the diffusion solver using SPH corrected cross sections, except for the maximum error which is still high.

For this reason, as next step, the SPH correction of the cross section libraries will be suitably extended to be applicable to the SP_3 solver, in order to improve the results of strongly controlled states and in particular to reduce the maximum errors in the normalized power distribution. Furthermore, the SP_3 solver will be tested on small and strongly controlled cores.

ACKNOWLEDGMENTS

This work was supported by the German Federal Ministry for the Environment, Nature Conservation, Nuclear Safety and Consumer Protection. Furthermore, we thank our colleague Dr. Bousquet for the implementation of the SPH correction in PEMTY and the related support in the generation of the macroscopic cross section libraries.

REFERENCES

1. A. SCHAFFRATH et al. “SMRs — overview, international developments, safety features and the GRS simulation chain,” *Front. Energy*, **15,** *4*, 793 (2021).
2. LEVON GHASABYAN. “Use of Serpent Monte-Carlo code for development of 3D full-core models of Gen-IV fast-spectrum reactors and preparation of group constants for transient analyses with TRACE-PARCS coupled system,” (2013).
3. C. LIANGZHI and H. WU, *Deterministic Numerical Methods for Unstructured-Mesh Neutron Transport Calculation*, Elsevier Science & Technology, San Diego (2021).
4. A. V. AVVAKUMOV et al. “Numerical modeling of neutron transport in SP3 approximation by finite element method,” http://arxiv.org/pdf/1903.11502v1.
5. W. M. STACEY, *Nuclear reactor physics*, 2. ed., completely rev. and enlarged., WILEY-VCH, Weinheim (2007).
6. S. MARGUET, *The Physics of Nuclear Reactors*, Springer International Publishing (2018).
7. K. DEVAN and A. BACHCHAN, *Homogeneous reactor and neutron diffusion equation*, in: P. Mohanakrishnan et al. (Eds.), *Physics of nuclear reactors*, 193, Academic Press an imprint of Elsevier, London (2021).
8. S. LO MUZIO and A. SEUBERT, *Implementation And Validation Of The Steady State SP3 Approximation In The GRS FENNECS Code*, in: *Proceedings of NENE 2022; paper submitted*.
9. S. LO MUZIO and A. SEUBERT. “Verification of the SP3 Solver in FENNECS with C5G7 Test Cases using HELIOS Cross Sections,” *ETSON Conference in Munich* (2022).
10. A. RINEISKI et al. “Specification of the new core safety measures,” European Commission (Jul. 2018).
11. ALAIN HÉBERT. “A consistent technique for the pin-by-pin homogenization of a pressurized water reactor assembly,” *Nucl. Sci. Eng., 113 (3)*, 227 (1993).
12. J. BOUSQUET et al. “New finite element neutron kinetics coupled code system FENNECS/ATHLET for safety assessment of (very) Small and Micro Reactors,” *J. Phys.: Conf. Ser*. (2020).
13. A. SEUBERT et al. “RECENT ADVANCES OF THE FENNECS NEUTRONICS CODE FOR SAFETY ASSESSMENT OF (V)SMR, GENERATION IV AND OTHER INNOVATIVE CONCEPTS,” *The International Conference on Mathematics and Computational Methods Applied to Nuclear Science and Engineering: Proceedings*, Raleigh, North Carolina, 11-15 April (2021).
14. S. LO MUZIO et al., *SIMULATION OF CEFR NEUTRONIC START-UP TESTS WITH FENNECS AND COUPLED PIN-BY-PIN MODEL OF A CEFR SUBASSEMBLY*, in: KERND (Ed.), *Proceedings of Young Scientist Workshop at Kerntechnik 2022* (2022).
15. R. HENRY et al. “Analysis of the X2 VVER-1000 benchmark with FENNECS,” *Proceedings of NENE 2021 conference* (2021).
16. M. MARGULIS et al. “Safety and performance parameters at EOC,” European Commission (Jun. 2020).

Chapter 5

Conclusions and outlook

5.1 Conclusions

The goal of this work is the implementation of a new steady state solver based on the SP_3 approximation of the neutron transport equation in the GRS neutronics diffusion code FENNECS. The new solver is necessary in FENNECS in order to perform the safety assessment of (v)SMRs and MMRs. Such reactors are characterised by complex and heterogeneous geometries, which are difficult to model with other codes. These inhomogeneous and compact cores can be modelled with transport theory. Deterministic as well as Monte Carlo codes based on transport theory are available. Both require higher computational costs compared to a deterministic diffusion or SP_3 solvers. Monte Carlo deterministic codes offer a very high geometrical flexibility, which allows to model the complex geometries of (v)SMRs and MMRs. This feature is typically not provided by deterministic transport codes. However, Monte Carlo transport codes require very high computational times. This makes them unpractical for transient calculations. Furthermore, no coupling between Monte Carlo transport codes and ATHLET [1] or CTF [52] exists. To reduce the computational costs, approximations are applied to the neutron transport equation. The most common one is diffusion theory. Unfortunately, this cannot model reliably (v)SMRs and MMRs, due to their small and heterogeneous geometries. The SP_3 approximation of the neutron transport equation offers a higher accuracy compared to diffusion theory. Therefore, to increase the accuracy of FENNECS, originally a diffusion code, the new SP_3 solver was implemented in this code. The new SP_3 solver was implemented in FENNECS because this code offers already a coupling with ATHLET as well as CTF. Therefore, neutronic calculations with thermal-hydraulic feedback can be performed. Furthermore, FENNECS offers a high geometrical flexibility (see section 2.2), required

to model the geometries of (v)SMRs and MMRs.

The steady state SP_3 equations, including the boundary conditions, were derived starting from setting up the neutron transport equation (see chapter 3). After the derivation of the SP_3 equations, their Galerkin form was obtained. This was necessary to implement the equations in the finite elements based code FENNECS. Ad hoc algorithms to solve the SP_3 equations in the Galerkin form were developed, in order to implement the steady state SP_3 solver in FENNECS.

The SP_3 solver was verified based on the following models:

- homogeneous slab [47]
- heterogeneous slab [47]
- highly enriched fuel assembly
- 2D Cartesian planar benchmark [29]
- Hébert benchmark [29]
- three homogenous cores of different size [5]
- UO_2 fuel assembly of the C5G7 benchmark [10]
- MOX fuel assembly of the C5G7 benchmark [10]
- ESFR [51].

In the verification process (see chapter 4), the comparison was performed using as reference the transport codes ONEDANT [17], Serpent [35], ERANOS [50] or HELIOS [62] or the SP_5 or SP_3 solver of TRIVAC [28]. The study was also supported by comparisons with other SP_3 codes. Furthermore, diffusion theory was used, whose results were also compared to the ones of the reference. This step makes possible to assess the improvement in accuracy by using the more computationally expensive method of the SP_3 approach.

Firstly, the homogeneous and the heterogeneous slab [47] were analysed. These are very simple geometries with strong heterogeneities, due to the very small size and the vacuum boundary condition. In addition, in the heterogeneous slab, different materials regions of small size are present. The homogeneous and the heterogeneous slab were modelled with only one energy group. These calculations were actually performed at the beginning of the verification phase to firstly verify the functionality of the FENNECS SP_3 solver. The reference results were obtained with ONEDANT, a

transport code. For both slabs, a high deviation between the effective multiplication factor obtained from ONEDANT and the one calculated by the FENNECS SP_3 solver was observed. This deviation ranged between -2308 pcm and -1011 pcm. Nevertheless, this deviation was considerably smaller compared to the one obtained from the FENNECS diffusion solver, which was between $-19\,375$ pcm and -3736 pcm. Hence, with the SP_3 solver, an improvement was achieved. The FENNECS results were compared also with the diffusion and SP_3 solvers developed in the frame of [47]. No deviations between the results of these solvers and the ones of FENNECS could be observed. Therefore, if the FENNECS results were compared with the same solver, an excellent agreement was obtained. The ability of FENNECS in reproducing the same results as the code presented in [47] shows the successful implementation of the solver. Furthermore, it reveals the difficulty of the SP_3 solvers in modelling such geometries.

Another simple test case that was analysed is a highly enriched fuel assembly with vacuum boundary conditions. Two energy groups were used. The reference effective multiplication factor as well as the macroscopic cross sections were obtained with Serpent. For the FENNECS SP_3 solver, the discrepancies with the reference were between 371 pcm and 5724 pcm, depending on the mesh. Therefore, it can be observed that refining the mesh improves the results by one order of magnitude. This holds particularly for the radial mesh size. On the contrary, for the FENNECS diffusion solver, the refinement only weakly improves the results. For this solver the discrepancies were much higher and ranged between 20 022 pcm and 27 393 pcm. Hence, a considerable improvement could be obtained with the SP_3 methodology.

Further simple models analysed are three cores of different size. These have a larger size, compared to the previous test cases. Two energy groups macroscopic cross section libraries obtained with ERANOS and with Serpent were used. The goal was to conduct a performance comparison between cross section calculation methodologies in relation with the SP_3 solver. For the SP_3 solver, the diffusion coefficient was calculated with two approaches. In the first one, the coefficient was defined based on the macroscopic transport cross section and in the second one based on the total and first order scattering cross section (see chapter 3). For both approaches, the SP_3 solvers of FENNECS and SPNDYN [5] calculated similar results. The reference multiplication factors were calculated by Serpent as well as ERANOS. For FENNECS, the SP_3 methodology improved the accuracy of the results with respect to diffusion theory. The improvement in the effective multiplication factor ranged between 9 pcm and 665 pcm, depending on the core size analysed, on the applied mesh, the definition of the diffusion coefficient and the cross sections used. The highest improvements were observed for the smallest core. For the comparison with the reference, a key role was played by the source program used for the cross section generation and by the approach

used to calculate the zeroth order diffusion coefficient. If the cross sections generation was carried out with ERANOS, which calculated the macroscopic cross sections using the higher order fluxes, similar results were obtained for the two approaches used to calculate the diffusion constant within the SP_3 methodology. The differences between them increased if Serpent generated cross sections were used, which are obtained using only the zeroth order flux.

More complex models are the Cartesian and the Hébert benchmarks. These two were modelled with only a single energy group. For the Cartesian and Hébert benchmarks, the TRIVAC SP_5 and SP_3 solvers were used as reference, respectively. Additionally, in the evaluations of the results of the Cartesian and Hébert benchmarks, the SP_3 solvers of TRIVAC and DYN3D were involved, respectively. For these geometries, using the FENNECS SP_3 solver, always improved the results by orders of magnitude, compared to diffusion theory. As for all test cases analysed in this work, a strong dependency on the mesh was observed. This is not surprising, since the finite element method is characterised by a strong dependency on the mesh. For the Cartesian and the Hébert benchmarks, deviations in the effective multiplication factor of above 500 pcm were observed for the coarsest meshes and very good results could be achieved for finer meshes: for meshes, were each assembly was divided in at least 10 parts in radial direction, deviations below 120 pcm were obtained. Hence, the FENNECS SP_3 solver, showed a the strong dependency of the results on the mesh also for these two benchmarks.

In this work, also models with a larger number of energy groups were analysed. The simplest ones are the single fuel assemblies of the C5G7. For the simulation, 7 energy groups were used. The reference results as well as the macroscopic cross section libraries for the UO_2 and the MOX fuel assembly with reflecting boundary conditions were obtained with HELIOS. The new FENNECS SP_3 solver showed for both test cases a good agreement with the reference: the deviations in the k_{eff} and in the normalized power distribution were never above 66 pcm and 0.17%, respectively. The FENNECS SP_3 solver was able to improve the results from the point of view of the effective multiplication factor as well as normalized power distribution. For k_{eff}, in case of the UO_2 fuel assembly, the improvement ranged between 13 pcm and 15 pcm, depending on the mesh. A higher improvement was observed for the MOX fuel assembly, which shows a more heterogeneous configuration compared to the UO_2 fuel assembly: for the effective multiplication factor, the increase in accuracy was between 34 pcm and 42 pcm, depending on the mesh applied. Therefore, a dependency between the improvement in accuracy and the heterogeneity of the geometry can be observed.

To a certain extend, a similar tendency can be observed also for the modelled ESFR

configurations. For the simulations, 10 energy groups were used. These were obtained with Serpent. The same code waas used also for the calculation of the reference results. Also for the ESFR, except the strongly controlled states, using the FENNECS SP_3 solver, a good agreement with the reference could be achieved: in the first CR insertion step, the CR worth calculated by the FENNECS SP_3 showed a deviation from the reference of only -1 pcm. This can be judged as a very small deviation, considering that the calculation uncertainty was only $4.90 \cdot 10^{-5}$. Furthermore, an improvement in the accuracy was obtained, with respect to the diffusion calculations. This is also the case for the strongly controlled states of the ESFR: for the all rods in (ARI) condition of the ESFR, the improvement in the k_{eff} was above 300 pcm. In this scenario, the error obtained in the k_{eff} by the diffusion solver was almost halved using the SP_3 solver. Regarding this two arguments, three scenarios can be distinguished, as explained hereafter. Firstly, for the low controlled states of the ESFR, the two solvers do not show enormous differences in the results: the system is homogeneous enough, such that the diffusion approximation is able to calculate good results. Secondly, this is not the case if the CRs are further inserted in the core. For the medium controlled states of the ESFR, a considerable improvement could be obtained with the FENNECS SP_3 solver. Actually, for the fifth CR insertion step, the deviation in the k_{eff} calculated by the SP_3 solver was only -43 pcm, which was less than one sixth of the one obtained from the diffusion approximation. Thirdly, by further increasing the heterogeneities, hence by considering the highly controlled states of the ESFR, despite the improvement due to the SP_3 methodology, the deviations with respect to the reference were too high. For the ARI configuration calculated by the FENNECS SP_3 solver, the maximum error in the normalized power distribution was 35.85%. Even though this high deviation was not in the hottest assembly. For these highly controlled scenarios, good results could only be obtained by applying the SPH method to the macroscopic cross sections, before using the diffusion solver. In this case, for ARI, the RMS error of the normalized power distribution was below 5%.

Based on the results summarised here, besides the implementation of the steady state SP_3 methodology in the FENNECS code, this work was able to verify the new solver, proving its functionality and its higher accuracy compared to diffusion theory. Furthermore, the strong points as well as the limitations of the new solver were identified.

5.2 Outlook

The implementation of the steady state SP_3 solver in FENNECS and the verification work presented open multiple possibilities regarding further developments. The first option is to perform further research on the implemented SP_3 solver. The second one concerns the development of the FENNECS transient SP_3 solver and the third one coupled calculations with the new solver and ATHLET.

5.2.1 Further works on the steady state FENNECS SP_3 solver

The test case with the three cores of different size, where two different approaches were used for the macroscopic cross sections generations, offers multiple ideas regarding further research. Firstly, further studies should be performed in order to understand the correlation between the cross sections generation program and the results obtained, also in relationship with the type of system modelled. Secondly, additional studies on the two possible SP_3 approaches are necessary, also in relationship with the cross sections generation methodology and the type of system modelled.

Further verification should be performed on real (v)SMRs and MMRs configurations. A possibility would be to test the new solver on a real design, like the NuScale US600 [2].

Thirdly, the solver could be optimized from the point of view of the calculation time. For example, the Wielandt convergence acceleration method should be implemented for the FENNECS SP_3 solver, as it is already done for the diffusion solver.

5.2.2 Development of the transient SP_3 solver

At the moment, in FENNECS, only the diffusion solver is capable to perform transient calculations. The work presented in this thesis represents the first stone for performing calculations with complex geometries with a better resolution than diffusion theory. This thesis represents the starting point for implementing a transient SP_3 solver in FENNECS.

5.2.3 Coupled calculations

FENNECS profits from the coupling with the GRS thermal-hydraulic code ATHLET. Now, it is possible to perform steady state coupled simulations with higher accuracy, taking advantage of the new FENNECS steady state SP_3 solver. When this will be

also capable to perform transient calculations, it will be possible to calculate transients with the FENNECS SP_3 solver and the thermal-hydraulic feedback from ATHLET.

List of Figures

Bibliography

[1] ATHLET 3.3 Program Overview.

[2] NuScale Standard Plant Design Certification Application: Part 02 - Final Safety Analysis Report (Rev. 5), Tier 2, Chapter 4, Reactor.

[3] H. A. Gabbar, M. R. Abdussami, and M. I. Adham. Techno-Economic Evaluation of Interconnected Nuclear-Renewable Micro Hybrid Energy Systems with Combined Heat and Power. *Energies*, 13(7):1642, 2020.

[4] A. V. Avvakumov, V. F. Strizhov, P. N. Vabishchevich, and A. O. Vasilev. Numerical modeling of neutron transport in SP3 approximation by finite element method. *CoRR*, (arXiv:1903.11502v1 [cs.CE]), 2019.

[5] B. Babcsány, Z.I. Böröczki, J.E. Maróti, and M. Szieberth. On the Effect of Scalar Flux Weighting of Linearly Anisotropic Scattering Matrices in Few-Group Transport Calculations. In *PHYSOR Proceedings*, 2022.

[6] G. Bal and L. Ryzhik. Diffusion Approximation of Radiative Transfer Problems with Interfaces. *SIAM Journal on Applied Mathematics*, 60(6):1887–1912, 2000.

[7] C. Beckert and U. Grundmann. A NODAL EXPANSION METHOD FOR SOLVING THE MULTIGROUP SP3 EQUATIONS IN THE REACTOR CODE DYN3D. *Joint International Topical Meeting on Mathematics & Computation and Supercomputing in Nuclear Applications (M&C + SNA 2007)*, 2007.

[8] J. Bousquet, R. Henry, and A. Seubert. NEW FINITE ELEMENT NEUTRON KINETICS CODE SYSTEM FENNECS/ATHLET FOR COUPLED SAFETY ASSESSMENT OF (VERY) SMALL AND MICRO REACTORS.

[9] J. Bousquet, A. Seubert, and R. Henry. New finite element neutron kinetics coupled code system FENNECS/ATHLET for safety assessment of (very) Small and Micro Reactors. *Journal of Physics: Conference Series*, 2020.

[10] V. Boyarinov, P. Fomichenko, J. Hou, K. Ivanov, A. Aures, W. Zwermann, and K. Velkov. Deterministic Time-Dependent Neutron Transport Benchmark without Spatial Homogenization (C5G7-TD) Volume I: Kinetics Phase (C5G7-TD): Volume I: Kinetics Phase.

[11] M. Burrone. *Study of eigenvalue formulations in the PN approximation of the neutron transport equation.* Master's Thesis, Politecnico di Torino, Torino, 2018.

[12] C. Canuto and A. Tabacco. Differential Calculus. In *Mathematical Analysis I*, pages 169–224. Springer, Cham, 2015.

[13] L. Cao and H. Wu. *Deterministic Numerical Methods for Unstructured-Mesh Neutron Transport Calculation.* Woodhead Publishing Series in Energy. Elsevier Science & Technology, San Diego, 2021.

[14] A. Carreño, A. Vidal-Ferràndiz, D. Ginestar, and G. Verdu. Adaptive time-step control for modal methods to integrate the neutron diffusion equation. *Nuclear Engineering and Technology*, 53(2):399–413, 2021.

[15] A. M. G. Cox, S. C. Harris, E. L. Horton, and A. E. Kyprianou. Multi-species Neutron Transport Equation. *Journal of Statistical Physics*, 176(2):425–455, 2019.

[16] K. Devan and A. Bachchan. Homogeneous reactor and neutron diffusion equation. In P. Mohanakrishnan, O. P. Singh, and K. Umasankari, editors, *Physics of nuclear reactors*, pages 193–262. Academic Press an imprint of Elsevier, London, 2021.

[17] R. Douglas O'Dell, F. W. Brinkley, and D. R. Marr. User's Manual for ONEDANT: A Code Package for One-Dimensional, Diffusion-Accelerated, Neutral-Particle Transport.

[18] T. Downar, Y. Xu, and V. Seker. Theory Manual - PARCS v3.0 U.S. NRC Core Neutronics Simulator.

[19] S. Dürigen. *Neutron Transport in Hexagonal Reactor Cores Modeled by Trigonal-Geometry Diffusion and Simplified P3 Nodal Methods.* Dissertation, Karlsruhe Institute of Technology, Karlsruhe, 2013.

[20] V. Fen, M. Lebedev, V. Sarytchev, and W. Scherer. Modelling of Neutron Absorbers in High Temperature Reactors by Combined Transport-Diffusion Methods, 1992.

[21] C. Fiorina, I. Clifford, M. Aufiero, and K. Mikityuk. GeN-Foam: a novel OpenFOAM® based multi-physics solver for 2D/3D transient analysis of nuclear reactors. *Nuclear Engineering and Design*, 294:24–37, 2015.

[22] C. Fiorina, M. Hursin, and A. Pautz. Extension of the GeN-Foam neutronic solver to SP3 analysis and application to the CROCUS experimental reactor. *Annals of Nuclear Energy*, 101:419–428, 2017.

[23] Y. Fontenla, A. Vidal-Ferràndiz, A. Carreño, D. Ginestar, and G. Verdú. FEMFFUSION and its verification using the C5G7 benchmark. *Annals of Nuclear Energy*, 196:110239, 2024.

[24] S. H. Ghazaie, M. Abbasi, and A. Zolfaghari. The Multi-PN approximation to neutron transport equation. *Progress in Nuclear Energy*, 110:64–74, 2019.

[25] U. Grundmann, Rohde U., Mittag S., and S. Kliem. DYN3D version 3.2 - code for calculation of transients in light water reac-tors (LWR) with hexagonal or quadratic fuel elements - description of models and methods. 2005.

[26] R. Harel, S. Burov, and S. I. Heizler. The Time-Dependent Asymptotic PN Approximation for the Transport Equation. *Nuclear Science and Engineering*, 195(6):578–597, 2021.

[27] R. L. Harrison. Introduction to Monte Carlo Simulation. In *AIP conference proceedings 1204, 17*, 2010.

[28] A. Hébert. A USER GUIDE FOR TRIVAC VERSION4.

[29] A. Hébert. Mixed-dual implementations of the simplified method. *Annals of Nuclear Energy*, 37(4):498–511, 2010.

[30] G. Hu, R. Hu, J. M. Kelly, and J. Ortensi. Multi-Physics Simulations of Heat Pipe Micro Reactor.

[31] D. T. Ingersoll and M. D. Carelli. *Handbook of small modular nuclear reactors*. Woodhead Publishing Series in Energy. Woodhead Publishing, Duxford, United Kingdom and Cambridge, MA, second edition edition, 2021.

[32] W. Kaplan. Advanced Calculus, 4th ed. pages 508–512 1992., 1992.

[33] A. D. Kramer. *Math for electricity and electronics*. Delmar Cengage Learning, Clifton Park, N.Y., 4th ed. edition, 2012.

[34] E. Larsen. A New 2D-Transport, 1D-Diffusion Approximation of the Boltzmann Transport equation.

[35] J. Leppänen, M. Pusa, T. Viitanen, V. Valtavirta, and T. Kaltiaisenaho. The Serpent Monte Carlo code: Status, development and applications in 2013. *Annals of Nuclear Energy*, 82:142–150, 2015.

[36] Levon Ghasabyan. *Use of Serpent Monte-Carlo code for development of 3D full-core models of Gen-IV fast-spectrum reactors and preparation of group constants for transient analyses with TRACE-PARCS coupled system.* Master's thesis, KTH, Stockholm.

[37] E. E. Lewis and W. F. Miller. *Computational methods of neutron transport.* Wiley, New York, 1984.

[38] S. lo Muzio and A. Seubert. Implementation And Validation Of The Steady State SP3 Approximation In The GRS FENNECS Code. In *Proceedings of NENE 2022.* Nuclear Society of Slovenia, 2022.

[39] S. lo Muzio and A. Seubert. Verification of the SP3 Solver in FENNECS with C5G7 Test Cases using HELIOS Cross Sections. *ETSON Conference in Munich*, 2022.

[40] S. lo Muzio and A. Seubert. Validation of the FENNECS SP3 solver with control Rod Insertion Simulations of the ESFR using Serpent cross sections. *Proceedings M&C 2023 - The International Conference on Mathematics and Computational Methods Applied to Nuclear Science and Engineering*, 2023.

[41] S. lo Muzio and A. Seubert. Implementation of the steady state simplified P3 (SP3) transport solver in the finite element neutronic code FENNECS, Part 1: Theory. *Annals of Nuclear Energy*, 200:110303, 2024.

[42] S. lo Muzio and A. Seubert. Implementation of the steady state Simplified P3 (SP3) transport solver in the finite element neutronic code FENNECS, Part 2: Verification. *Annals of Nuclear Energy*, 200:110304, 2024.

[43] S. lo Muzio, A. Seubert, and L. Guo. SIMULATION OF CEFR NEUTRONIC START-UP TESTS WITH FENNECS AND COUPLED PIN-BY-PIN MODEL OF A CEFR SUBASSEMBLY. In *Proceedings of Young Scientist Workshop at Kerntechnik 2022.* 2022.

[44] S. Marguet. *The Physics of Nuclear Reactors.* Springer International Publishing, 2018.

[45] P. C. Matthews. *Vector Calculus.* Springer London, 1998.

[46] Q.-Q. Pan, T.-F. Zhang, X.-J. Liu, H. He, and K. Wang. SP3-coupled global variance reduction method based on RMC code. *Nuclear Science and Techniques*, 32(11), 2021.

[47] Ragab Fayez Moustafa. *Approximation of The Neutron Diffusion Equation on Hexagonal Geometries Using a h-p finite element method*. Dissertation, Universitat Politècnica de València, Valencia, 2016.

[48] A. Rais, D. Siefman, M. Hursin, A. Ward, and A. Pautz, editors. *Neutronics modeling of the CROCUS reactor with SERPENT and PARCS codes*, 2017.

[49] J. B. Reade. *Calculus with complex numbers*. Taylor & Francis, London, 2003.

[50] G. Rimpault, D. Plisson, J. Tommasi, R. Jacqmin, J.-M. Rieunier, D. Verrier, and D. Biron. The ERANOS Code and data system for fast reactor neutronic analyses. In *Proceeding of PHYSOR 2002*, October 2002.

[51] A. Rineiski, C. Meriot, C. Coquelet, J. Krepel, E. Fridman, and K. Mikityuk. Specification of the new core safety measures.

[52] R. Salko, M. Avramova, A. Wysocki, A. Toptan, J. Hu, Porter, N., Blyth, T., C. Dances, A. Gomez, C. Jernigan, J. Kelly, and A. Abarca. CTF Theory Manual.

[53] R. Sanchez. On SP theory. *Annals of Nuclear Energy*, 129:331–349, 2019.

[54] A. Schaffrath, A. Wielenberg, R. Kilger, and A. Seubert. SMRs — overview, international developments, safety features and the GRS simulation chain. *Frontiers in Energy*, 15(4):793–809, 2021.

[55] A. Seubert, J. Bousquet, and R. Henry. RECENT ADVANCES OF THE FENNECS NEUTRONICS CODE FOR SAFETY ASSESSMENT OF (V)SMR, GENERATION IV AND OTHER INNOVATIVE CONCEPTS. In *The International Conference on Mathematics and Computational Methods Applied to Nuclear Science and Engineering*, 2021.

[56] A. Sharma. *Engineering Mathematics, Semester-I, Part-Ii*. Discovery Publishing House Pvt. Limited, 2009.

[57] W. M. Stacey. *Nuclear reactor physics*. WILEY-VCH, Weinheim, 2. ed., completely rev. and enlarged. edition, 2007.

[58] A. Vidal Ferràndiz, A. Carreño, Y. Fontenla, D. Ginestar, and G. Verdú. FEMFFUSION A finite element code to model nuclear reactors: User's Manual, 2023.

[59] A. Vidal-Ferràndiz, A. Carreño, D. Ginestar, C. Demazière, and G. Verdú. A time and frequency domain analysis of the effect of vibrating fuel assemblies on the neutron noise. *Annals of Nuclear Energy*, 137:107076, 2020.

[60] Y. Wang, S. Schunert, and V. Laboure. Rattlesnake Theory Manual.

[61] Y. Wang, S. Schunert, J. Ortensi, V. Laboure, M. DeHart, Z. Prince, F. Kong, J. Harter, P. Balestra, and F. Gleicher. Rattlesnake: A MOOSE-Based Multiphysics Multischeme Radiation Transport Application. *Nuclear Technology*, 207(7):1047–1072, 2021.

[62] C. A. Wemple, H.-N. Gheorghiu, R. Stamm'ler, and E. A. Villarino. Recent Advances in the HELIOS-2 Lattice Physics Code. In *Proceedings of PHYSOR 2008*, 14-19 September 2008.

[63] J. Willert, C. T. Kelley, D. A. Knoll, and H. Park. Hybrid Deterministic/Monte Carlo Neutronics. *SIAM Journal on Scientific Computing*, 35(5):62–83, 2013.

[64] Y. Wu. *Fusion Neutronics*. Springer eBook Collection. Springer, Singapore, 2017.

[65] Y. Wu. *Neutronics of Advanced Nuclear Systems*. Springer eBook Collection. Springer, Singapore, 2019.